

CZECH TECHNICAL UNIVERSITY IN
PRAGUE

Faculty of Nuclear Sciences and Physical
Engineering

Department of Physics



Diploma thesis

**Analysis of D^0 meson production in
Cu+Au collisions in the STAR
experiment**

Miroslav Šaur

Supervisor: Mgr. Pavol Federič Ph.D

Prague, 2017

ČESKÉ VYSOKÉ UČENÍ TECHNICKÉ
V PRAZE

Fakulta Jaderná a Fyzikálně Inženýrská
Katedra Fyziky



Diplomová práce

Analýza produkce mezonu D^0 v Cu+Au
srážkách v experimentu STAR

Miroslav Šaur

Vedoucí práce: Mgr. Pavol Federič, Ph.D.

Praha, 2017



ČESKÉ VYSOKÉ UČENÍ TECHNICKÉ V PRAZE
FAKULTA JADERNÁ A FYZIKÁLNĚ INŽENÝRSKÁ
PRAHA 1 - STARÉ MĚSTO, BŘEHOVÁ 7 - PSČ 115 19



Katedra: fyziky

Akademický rok: 2016/2017

ZADÁNÍ DIPLOMOVÉ PRÁCE

Student: Bc. Miroslav Šaur

Studijní program: Aplikace přírodních věd

Obor: Experimentální jaderná a částicová fyzika

Název práce: Analýza produkce mezonů D0 v Cu+Au srážkách v experimentu STAR
(česky)

Název práce: Analysis of D0 meson production in Cu+Au collisions in the STAR
(anglicky) experiment

Pokyny pro vypracování:

- 1) Kontrola kvality dat z časové projekční komory (TPC) v Cu+Au srážkách z roku 2012 měřených v experimentu STAR.
- 2) Rekonstrukce D0 mezonů v hadronovém rozpadovém kanálu v Cu+Au srážkách v experimentu STAR.
- 3) Určení účinnosti rekonstrukce D0 mezonů.
- 4) Měření invariantního výtěžku a jaderného modifikačního faktoru D0 mezonů.

Doporučená literatura:

- [1] L. Adamczyk et al. (STAR Collaboration), Observation of D0 Meson Nuclear Modifications in Au+Au Collisions at $\sqrt{s_{NN}}=200$ GeV, Phys. Rev. Lett. 113, 142301.
[2] L. Adamczyk et al. (STAR Collaboration), Measurements of D0 and D* production in p+p collisions at $\sqrt{s_{NN}}=200$ GeV, Phys. Rev. D 86, 072013.
[3] K. Yagi et al., Quark-gluon plasma, Cambridge University Press, (2005).


Jméno a pracoviště vedoucího diplomové práce:

Mgr. Pavol Federič, Ph.D., Ústav jaderné fyziky, AV ČR, v. v. i., Řež

Datum zadání diplomové práce: 20.10.2016

Termín odevzdání diplomové práce: 05.05.2017

Doba platnosti zadání je dva roky od data zadání.


vedoucí katedry




děkan

V Praze dne 20.10.2016

Prohlášení:

Prohlašuji, že jsem svou diplomovou práci vypracoval samostatně a použil jsem pouze podklady (literaturu, software, atd.) uvedené v příloženém seznamu.

Nemám závažný důvod proti užití tohoto školního díla ve smyslu 60 Zákona .121/2000 Sb., o právu autorském, o právech souvisejících s právem autorským a o změně některých zákonů (autorský zákon).

V Praze dne 05.05.2017

Title:

Analysis of D^0 meson production in Cu+Au collisions in the STAR experiment

Author: Miroslav Šaur

Specialization: Experimental nuclear and particle physics

Sort of project: Diploma thesis

Supervisor: Mgr. Pavol Federič Ph.D. Nuclear Physics Institute of the Czech Academy of Sciences

Abstract:

Heavy quarks are mainly produced by hard processes during the early stage of heavy-ion collisions and before the formation of the quark-gluon plasma (QGP). As most of the heavy quarks are expected to propagate through the medium during its evolution, they can encode information on different stages of the medium. The D^0 meson is the lightest meson containing a charm quark. Measurement of modifications to D^0 production in heavy-ion collisions relative to a proton-proton collisions can be used to study properties of the nuclear medium. In 2012, the STAR experiment at RHIC recorded Cu+Au collisions at the center-of-mass energy per nucleon pair of $\sqrt{s_{NN}} = 200$ GeV. Measuring D^0 production in asymmetric Cu+Au collisions allows to probe charm quark production in a system with different geometry than the symmetric Au+Au collisions. In this Diploma thesis, the first measurement of the D^0 mesons in Cu+Au collisions is presented. The D^0 mesons are reconstructed via the hadronic decay channel ($D^0 \rightarrow K^- \pi^+$). The invariant yield and the nuclear modification factor of D^0 meson are shown as a function of transverse momentum. These results are then compared with existing results from Au+Au collisions at the same collision energy and corresponding centrality.

Key words: STAR experiment, D^0 meson, nucleus-nucleus collisions, quark-gluon plasma, hard probes.

Název práce:

Analýza produkce mezonu D^0 v Cu+Au srážkách v experimentu STAR

Autor: Miroslav Šaur

Zaměření: Experimentální jaderná a částicová fyzika

Typ práce: Diplomová práce

Supervisor: Mgr. Pavol Federič Ph.D. Ústav Jaderné Fyziky, AV ČR, v. v. i., Řež

Abstrakt:

Těžké kvarky jsou převážně produkovány tvrdými procesy během počátečních fázi srážek těžkých iontu, dříve než dochází k formování kvark-gluonového plazmatu (QGP). U většiny těžkých kvarků se předpokládá jejich průchod médii během evoluce media, tudíž mohou poskytovat informace o mediu. D^0 mezon je nejlehčí mezon obsahující puvabný kvark. Měření modifikace produkce D^0 mezonu ve srážkách těžkých jader vůči proton-protonovým srážkám lze použít ke studiu vlastností jaderného media. V roce 2012 experiment STAR na RHICu zaznamenával srážky Cu+Au s energií na nukleonový pár $\sqrt{s_{NN}} = 200$ GeV. Měření produkce D^0 v asymetrických srážkách Cu+Au umožňuje studium produkce puvabného kvarku v systému s odlišnou geometrií než symetrické srážky Au+Au. Tato Diplomová práce přináší první měření D^0 mezonu ve srážkách Cu+Au. D^0 mezon je rekonstruován v hadronovém rozpadovém kanálu ($D^0 \rightarrow K^-\pi^+$). Invariantní výtěžek a jaderný modifikační faktor D^0 mezonu je zobrazen v závislosti na příčné hybnosti. Výsledky jsou poté porovnány s výsledky z Au+Au srážek při stejné energii srážky a odpovídající centralitě.

Klíčová slova: experiment STAR, D^0 mezon, jádro-jaderné srážky, kvark-gluonové plazma, tvrdé sondy.

Acknowledgement

I would like express my gratitude to my supervisor, Mgr. Pavol Federič Ph.D., for his leading, advices, help and great patience during my work on this Thesis. I would also like to thanks to my colleagues from the Heavy-ion group at the Nuclear Physics Institute of the Czech Academy of Sciences. Namely I would like to thanks to Dr. Jana Bielčíková, the group leader of the Heavy-ion group, for the possibility to be a part of this working group and for the many great advices, to Dr. Filip Křížek, for many helpful comments and willingness to discuss. I also have to mention thanks to my other colleagues from NPI for their help and advices: doc. Dr. Michal Šumbera, Dr. Vít Kučera, Ing. Jan Rusňák and Ing. Miroslav Šimko.

Contents

1	Experimental setup	23
1.1	RHIC	23
1.2	STAR detector	25
1.2.1	Time Projection Chamber	26
1.2.2	Time of Flight detector	28
1.3	Recent and planned runs	29
1.4	Future of the RHIC	30
1.4.1	STAR	30
1.4.2	sPHENIX	33
1.4.3	eRHIC	35
2	Theory overview	37
2.1	Variables used for the description of the heavy-ion collisions .	37
2.1.1	Mandelstam variables	37
2.1.2	Rapidity and pseudorapidity	38
2.1.3	Impact factor and centrality	39
2.1.4	Invariant yield	41
2.1.5	Nuclear modification factor	41
2.1.6	Bjorken x and Feynman x	41
2.2	The Standard model of the particle physics	42
2.3	Strong interaction	43
2.3.1	Asymptotic freedom	44
2.3.2	Color confinement	45
2.4	Hard processes	46
2.4.1	Factorization theorem QCD	47
2.5	Heavy-ion collisions	48
2.5.1	Cu+Au collisions	49
2.6	Quark-gluon plasma	50
2.7	D ⁰ meson	51
3	Overview of experimental results	55
3.1	Results from the STAR experiment	55
3.1.1	p+p results	55

3.1.2	Au+Au results	56
3.2	Results from the PHENIX experiment	59
3.3	Results from the ALICE experiment	60
3.3.1	p+Pb results	60
3.3.2	Pb+Pb results	61
3.4	Results from the CMS experiment	64
4	Analysis of Cu+Au experimental data	69
4.1	Event and track selection	69
4.2	Quality assurance	70
4.3	Identification of pions and kaons	72
4.3.1	PID of K mesons	73
4.3.2	PID of π mesons	74
4.4	Methods of background reconstruction	76
4.4.1	Like-sign method	77
4.4.2	Mixed-event method	77
4.4.3	Rotated momentum method	78
4.5	Raw D^0 yield	78
5	Detector Efficiencies	83
5.1	TOF efficiency	83
5.2	Tracking efficiency	84
5.3	Total reconstruction efficiency of the D^0 meson	86
6	Systematics uncertainties	93
6.1	Double counting	96
7	Results and discussion	99

List of Figures

1	History of the Universe	20
1.1	Layout of RHIC	24
1.2	RHIC summary of energies, species and luminosity.	24
1.3	STAR detector	26
1.4	Time Projection Chamber	27
1.5	MWPC pad	27
1.6	Barrel Time of Flight detector	28
1.7	Ratio of multiplicity for Ru and Zr	31
1.8	Initial magnetic field for Ru+Ru and Zr+Zr collisions.	31
1.9	STAR 2020+ plan	33
1.10	The layout of the eRHIC collider	35
2.1	Schematic view of a collision of two particles.	38
2.2	Centrality distribution	40
2.3	Definition of participants and spectators	40
2.4	Standard model	43
2.5	Interaction between gluons	44
2.6	Measurements of coupling constant α_s	45
2.7	String breaking mechanism.	46
2.8	Hard scattering sub-processes in QCD	48
2.9	Timeline of a heavy-ion collisions with creation of QGP.	49
2.10	Cu+Au collision	50
2.11	Phase diagram of matter	51
2.12	D^0 two main decay channels	52
3.1	D^0 raw signals from p+p at $\sqrt{s} = 200 \text{ GeV}$	56
3.2	Cross section of $c\bar{c}$	57
3.3	Production cross-section of $c\bar{c}$ in p+p collisions from Run12	57
3.4	Differential invariant yield of D^0 at Au+Au collision,	58
3.5	R_{AA} of D^0 from Au+Au collisions	59
3.6	R_{AA} of D^0 from Au+Au collisions with data from HFT	60
3.7	Measurement of R_{AA} of J/ψ at Cu+Au by PHENIX.	61
3.8	Raw invariant mass of D^0 , D^{*+} from p+Pb collisions	62

3.9	R_{pA} for D^0 , D^+ and D^{*+} from p+Pb collisions	62
3.10	R_{AA} for D mesons and for J/ψ from Pb+Pb collisions	63
3.11	R_{AA} of prompt D^0 , D^+ , and D^{*+} mesons for the 0-10 % and 30-50 %	65
3.12	R_{AA} of prompt D^0 , D^+ , D^{*+} mesons and light mesons for the 0-10 % and 30-50 %	66
3.13	D^0 R_{AA} from CMS	67
4.1	Distribution of Vz_{TPC}	71
4.2	Distribution of DCA	71
4.3	Reference multiplicity	72
4.4	TOF multiplicity as function of reference multiplicity	73
4.5	Particle identification via TOF	74
4.6	PID of kaons via TOF before cuts	75
4.7	PID of kaons via TPC	75
4.8	The p_T distribution of pions	76
4.9	PID of π meson via TOF	76
4.10	Raw Yield of D^0 meson - Mixed-event method	79
4.11	Raw Yield of D^0 meson - LS method	80
4.12	Raw Yield of D^0 meson - ROT method	81
4.13	Invariant mass distribution of $K\pi$ pairs in the p_T bin $0.8 <$ $p_T < 2.0$ GeV/ c^2	82
5.1	Measured raw p_T distribution of charged pions in the TPC	84
5.2	Measured raw p_T distribution of charged pions in the TOF	85
5.3	Measured raw p_T distribution of charged kaons in the TPC	86
5.4	Measured raw p_T distribution of charged kaons in the TOF	87
5.5	TOF efficiency for kaons	87
5.6	TOF efficiency of pions	88
5.7	TPC tracking efficiency for K^+	88
5.8	TPC tracking efficiency for K^-	89
5.9	TPC tracking efficiency for π^+	89
5.10	TPC tracking efficiency for π^-	90
5.11	The total reconstruction efficiency of D^0 meson	91
6.1	Raw yield of D^0 meson, $0.8 < p_T < 2.0$ GeV/ c with condition FitPoints ≥ 25	94
6.2	Raw yield of D^0 meson, $0.8 < p_T < 2.0$ GeV/ c for DCA = 1 cm	95
6.3	Raw yield of D^0 meson, $0.8 < p_T < 2.0$ GeV/ c for DCA = 3 cm	96
6.4	Double counting of D^0 in Au+Au collisions	97
7.1	Nuclear modification factor for the D^0 meson	100

List of Tables

1.1	Overview of Run 15	29
1.2	Overview of Run 16	29
1.3	Overview of Run 17	30
1.4	Overview of Run-18	30
4.1	Centrality classes division	72
4.2	Overview of D^0 meson raw yield by various method	78
5.1	Parameters of the embedding process.	85
6.1	Systematic uncertainties	97

Introduction

Birth of the modern nuclear and particle physics can be traced to the Joseph John Thompson, who in the 1897 discovered electron during his studies of cathode discharge. From J. J. Thompson originated the "pudding" model of the atom, where electrons are point-like objects with negative charge in the positively charged volume of the atom. Next great breakthrough was experiment of Ernest Rutherford who discovered positively charged nucleus of atom. This experiment consisted of irradiating of the gold foil by the α -particles. In the next few following years the neutrons, positrons, neutrinos and many subatomic particles were discovered.

With the still increasing numbers of sub-atomic particles the question about what is the fundamental building block of the nature arise again. By studying of Deep inelastic scattering in the late 1960's it was found, that protons have an internal structure - *partons*. In 1962 Gell-Mann [1] and Zweig [2], completely independently, comes with quark model. Subsequently partons were identified as quarks. Quark model was later developed into the theory of the strong interaction - the quantum chromodynamics.

Strong interaction have two distinct features: confinement and asymptotic freedom. The strong interaction, in basic approximation, behaves as an inverse function of the distance between quarks. For small distances between quarks the strong interaction is almost negligible, but with increasing distance the intensity of the strong interaction increase. This behavior is known as an asymptotic freedom and it implies the nonexistence of free quarks - the confinement.

Collins and Perry in 1975 comes with prediction of superdense matter consists of quarks than of hadrons [3]. In the case of specific conditions, quarks are not longer confined within matter and becomes a free particles. This requires extreme densities of matter which can be found, for example, in neutron stars, black holes and early after the Big bang [3]. Matter formed from the free quarks and gluons is called quark-gluon plasma and is believed, that the Universe was in the state of quark-gluon plasma a few microsecond after the Big bang. This is illustrated in Fig. 1.

One of the main part of contemporary high-energy physics are ultra-relativistic heavy-ion collisions, in which hadronic matter is under extreme conditions and quark-gluon plasma is created. This phase of matter can

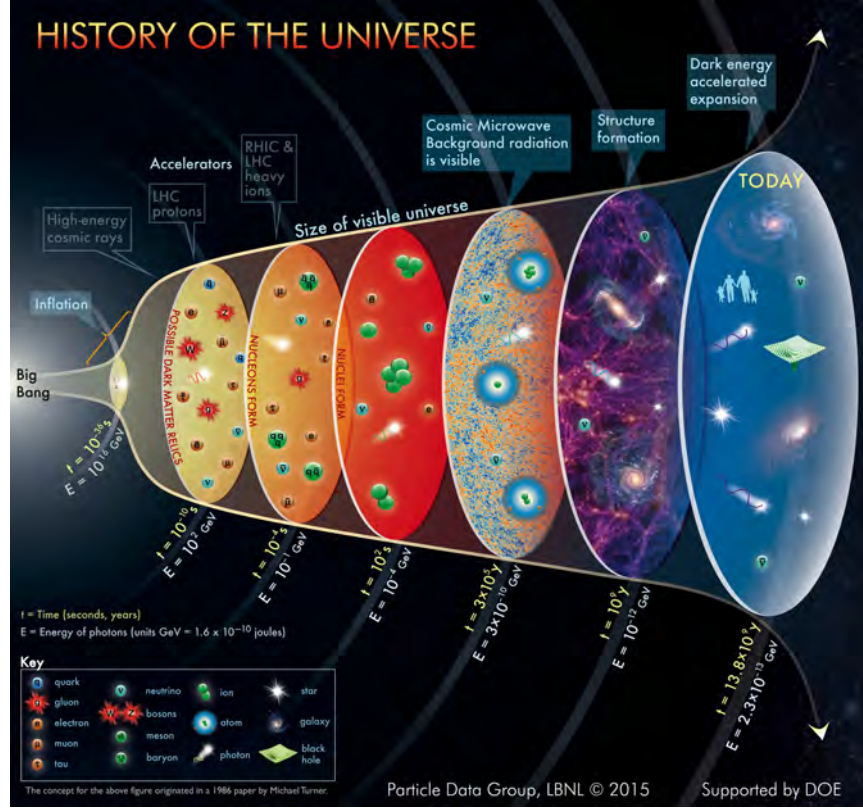


Fig. 1: History of the Universe with highlighted distinctive phases. In the time $t \sim \mu\text{s}$ the Universe is believed to be in the state of quark-gluon plasma. Distinctive eras of the Universe are shown. Taken from Ref. [4].

be studied by various method. One of method is to measure production of different types of particles in heavy-ion collisions and compare results with data from proton-proton collisions. Obtained difference tell us, how much quark-gluon plasma modified production of particles and how particles propagates through quark-gluon plasma.

Theme of this Thesis is analysis of the D^0 in Cu+Au collisions at $\sqrt{s_{NN}} = 200$ GeV. Main goals are quality check of Cu+Au data, D^0 reconstruction in hadronic decay channel $D^0 \rightarrow K^- \pi^+$ (and charge conjugates), calculating reconstruction efficiency, invariant yield and nuclear modification factor. Measuring D^0 production in asymmetric Cu+Au collisions allows to probe charm quark production in a system with different geometry than the symmetric Au+Au collisions.

This diploma thesis is divided at two main parts. First part consist of three chapters and is mainly mentioned as introduction part. This part discuss experimental setup, overview of theory and experimental results about D^0 from STAR, ALICE, CMS experiments.

Second part, which started with Chapter 4, describes analysis of D^0 in Cu+Au collisions. Chapter 4 shows required cuts, methods of particle and background identification, and raw yield of D^0 meson. Chapter 5 describes how detector efficiencies were obtained and final reconstruction efficiency of D^0 meson. In the Chapter 6 systematic uncertainties are shown with description of their origin and how significant they are. Last chapter, Chapter 7, is dedicated to overview and discussion of this thesis final results, the invariant yield and nuclear modification factor of D^0 meson in Cu+Au collisions. These results are compared to the results from Au+Au collisions.

Results of this Diploma thesis were approved by the STAR collaboration and presented as the poster at the XXVI international conference on ultrarelativistic heavy-ion collisions: Quark Matter 2017.

Chapter 1

Experimental setup

In this chapter the experimental setup will be described. At first will be described Relativistic Heavy Ion Collider (RHIC), than the Solenoidal Tracker at RHIC (STAR) detector and sub-detectors of the STAR. After that description, current and planned physical runs of RHIC are mentioned. End of the chapter is dedicated to brief overview of the RHIC future: new experiment sPHENIX and possible upgrade to an Electron-Ion Collider (EIC).

1.1 RHIC

RHIC is located at Brookhaven National Laboratory (BNL) on Long Island, New York state, USA. RHIC is a synchrotron (storage ring) based accelerator, scheme of the RHIC complex is shown in Fig. 1.1. One of the main goal of RHIC is to study the quark-gluon plasma. The formal RHIC proposal was issued in August 1984, actual construction began at 1991. The construction of RHIC was completed in 1999 and the first physics run took place in June 12, 2000. Two Au beams were collided with center-of-mass energy per nucleon $\sqrt{s_{NN}} = 28$ GeV [5]. RHIC itself consists of two independent rings - called "Yellow" and "Blue" - where in the Blue ring the beam orbits in the clock-wise direction and in the Yellow ring beam orbits in the counter clock-wise direction. The maximal energies of collisions at the RHIC are $\sqrt{s_{NN}} = 200$ GeV for ions and $\sqrt{s} = 510$ GeV for protons [7].

To accomplish its goals, RHIC is capable of colliding several different systems such as polarized protons, deuterons and isotopes of ${}^4_2\text{He}$, ${}^{27}_{13}\text{Al}$, ${}^{63}_{29}\text{Cu}$, ${}^{197}_{79}\text{Au}$, ${}^{238}_{92}\text{U}$. There were symmetrical collisions p+p (and polarized p+p), Cu+Cu, Au+Au, U+U. Besides symmetrical system, RHIC is able to collide also several non-symmetrical geometries: p+Au, p+Al, d+Au, He+Au, Cu+Au [7]. RHIC is the only spin-polarized collider in the world. Even some fixed target experiments takes place at RHIC [8]. Cu+Au collisions will be more described in the Chapter 2, which is dedicated to the theory overview. Summary of collisions energies, species combinations and

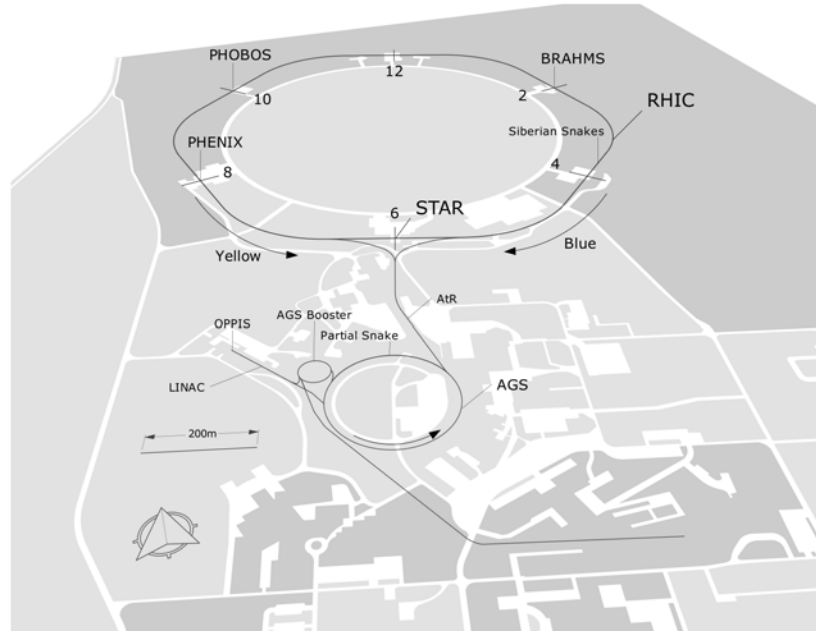


Fig. 1.1: Layout of Relativistic Heavy Ion Collider and it's pre-accelerators. Taken from Ref. [6].

luminosities is show in Fig. 1.2.

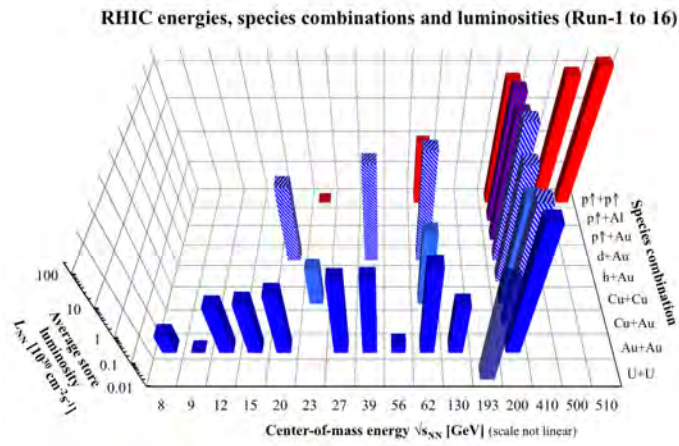


Fig. 1.2: Summary of collisions energy, species combinations and average store luminosity from Run 1 (2001) to Run 16 (2016) at RHIC. Taken from Ref. [7]

RHIC originally hosted 4 large experiments:

- Solenoidal Tracker at RHIC
- Pioneering High Energy Nuclear Interaction eXperiment (PHENIX)
- PHOBOS
- BRAHMS

Nowadays only one of the original four detectors at RHIC are still active: STAR. Detectors PHOBOS, BRAHMS and PHENIX is already finished their physical program and are no longer active.

1.2 STAR detector

The STAR detector main purpose is to study hot and dense nuclear matter in heavy-ion collisions via detecting, tracking and identifying charged particles in mid-rapidity. STAR detector consist of a room-temperature solenoid magnet with full field strength $B = 0.5$ T which surrounds most of the detector sub-systems. Magnetic field is parallel to the beam-pipe axis. The STAR detector¹ is a combination of 13 sub-detectors, where 6 sub-detectors are azimuthally symmetrical (from inner to outer):

- Heavy flavor tracker (HFT)², which consist of:
 - PiXeL detector (PXL)
 - Intermediate Silicon Tracker (IST)
 - Silicon Strip Tracker (SST)
- Time of Flight (TOF)
- Time Projection Chamber (TPC)
- Barrel ElectroMagnetic Calorimeter (BEMC)
- Muon Telescope Detector (MTD)

STAR has also following forward detectors (forward rapidity region $1.086 < \eta < 2$):

- Endcap Electromagnetic Calorimeter (EEMC)
- Forward GEM Tracker (FGT)

The last three detectors provide fast trigger:

¹As in 2016.

²Installed from Run 14 to Run 16.

- Vertex Position Detector (VPD)
- Beam-beam counter (BBC)
- Zero degree Calorimeter (ZDC)

Schematic view of the STAR detector is show in Fig. 1.3.

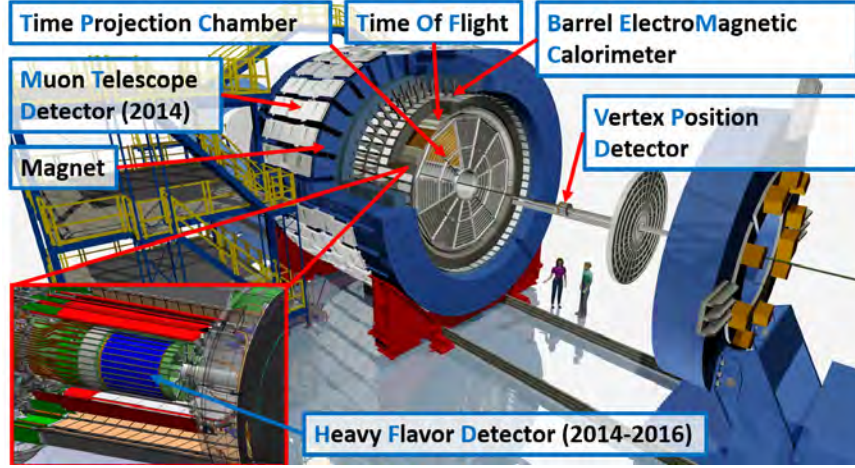


Fig. 1.3: Schematic view of the STAR detector at RHIC. Courtesy of Alexander Schmah and Jakub Kvapil from the STAR Collaboration

For purpose of this work only the following sub-detectors will be described in more detail : TPC, TOF, and VPD as they are crucial for this thesis data analysis.

1.2.1 Time Projection Chamber

Time Projection Chamber (TPC) is primary tracking sub-detector of charged particles . In addition, TPC provides particle identification via their specific ionization energy loss.

The TPC is cylindrical tracking detector with outer diameter $r_{\text{out}} = 4$ m and inner $r_{\text{in}} = 1$ m , with length 4.2 m (Fig. 1.4) and full azimuthal angle ($0 < \phi < 2\pi$) coverage. Pseudorapidity coverage is ± 1.0 units [9].

Internally TPC is divided into two halves (at $z = 0$) along the beam pipe by the Central Membrane. Voltage of membrane is -28 kV. The membrane serves as a TPC cathode. Internally TPC is further divided by a equipotential rings which forms the field cage. Multi-wire proportional chambers (MWPC) serve as an anode, and with the membrane and the field cage creating together an uniform electric field of $E \sim 135$ V/cm. Cylinder volume of the TPC is filled with P10 gas (10% of methane and 90% of argon) with pressure 200 Pa above the atmospheric pressure.

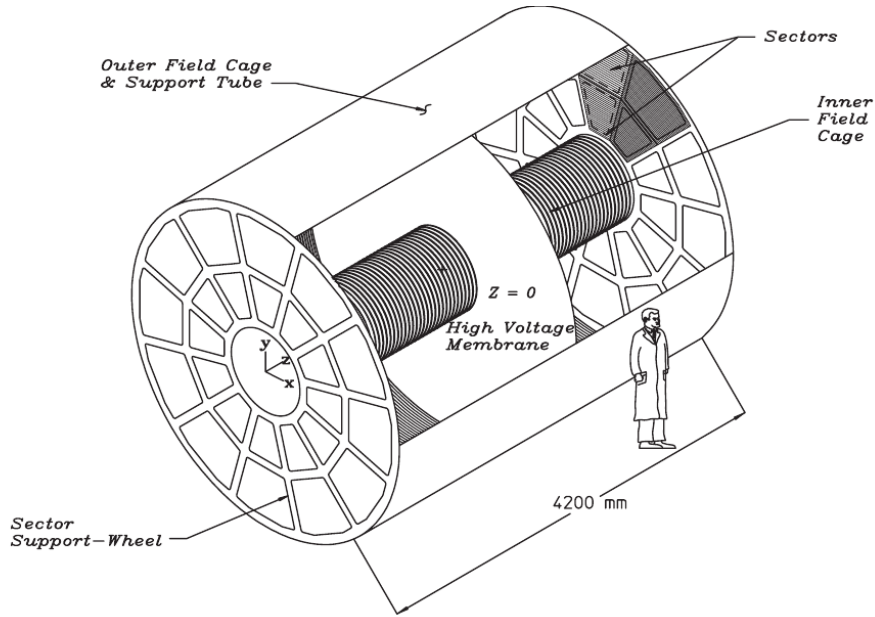


Fig. 1.4: Schematic view of Time Projection Chamber sub-detector of the STAR. Taken from Ref. [9].

The MWPC are divided into 12 sectors. In each sector there are 13 inner and 32 outer pad rows. In total MWPC consist of 136 560 read-outs pads. Fig 1.5 shows geometry of one section of MWPC.

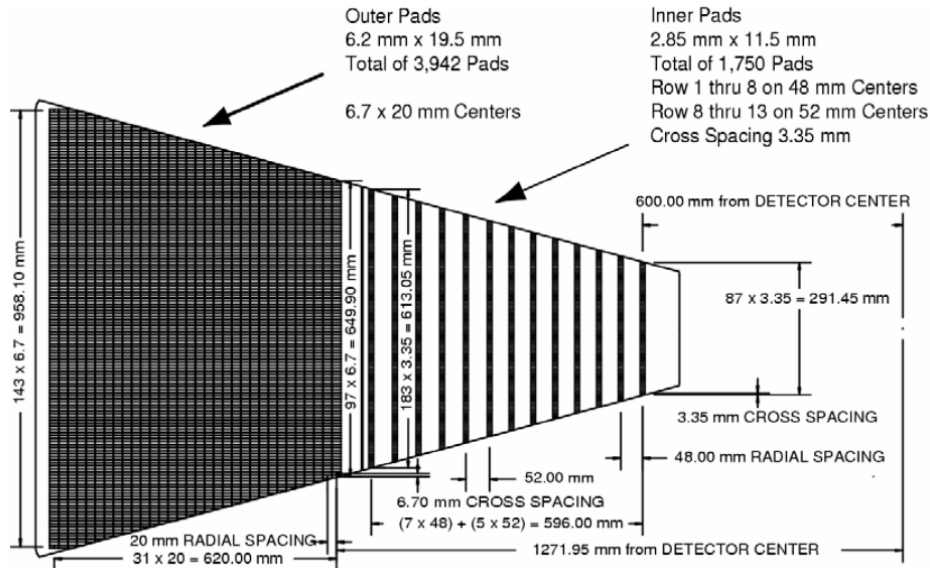


Fig. 1.5: Schematic view of the anode pad plane. Taken from Ref. [9].

Charged particle traversing the volume of TPC ionizing P10 gas. Electrons then drift towards anode at an average velocity $v_{e,\text{drift}} = 5.45 \text{ cm}/\mu\text{s}$, resulting in maximum drift time in the TPC $t_{\text{max,drift}} = 40 \mu\text{s}$. Drift velocity depends on temperature and pressure inside TPC.

1.2.2 Time of Flight detector

Time-of-Flight detector (TOF) is designed for the measurement time of flight of particle and together with TPC to obtain information about masses and velocity of particles passing through TPC and TOF. TOF consist of Barrel TOF (BTOF) and the Vertex position Detector (VPD).

BTOF consist of 120 trays that cover full azimuthal angle and pseudo-rapidity at ± 1.0 units. Sub-detector itself is based on Multi-gap Resistive Plate Chamber (MRPC) technology, which using collection of currents induced by alternation of electric field that is caused by electron avalanches created in detector gas. Each tray of BTOF has 32 MRPC modules, each module containing 6 pads. Geometry of BTOF is shown at Fig. 1.6.

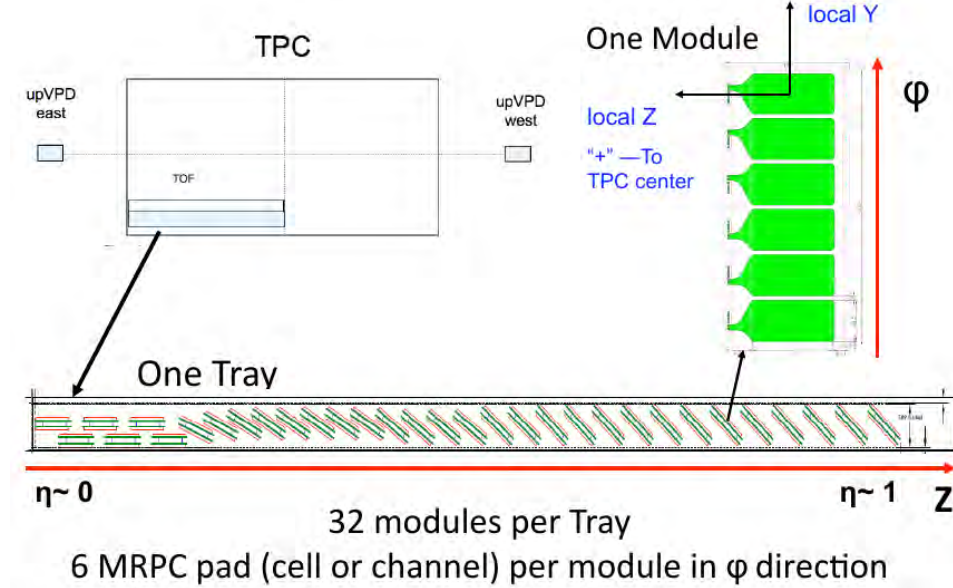


Fig. 1.6: Geometry of Barrel Time of Flight detector. Taken from Ref. [10]

The VPD is a coincidental detector and consist of two identical parts on the west and east side of the beam pipe, 5.7 m from centre of STAR detector. Each part consist of 19 cylindrically shaped channels of lead layers, scintillator and a photo-multiplier tube. The VPD measures the start time and BTOF measure stop time. Then can be obtained equation

$$\text{stop time} - \text{start time} \equiv \tau,$$

where τ is particle time of flight.

1.3 Recent and planned runs

Run 15 consisted of 22.4 cryo-weeks and takes place from 24.01.2015 to 28.07.2015. During Run-15 3 types of collisions takes place: p+p, p+ $^{197}_{79}\text{Au}$ and p+ $^{27}_{13}\text{Al}$. Collision system are listed in Tab. 1.1.

System	$\sqrt{s_{\text{NN}}}$ [GeV/nucleon-nucleon]	T	L [pb $^{-1}$]
Polarized p+p	200	10.9 weeks	382
Polarized p + $^{197}_{79}\text{Au}$	200	5.1 weeks	1270
polarized p + $^{27}_{13}\text{Al}$	200	1.9 weeks	3.97

Tab. 1.1: Overview of Run 15. The $\sqrt{s_{\text{NN}}}$ is a total energy per nucleon-nucleon pair, T is duration of each type of collisions, L is a total delivered luminosity. Taken from Ref. [7].

For the year 2016 there were 20 cryo-weeks. Run 16 started at 25.01.2016 and ended at 29.07.2016. Specific informations about Run 16 are in Tab. 1.2.

System	$\sqrt{s_{\text{NN}}}$ [GeV/nucleon-nucleon]	T	L [nb $^{-1}$]
$^{197}_{79}\text{Au} + ^{197}_{79}\text{Au}$	200	14.4 weeks	52.2
d + $^{197}_{79}\text{Au}$	200	8 days	289
d + $^{197}_{79}\text{Au}$	62	6 days	44
d + $^{197}_{79}\text{Au}$	20	11 days	7.20
d + $^{197}_{79}\text{Au}$	40	7 days	19.5

Tab. 1.2: Overview of Run 16. The $\sqrt{s_{\text{NN}}}$ is a total energy per nucleon-nucleon pair, T is duration of each type of collisions, L is a total delivered luminosity. Taken from Ref. [7].

Run 17 started at 21.02.2017 and should end in July 2017. Specific informations about Run 17 are in Tab. 1.3.

For the Run 18 main goal is to take data about isobaric collisions Ru+Ru and Zr+Zr [11]. Collisions of isobaric nuclei $^{96}_{44}\text{Ru}$ and $^{96}_{40}\text{Zr}$ provides an opportunity to study chiral magnetic and chiral vortical effects. Nuclei will collide at $\sqrt{s_{\text{NN}}} = 200$ GeV and is planned to collect $1.2 \cdot 10^9$ events. Chiral effects are long discussed and experimental results so far support chiral magnetic effects, chiral magnetic wave and chiral vortical effects. Ratio of charged particle multiplicity created in Ru+Ru and Zr+Zr collisions is almost identical (excluding 0-5% most central collisions) but they had different

System	$\sqrt{s_{NN}}$ [GeV/nucleon-nucleon]	Duration [week]
Polarized p+p	500	13
p+p	500	1
CeC	-	2
Au+Au	62.4	4

Tab. 1.3: Overview of Run 17. The $\sqrt{s_{NN}}$ is a total energy per nucleon-nucleon pair, CeC is a Coherent electron Cooling. Taken from Ref. [11]

nucleus deformity β_2 . For Ru $\beta_2 = 0.158$, for Zr $\beta_2 = 0.08$ - these are results from e-A scattering³. Overview of Run 18 is show in Tab. 1.4.

System	$\sqrt{s_{NN}}$ [GeV/nucleon-nucleon]	Duration [week]
Ru+Ru	200	3.5
Zr+Zr	200	3.5
Au+Au	27	2

Tab. 1.4: Overview of Run-18. The $\sqrt{s_{NN}}$ is a total energy per nucleon-nucleon pair. Taken from Ref. [11]

Due to different deformation of nucleus and number of protons, the initial magnetic field would be different for Ru+Ru and Zr+Zr collisions. Theoretical calculations for initial distribution of magnetic field are shown in Fig. 1.8. If there really are chiral magnetic and chiral vortical effects, then those effects should be functions of $(\frac{eB}{m_\pi})^2 \cos[2(\psi_B - \psi_{RP})]$, where e is elementary charge, B is magnetic field, m_π is mass of pion, ψ_B is a angle of the magnetic field and ψ_{RP} is a angle of the reaction plane of a given event [11].

1.4 Future of the RHIC

1.4.1 STAR

The STAR collaboration has many experimental plans beyond 2020, which are supported by the Nuclear Science Advisory Committee (NSAC) 2015 Long Range plan. This document emphasize importance of the RHIC and STAR in the research that studies properties of QGP and the spin structure of the proton [12]. Summary of proposed plans and upgrades can be seen in Fig. 1.9.

³According different sources - comprehensive model deductions - deformity parameter is $\beta_2 = 0.053$ for Ru and $\beta_2 = 0.217$ for Zr, which is the quite opposite to results from e-A scattering [11].

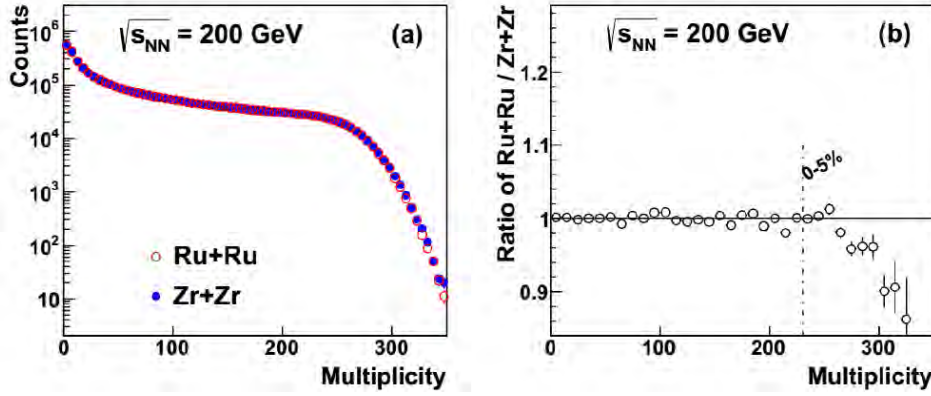


Fig. 1.7: Panel (a): The Glauber model multiplicity simulation for Ru and Zr. Panel (b): Ratio of the Glauber model multiplicity. The solid lines represents calculations with Glauber model, dashed lines represent calculation with comprehensive model deductions. Taken from Ref. [11].

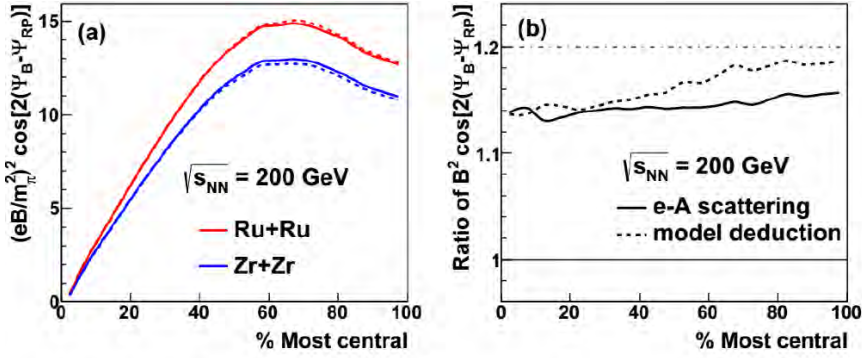


Fig. 1.8: Panel (a): Initial magnetic field for Ru+Ru and Zr+Zr collisions. Panel (b): Ratio of distribution versus centrality. The solid lines represents calculations with Glauber model, dashed lines represent calculation with comprehensive model deductions. Taken from Ref. [11].

Proposed items of the physics program envisioned by the STAR Collaboration are [13]:

- Studies of the nuclear parton distribution and fragmentation functions.
- Understanding of the nature of the pomeron and potentially discovering the odderon.
- Extension of gluon polarization results down to low- x .
- Constraints on the transport coefficients \hat{e} and \hat{q} near the critical temperature T_c .

- Constraints on the 3+1D hydrodynamics and temperature dependence of relevant QGP properties.

To achieve these goals several hardware upgrades are required, namely [13]:

- inner TPC (iTPC): improving tracking and mid-rapidity resolution,
- Event Plane Detector (EPD): improvement of event plane resolution,
- Forward Electromagnetic and Hadronic Calorimeters (fCal): extending forward calorimetry capabilities,¹
- HFT+: Replacing PXL layer with next generation Monolithic Active Pixel Sensor (MAPS) technology and new electronics,
- Streaming: Implementing new read-out electronics on most detectors,
- Replacing the BSMD readout.

Physics Goal	Measurements	Requirements							
			Base	fCal	fTS	RP	HFT+	BSMD	Streaming
Nuclear PDFs	DV, Direct photons +J/Psi R_{pA}	★ ■	✓	✓	Enh				
Nuclear FF	Hadron + Jet	★ ■	✓						Enh
Polarized Nuclear FF	Hadron + Jet	★	✓						
Odderon & Polarized Diffraction	A_{UT} of pion + forward proton	★		✓		✓			
Low-x ΔG	Di-jets	★	Enh	✓	✓				
High-x Transversity	Hadron+jet	★ ■		✓	✓				
Mapping the Initial State in 3-D: QGP Transport Properties	R. Plane Rapidity de-correlations	★	Needs iTPC						
	Ridge $ \Delta\eta < 3$	★	Needs iTPC						
	Ridge $ \Delta\eta < 6$	★	Needs iTPC		✓				
	Forward Energy Flow	★	Needs iTPC	✓					
Effects of Chiral Symmetry at $\mu_B=0$	Di-lepton spectra at $\mu_B=0$	★ ■	Needs iTPC				HFT out		Enh
	Extended LPV observables	★ ■	Needs iTPC						Enh
Internal Structure of the QGP and Color Response	$Y(1S, 2S, 3S)$	○	✓						
	B R_{AA}	★ ■	✓				✓		
	B v_2	★ ■	✓				✓	✓	✓
	B-tagged Jets	○	✓				✓		
	Jets	○	✓						Enh
	γ -jets	○	✓					✓	
Phase Diagram and Freeze-out	BES-II Observables at $\mu_B=0$	★	Needs iTPC						
	C6/C2, C4/C2	★	Needs iTPC						
The Strong Force	Exotics and Bound States (di-Baryons)	★	Needs iTPC						✓
Estimated Cost M\$				2.0	4.0	0.6	5.0	1.0	4.5

✓ Measurement needs upgrade

Enh : Enhances measurement, but is not required

★ Unique to STAR

○ Complementary to sPHENIX

■ Complemented by LHC and/or JLab

Fig. 1.9: Summary of the STAR 2020+ plan and the required upgrades to perform these measurements. Taken from Ref. [13].

1.4.2 sPHENIX

One of the major upgrades of RHIC experiments since its operational start is project sPHENIX. PHENIX collaboration proposed at 2012 a major upgrade of the PHENIX detector which should open new possibilities for studying of QGP, but technically the sPHENIX is completely new detector. This upgrade was approved in 2015.

sPHENIX collaboration proposed mainly the following measurements [14]:

- jets,
- b-tagged jets,
- photons,

- charge hadrons and their correlations,
- measurement of Υ particles family.

The sPHENIX detector should consist of (from inner to outer layer)⁴ [15]:

- MAPS detector
- Inner Tracker (INTT)
- Time Projection Chamber (TPC)
- Electromagnetic calorimeter (EMCal)
- Inner hadronic calorimeter (IHCAL)
- Solenoid magnet
- Outer hadronic calorimeter (Outer HCal)

The MAPS detector, the inner-most tracking detector, is based on technology used for the ALICE Inner Tracking System upgrade design. Resolution of the decay vertex should be $DCA_{xy} < 70 \mu\text{m}$ [15].

INTT detector should provide continuity in tracking between MAPS and TPC, DCA determination and pile-up rejection. It consists of 4 layers of Si strips.

The TPC, the outer-most tracking detector, is located between 20 and 78 cm in radius, expected effective hit resolution is $250 \mu\text{m}$. The main goal of the TPC is to provide momentum resolution for particles between 0.2 and 40 GeV/ c in p_T . A continuous read-out of the TPC is planned.

The electromagnetic calorimeter is a tungsten-scintillating fibre sampling calorimeter with silicon photo-multipliers read-out system.

The hadronic calorimeter is a sampling calorimeter. It is divided into two pieces - outer (HCal) and inner (IHCAL) hadronic calorimeter. IHCAL consist of non-magnetic metal and scintillator located inside the bore of solenoid magnet. Outer HCal is outside of the cryostat.

Magnet of sPHENIX is taken from the BaBar experiment. It is a solenoid magnet with operating current $I_{op} = 4596 \text{ A}$ and maximal intensity of magnetic field $B = 1.5 \text{ T}$. The solenoid magnet is already transfered to the BNL.

The sPHENIX collaboration expects that the sPHENIX detector should be fully operational at the RHIC run 2021 and take first date in 2022. More about sPHENIX can be found at the Proposal of sPHENIX [14] and [15].

⁴In the most recent variant from the November 2016

1.4.3 eRHIC

Proposed *Electron Ion Collider* (EIC) is a great step at experimental possibilities in high energy physics. Proposed idea of colliding electrons with heavy ions opens many new areas of research which are not possible reached with current experimental technologies. For a few lets name a gluon saturation, test of QCD at small scales of the x^5 , precise measurements of spin distribution inside a proton, etc. Realization of EIC at RHIC should bear name eRHIC. More about eRHIC can be found at [16]. The proposed layout of the eRHIC is shown in Fig. 1.10.

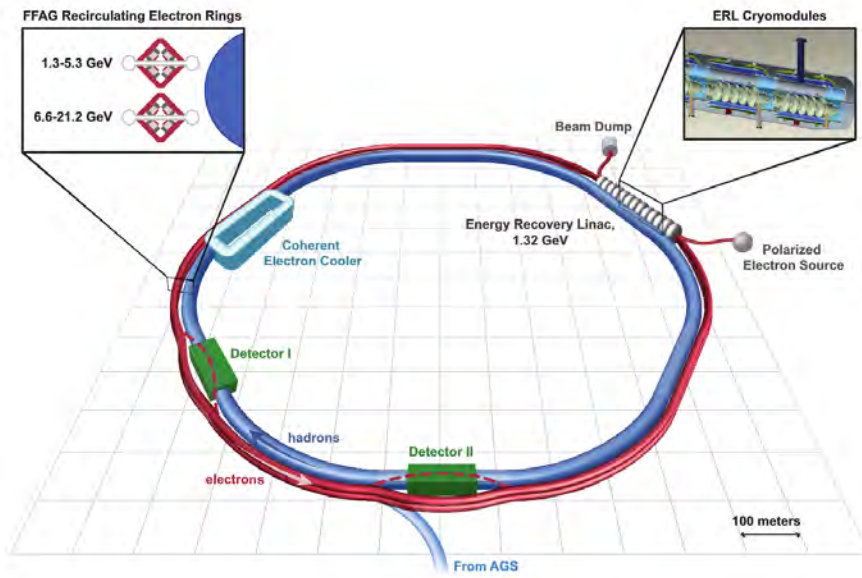


Fig. 1.10: The layout of eRHIC collider. Taken from Ref. [16].

⁵Defined by the Eq. 2.12.

Chapter 2

Theory overview

Experiments at the RHIC discovered a new phase of matter called the *quark-gluon plasma* (QGP) in Au+Au collisions at $\sqrt{s_{NN}} = 200$ GeV in 2004 [17]. The QGP is produced in heavy-ion collisions with high energy densities, where temperature of system cross the critical temperature $T_c = 170$ MeV [18]. One possible way to study QGP is by looking at modification of various particle production in heavy-ion collisions (where is QGP created) compared to a binary collision scaled spectra from proton-proton collisions. In order to have better understanding of hard process in QGP in this chapter we review hard processes, heavy-ion collisions, quark-gluon plasma, D^0 meson will be discussed.

2.1 Variables used for the description of the heavy-ion collisions

In this section, a few basic variables commonly used in high energy and heavy-ion physics will be presented. Such a variables are: Mandelstam variables, rapidity and pseudorapidity, impact parameter, centrality, invariant yield and the nuclear modification factor.

2.1.1 Mandelstam variables

For a basic binary collision, as shown in Fig. 2.1, the Mandelstam variables can be defined as:

$$s = (p_1 + p_2)^2 = (p_3 + p_4)^2 \quad (2.1)$$

$$t = (p_1 - p_3)^2 = (p_2 - p_4)^2 \quad (2.2)$$

$$u = (p_1 - p_4)^2 = (p_2 - p_3)^2 \quad (2.3)$$

where p_1, p_2, p_3 and p_4 are four-momentum defined according to Fig. 2.1. They are Lorentz invariant. The Mandelstam variables fulfill:

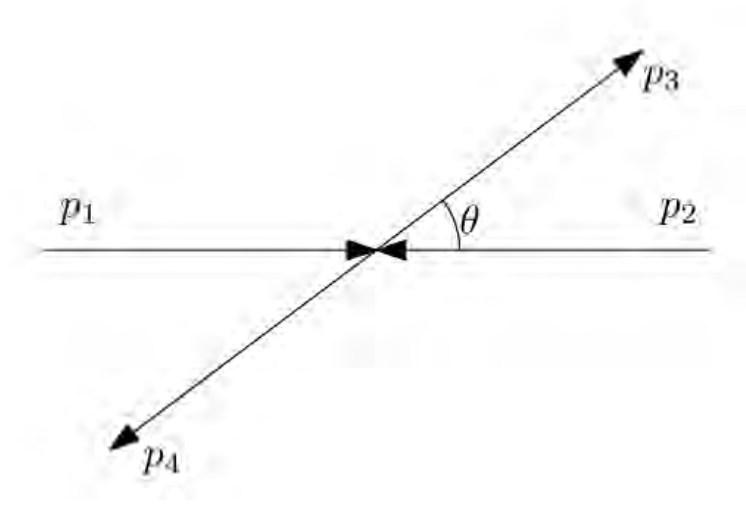


Fig. 2.1: Schematic view of a collision of two particles. Four-momenta of the particles are labeled as p_1, p_2, p_3, p_4 .

$$s + t + u = \sum_{i=1} m_i^2, \quad (2.4)$$

where m_i is the mass of the i -th particle in the collisions. The index i goes from 1 to the number of involved particles.

Total energy of one ion in the heavy-ion collision can be expressed as $N_{\text{pair}}/2 \cdot \sqrt{s_{\text{NN}}}$, where N_{pair} is the number of nucleon-nucleon pairs and $\sqrt{s_{\text{NN}}}$ is the energy of the nucleon-nucleon pair at the centre-of-mass system.

2.1.2 Rapidity and pseudorapidity

The rapidity variable y is defined as:

$$y = \frac{1}{2} \ln \left(\frac{E + p_z}{E - p_z} \right), \quad (2.5)$$

where E is total energy of the particle, p_z is longitudinal momentum of the particle in the direction of the axis z . Variable defined according to the Eq. 2.5 is Lorentz additive along the z -axis.

Total energy E and longitudinal momentum p_z can be extracted from known rapidity via following equations:

$$E = m_T \cosh y \quad (2.6)$$

$$p_z = m_T \sinh y \quad (2.7)$$

Where m_t is transverse mass of the particle, defined as:

$$m_T = \sqrt{m^2 + p_T^2} \quad (2.8)$$

The pseudorapidity η can be seen as an alternative to the rapidity y . It is defined by the following equation:

$$\eta = -\ln\left(\tan\frac{\theta}{2}\right), \quad (2.9)$$

where angle θ is the angle of the deviation of the particle from the beam axis. Pseudorapidity is equal to rapidity only for the massless particles. Experimentally is much easier to measured the pseudorapidity than the rapidity.

2.1.3 Impact factor and centrality

The centrality of the heavy-ion collision is defined via the impact factor b . Let R_1 and R_2 be the radius of the first nucleus or the second two colliding nuclei, respectively. Then the parameter b belongs to the interval $(0, R_1 + R_2)$. Impact parameter gives the distance between the center of gravity of each nucleus at the moment of the collision. For the $b \sim 0$ collisions are referred as a *head-on* or most central collisions, collisions with the $b \sim R_1 + R_2$ are the peripheral collisions, for the $b = R_1 + R_2$ the collisions are *ultra-peripheral*, in this case there is no physical contact between nucleus but still there is a electromagnetic interactions between them. According the value of the parameter b the *centrality* of the collisions can be defined or more precisely division of all collisions into the *centrality classes*. Impact parameter b cannot be measured directly but have to be measured indirectly, mainly via the *multiplicity* variable. Multiplicity is a number of the produced charged particles per collision where higher multiplicity corresponds to lower values of the impact parameter. Exact division into centrality classes can vary from various experimental and theoretical collaborations, an example of one such division is show in Fig. 2.2. For calculating the centrality the *Glauber model* [20] is used.

Protons and neutrons which took place in collisions are called *participants*, proton and neutrons which not took place in collisions are called *spectators*. Fig. 2.3 shows example of one collision with highlighted participants and spectators.

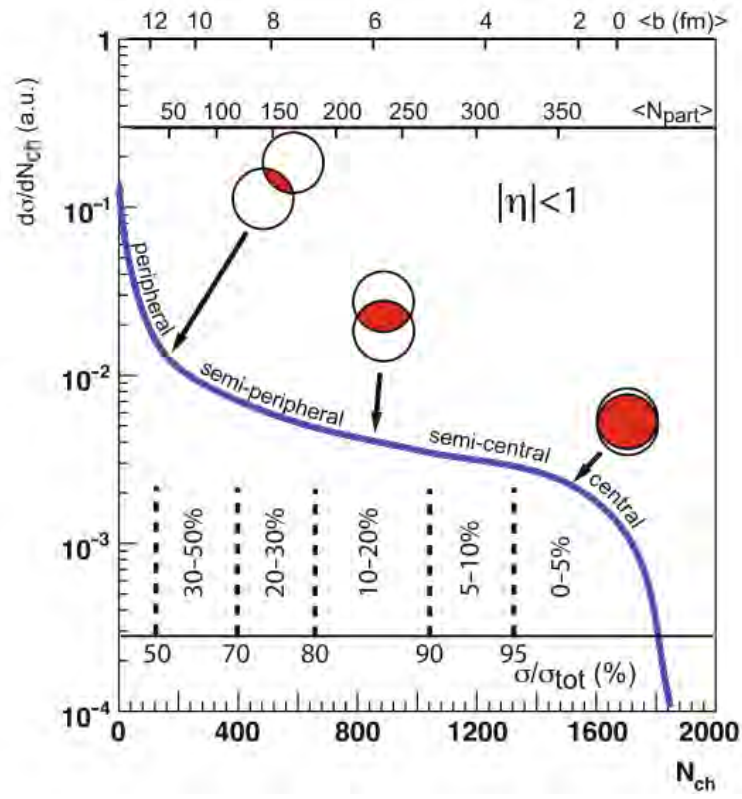


Fig. 2.2: Centrality distribution as a function of charged particles multiplicity N_{ch} . N_{part} represents the number of participants in the collision. Taken from Ref. [19].

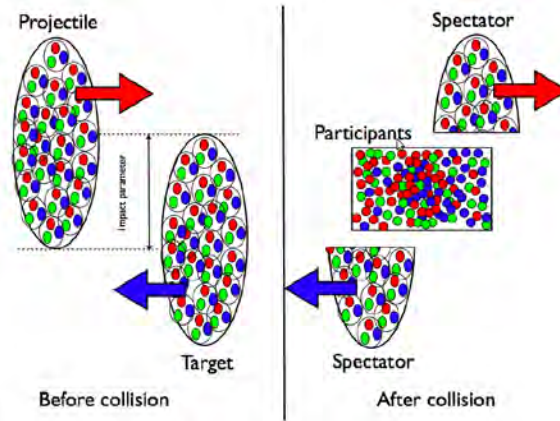


Fig. 2.3: Definition of participants and spectators in heavy-ion collisions. Taken from Ref. [21].

2.1.4 Invariant yield

Invariant yield for any particle X can be defined as:

$$B \frac{d^2 N}{d\phi p_T dp_T dy} = \frac{1}{2\pi p_T \Delta p_T \Delta y} \frac{N_X}{\epsilon_{\text{total}}} \frac{1}{N_{\text{ev}}}, \quad (2.10)$$

where B is the branching ratio of particular decay channel, p_T is the mean transverse momentum in the bin of width Δp_T and Δy is the rapidity interval. The N_X is the X raw yield in a given p_T and Δy interval, ϵ_{total} is a total reconstruction efficiency of X and N_{ev} is the number of analyzed events.

2.1.5 Nuclear modification factor

Because the QGP created in heavy-ion collision exists just for a very short time (typically $\tau \sim 10$ fm/ c), only indirect methods of measurement are possible. One option is to compare particle spectra from the system where QGP is created, heavy-ion collisions, with the system without QGP, the proton-proton collisions. In the case of the heavy-ion collisions there will be difference, in the comparison to the proton-proton collisions, in the final particle spectra due to interaction of quarks and gluons with the strongly interacting medium.

One possible variable for the study of QGP is the nuclear modification factor, R_{AA} , which is defined as:

$$R_{AA} = \frac{1}{\langle N_{\text{bin}} \rangle} \frac{d^2 N / dy dp_T^{AA}}{d^2 N / dy dp_T^{pp}}, \quad (2.11)$$

where $\langle N_{\text{bin}} \rangle$ is the average number of the binary (nucleon-nucleon) collision in one heavy-ion collisions for given centrality class of heavy-ion collisions, $d^2 N / dy dp_T^{AA}$ represents a yield from the nucleon-nucleon collisions, $d^2 N / dy dp_T^{pp}$ represents a corresponding particle yield from the proton-proton collisions. Three cases for values of R_{AA} can be distinguished. The $R_{AA} > 1$ represents the situation when particles production is enhanced against p+p collisions. For $R_{AA} = 1$ particles production behave the same as in binary scaled pp. Finally, $R_{AA} < 1$ represents the situation when particles production in heavy-ion collisions is suppressed with respect to scaled p+p collisions.

2.1.6 Bjorken x and Feynman x

Hard-scattering processes (including heavy flavor production) are described by means of *Bjorken* x , x_{Bj} , and *Feynman* x , x_F . Both variables are Lorentz invariant, and if some process can be described by x_{Bj} then it can be described by the x_F as well. The x_{Bj} is defined by Eq. 2.12 [22]:

$$x_{Bj} = \frac{Q^2}{2m_p\nu}, \quad (2.12)$$

where Q^2 is a squared transferred momentum, m_p is a mass of the parton, ν is a transferred energy. The x_{Bj} belongs to the interval (0, 1). This variable was originally defined in deeply inelastic scattering (DIS) as a relativistically-invariant variable describing the final state of the electron in high-energy e+p scattering. In the DIS the x_{Bj} represents momentum fraction of a proton which is carried by the parton.

The x_F is defined by Eq. 2.13 [22]:

$$x_F = \frac{p_Z^A}{p_{Z(max)}^A} = \frac{2p_Z^X}{\sqrt{s}}, \quad (2.13)$$

where p_Z^A is the longitudinal momentum of particle X in the p+p CM frame and p_{ZMax}^X is the maximum momentum that particle X can have in this frame depending on the energy of the collision and the masses of the particles. The x_F can reach values from -1 to 1. Positive values of the x_F mean that the particle is moving in the direction of the beam, particle with negative values of the x_F is moving in the opposite direction. High absolute values of the x_F correspond to high energies and high rapidity in the Laboratory system.

2.2 The Standard model of the particle physics

The Standard model of the particle physics (SM) is a theory describing 3 of the 4 known fundamental interactions (strong, weak, electromagnetic, gravitational) [23]. Particles included in the SM are: 6 gauge bosons *gluon*, $W^{+/-}$, Z^0 , γ , (spin = \hbar) and H^0 (spin = 0) which intermediate fundamental interactions and 12 elementary fermions (spin = $\hbar/2$). Fermions are further divided to 6 leptons: *electron* (e), *muon* (μ), *tau* (τ), *electron neutrino* (ν_e), *muon neutrino* (ν_μ), *tau neutrino* (ν_τ), and 6 quarks: *up* (u), *down* (d), *charm* (c), *strange* (s), *top* (t), *bottom* (b). Each fermion has also its own antiparticle. Table of SM particles is shown in Fig. 2.4. Mathematically the Standard model is a non-abelian gauge theory with the symmetry group $SU(3)_c \times SU(2)_L \times U(1)_Y$.

The fundamental interactions included at the SM are:

- Strong interaction - described by quantum chromodynamics (QCD)
- Weak interaction - described by electro-weak theory (EWT)
- Electromagnetic interaction - described by quantum electrodynamics (QED)

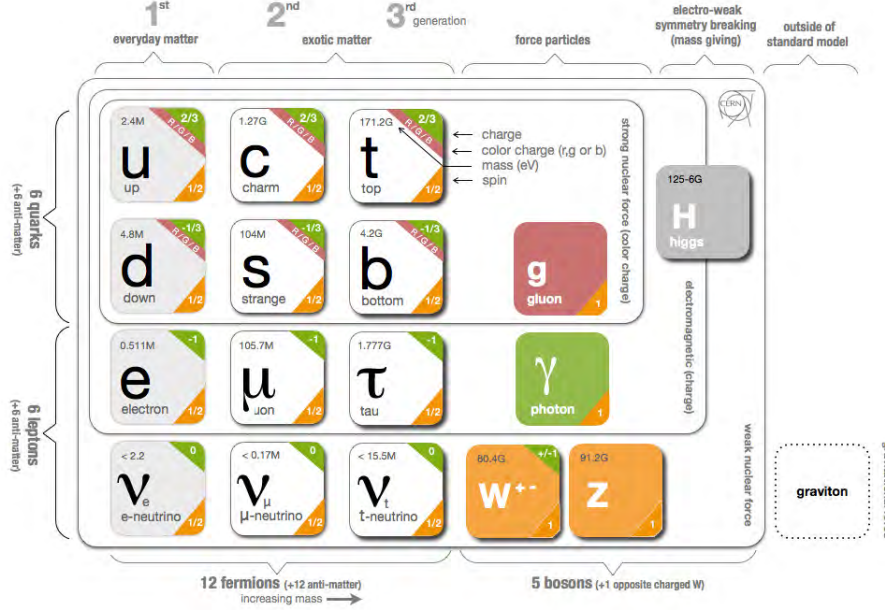


Fig. 2.4: Particles of the Standard model and their interactions. Taken from Ref. [24].

Weak interaction and electromagnetic interaction are united in the electroweak interaction.

According the Standard model, quarks form the *mesons* - a bounded state of a quark and an anti-quark, and *baryons* - a bounded state of three quarks. Mesons and baryons are collectively called as a *hadrons*. In the past few years there are reported observations of *tetraquark* [25]- a bounded state of four quarks, and *pentaquark* - a bounded state of five quarks [26].

2.3 Strong interaction

The strong interaction is described by quantum chromodynamics. It is a non-abelian field theory with $SU(3)_c$ group of symmetry. QCD defines a new quantum number - *color charge* or *color*. There are 3 basic colors: *red* (r), *green* (g), *blue* (b). To any of these colors an anti-color exist. Gluons carry combination of color and anti-color charge. Totally, 8 combinations intermediate strong interaction (white or colorless combination of gluon is non-physical):

$$r\bar{g}, r\bar{b}, b\bar{g}, g\bar{r}, g\bar{b}, b\bar{b}, \frac{1}{\sqrt{2}}(r\bar{r} - g\bar{g}), \frac{1}{\sqrt{6}}(r\bar{r} + g\bar{g} - 2b\bar{b})$$

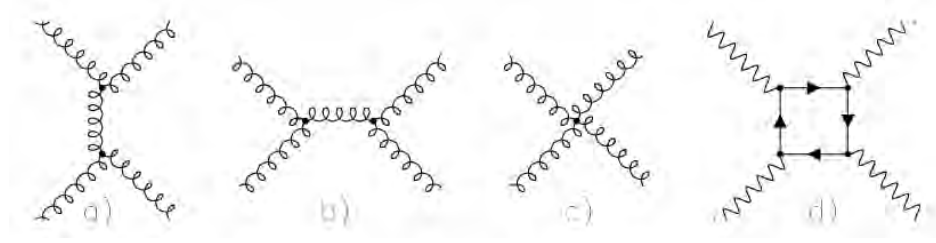


Fig. 2.5: Schematic view of gluons interactions in Feynman diagrams. Taken from Ref. [27]

All observed hadrons are colorless. Two main distinct features of strong interactions are *asymptotic freedom* and *confinement* (more about this features below). In the QCD the gluons can interact between themselves as shown in Fig. 2.5.

The Lagrangian of QCD is given by [23]

$$\mathcal{L}_{\text{QCD}} = \sum_q \bar{\psi}_{q,a} (i\gamma^\mu \partial_\mu \delta_{ab} - g_s \gamma^\mu t_{ab}^C \mathcal{A}_\mu^C - m_q \delta_{ab}) \psi_{q,b} - \frac{1}{4} F_{\mu\nu}^A F^{\mu\nu A}, \quad (2.14)$$

where over repeated indexes is summed. The $\psi_{q,a}$ are quark-field spinors of quark q with mass m_q and color charge a that goes from 1 to 3 (one index for one color charge). The γ^μ are Dirac gamma-matrices. The \mathcal{A}_μ^C are gluon fields, where C goes from 1 to 8, as there are 8 types of gluons. The t_{ab}^C are 3×3 matrices representing generators of the $SU(3)_c$ symmetry group. The $F_{\mu\nu}^A$ is field-strength tensor which describes interactions between gluons and which is defined as [23]:

$$F_{\mu\nu}^A = \partial_\mu \mathcal{A}_\nu^A - \partial_\nu \mathcal{A}_\mu^A - g_s f_{ABC} \mathcal{A}_\mu^B \mathcal{A}_\nu^C, \quad (2.15)$$

where

$$[t^A, t^B] = i f_{ABC} t^C,$$

where f_{ABC} are structure constants of the $SU(3)_c$ group.

The fundamental parameters of QCD are the coupling constant of the Strong interaction g_s (coupling constant can be equally written as: $\alpha_s = \frac{g_s^2}{4\pi}$) and masses of each quark m_{q_i} .

2.3.1 Asymptotic freedom

Asymptotic freedom can be explained via the so-called Cornell potential¹ [22]. The Cornell potential describes interaction between two quarks at

¹This potential is used as general QCD potential, but was primarily derived for quarkonia (*quarkonium* - a bounded state of heavy quark and its own anti-quark. *Charmonium* - $c\bar{c}$, *bottomium* - $b\bar{b}$)

$T = 0$ [22]:

$$V(r) = -\frac{4}{3} \frac{\alpha_s}{r} + \sigma r, \quad (2.16)$$

where α_s is a alternative expression for the coupling constant of strong interaction, r is a distance, σ is a *string tension constant* which represents tension of color field between valence quarks in meson in string model. As can be seen from 2.16 for small distances, Coulomb term $\frac{\alpha_s}{r}$ dominates and potential is repulsive for quark-antiquark pair. However, for large distances linear part of potential, σr linearly rises and is responsible for color confinement.

The effective QCD coupling constant α_s in the terms of renormalization theory can be expressed as [27]

$$\alpha_s \approx \frac{4\pi}{\beta_0 \ln(\mu^2/\Lambda_{QCD}^2)} \approx \frac{12\pi}{25 \ln(Q^2/\Lambda^2)}, \quad (2.17)$$

where β_0 is a beta function, μ^2 is a renormalization scale, Λ_{QCD}^2 is the scale of QCD. In second expression Λ^2 is cutoff parameter unique for each value of Q^2 . As can be seen from 2.17 for fixed $\beta_0 > 0$, the α_s have only μ^2 functional dependence, so with increasing μ^2 effective constant α_s decreases. This implies that for short distances or for high transferred momentum coupling constant goes to 0 and quarks and gluons behaves as free particles.

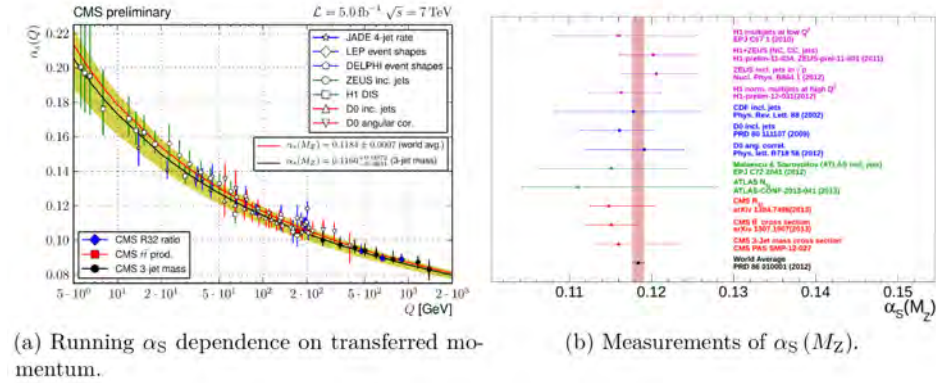


Fig. 2.6: Measurements of the strong coupling constant α_s . [28]

2.3.2 Color confinement

As had been already mentioned above, all observed hadrons are without color charge, or can be said with *white* color charge. From behavior of the Cornell potential 2.16 at larger distances coupling between quark and anti-quark gets stronger to the point when enough energy is stored in color field

and new pair of quark and anti-quark is created. Color field is often depicted as string, schematics of this process is shown in Fig. 2.7.

This model can explain why any particle with bare color charge have not been observed, but this model does not have an analytical proof within QCD.

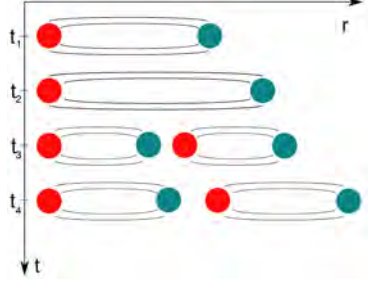


Fig. 2.7: Schema of a string breaking mechanism and creation of a quark-antiquark pair. [28]

2.4 Hard processes

Generally all interaction in particle or heavy-ion collisions can be divided into two main groups:

- Hard processes
- Soft processes

There is no clearly defined and generally acknowledged separation between those two groups, but the hard processes can be defined as processes with transferred four-momentum squared Q^2 greater than hundreds of GeV/c , and/or processes that can be described by the *perturbative QCD* (pQCD) [19] [22].

Hard probes can be defined as objects created by the hard processes, and can be listed as:

- Hard jets and partons with high p_T
- Heavy quarks and hadrons with open flavor
- Heavy quarkonia (J/ψ , Υ) and their excited states
- Direct photons
- Production of $W^{+/-}$ and Z^0 bosons

Creation time of all hard probes is smaller than the creation time of the QGP, thus creating of the hard probes is not influenced by the QGP. Subsequently probes propagates through the QGP and interacting with the medium hence they may serve as a probes of QGP.

2.4.1 Factorization theorem QCD

The main idea of the factorization theorem is to divided the formulas to part which can be described (and enumerated) by non-pertubative QCD a to part which need to be computed via pertubative QCD. This idea come from assumption, that any parton-parton interaction occurs much quicker than any long-distance interactions (but still within QCD space-time scale) that happens before or after the collision itself. If this assumption is true, than nucleus can be treated as system of free partons.

One of the main goals of QCD is computation of cross section of high p_T partons collision. For high energy partons collision the production of new parton with high momentum can be computed by *QCD factorization theorem*. [19]:

$$d\sigma_{AB \rightarrow h}^{hard} = f_{a/A}(x_1, Q^2) \otimes f_{b/B}(x_2, Q^2) \otimes d\sigma_{ab \rightarrow c}^{hard}(x_1, x_2, Q^2) \otimes D_{c \rightarrow h}(z, Q^2), \quad (2.18)$$

where:

•

$$d\sigma_{ab \rightarrow c}^{hard}(x_1, x_2, Q^2),$$

is the perturbative cross-section enumerated to the order of renormalization constant α_s

•

$$f_{a/A}(x_1, Q^2),$$

is a parton distribution function (PDF) - a probability of finding quark a with momentum fraction $x = \frac{p_{parton}}{p_{nucleus}}$ in nucleon A . Non-perturbative term of the factorization theorem.

•

$$D_{c \rightarrow h}(z, Q^2),$$

is a fragmentation function (FF) describing the probability of fragmentation of the outgoing parton c into the observed hadron h with momentum $z = \frac{p_{hadron}}{p_{nucleus}}$. Non-perturbative term of the factorization theorem.

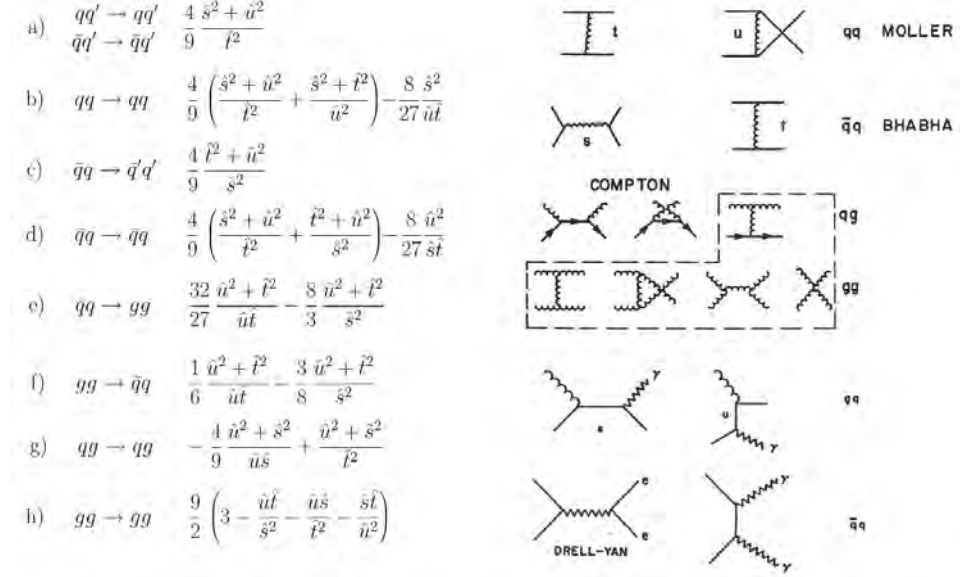


Fig. 2.8: Hard scattering sub-processes in QCD. On the left side: (a)-(h) show different sub-processes for quarks q , antiquarks \bar{q} and gluons g . On the right side: figures of the lowest order diagrams involving initial state q and g scattering. Equations represents cross-section of the particular interaction. Taken from Ref. [22]

In the case of nucleus-nucleus collision, 2.18 implies, that total hard inclusive cross section scale as

$$d\sigma_{AB}^{hard} = A \cdot B \cdot d\sigma_{pp}^{hard}, \quad (2.19)$$

where A and B is number of nucleons in each of colliding ions. $d\sigma_{pp}^{hard}$ is total hard inclusive cross for $p + p$ collision.

In Fig. 2.8 can be seen numerous sub-processes of QCD. First three sub-processes are analogues of processes from QED, respectively Moller, Bhabha and Compton scattering. Test of validity of these processes in QCD was one of the first proofs of validity of QCD [22].

2.5 Heavy-ion collisions

The goal of heavy-ion collisions is to produce and study the QCD matter under high temperatures and pressure, e.g. the QGP.

Time evolution of a heavy-ion collisions can be divided into 7 phases² - 1 pre-collision phase and 6 phases that follow after collision:

²This division depends on author, in all of this work division according the [19] is used.

1. Incoming hadrons - described by saturation models and by *color glass condensate* approach.
2. Hard scattering - described by pQCD. Highest energy density, creation of heavy quarks and hard probes. Time of the hard scattering is $\tau_{HS} \sim 0.1 \text{ fm}$
3. Glasma/strong fields - described by classical field theory.
4. Gluons and quarks out of equilibrium - described by kinetic theory.
5. Gluons and quarks at equilibrium - described by hydrodynamics.
6. Freeze out. The numbers and types of hadrons does not change any more.

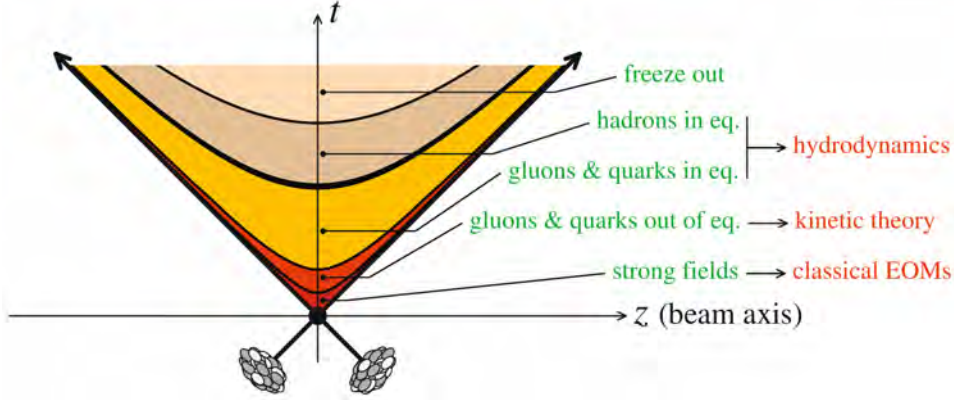


Fig. 2.9: Timeline of heavy-ion collision with highlighted phases of collisions. Taken from Ref. [19]

Today, primarily two isotopes of heavy-ion are collided: $^{197}_{79}\text{Au}$ at RHIC in the range $\sqrt{s_{NN}} = 7.8\text{--}200 \text{ GeV}$ and $^{208}_{82}\text{Pb}$ at LHC with $\sqrt{s_{NN}} = 2.76\text{--}5.02 \text{ TeV}$.

2.5.1 Cu+Au collisions

In 2012 for 5.5 weeks, Cu+Au collisions took place at RHIC. Isotopes $^{63}_{29}\text{Cu}$ and $^{197}_{79}\text{Au}$ were collided with energy $\sqrt{s_{NN}} = 200 \text{ GeV}$. Primary motivation of Cu+Au collisions was a measurement of this system as a control geometry for Au+Au collisions, because according the Glauber model, the number of participants in Cu+Au central collisions should agree with semi-central Au+Au collisions. Cu+Au system is asymmetrical both in longitudinal and transverse direction. Sketch of this system is show in Fig. 2.10

Another study possibilities at Cu+Au collisions are studies of flow effect created by initial asymmetric density profile which leads to asymmetric

pressure gradient and chiral effects due to sizable initial electric field, which pointing from Au to Cu. This may lead to a charge dependence of the directed flow.

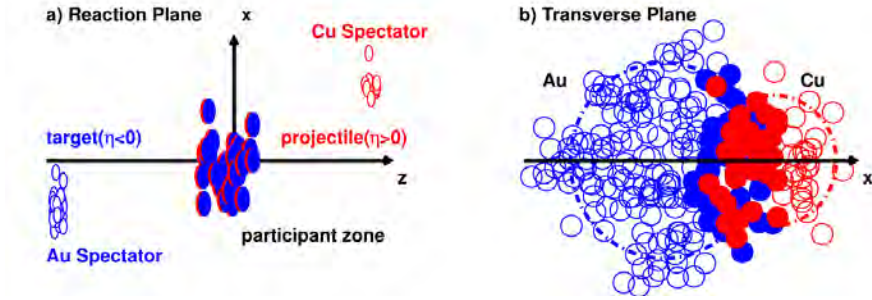


Fig. 2.10: Schematic imagination of a Cu+Au collision. a: View from a reaction plane. b: View from transverse plane. Taken from Ref. [29].

2.6 Quark-gluon plasma

As already has been said above, RHIC published compelling evidence about existence of a new hot and dense state of matter called quark-gluon plasma in 2004. Two main characteristics of QGP is *deconfinement* and restoration of *chiral symmetry*.

Quarks and gluons cannot be observed as free particles in normal conditions. But in the case of high temperatures or high densities the hadronic matter goes through the phase transition and quarks and gluons becomes free particles. This phenomena is called as the *deconfinement*, which is in accordance with QCD [3]. For high temperatures Cornell potential 2.16 has to be rewritten as [22]:

$$V(r) = -\frac{4}{3} \frac{\alpha_s}{r} \exp^{-\mu_d r} + \sigma \frac{1 - \exp^{-\mu_d r}}{\mu_d}, \quad (2.20)$$

where $\mu_d = \mu_d(T) = \frac{1}{r_D}$ is Debye screening mass. For $r \ll \frac{1}{\mu_d}$ matter is in normal conditions and quarks and gluons are confined in the hadronic matter. But for $r \gg \frac{1}{\mu_d}$ deconfinement occurs, quarks and gluons are free.

Critical temperature is about $T_c = 170$ MeV. One of the main goals of current heavy-ion physics is to find exact critical temperature T_c , position of the critical point in the phase diagram of the hadronic matter and nature of the phase transition. In the case of LHC energies the matter goes through the cross-over.

Partons with high momentum are predominately created via the hard-scattering in the early stage of a collision before formation of the QGP.

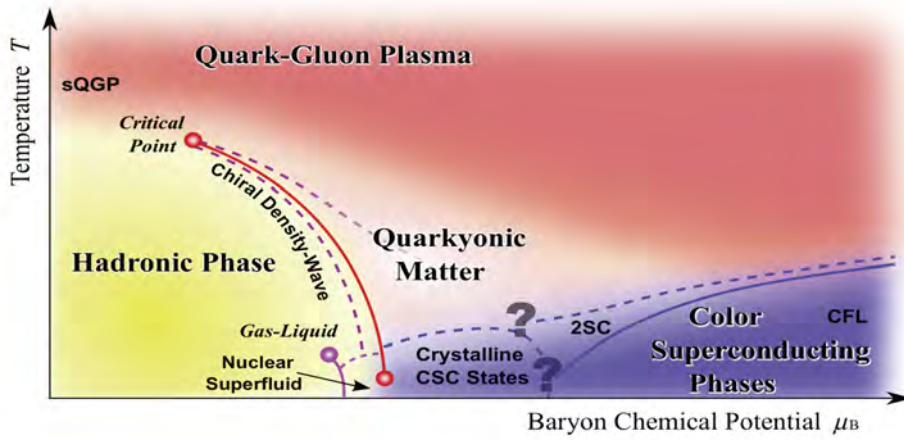


Fig. 2.11: Phase diagram of matter with dependence of Temperature T on Baryon Chemical Potential μ_B . Taken from Ref. [30].

As they subsequently propagate through the QGP, they interact with this medium and are losing energy via inelastic processes (for example radiative energy loss and emission of soft gluons) and via elastic processes (collisional energy loss). For all quarks and gluons the hierarchy of radiative energy loss in the medium is presumed as [22]:

$$\Delta E(g)_{rad} > \Delta E(q)_{rad} > \Delta E(c)_{rad} > \Delta E(b)_{rad}, \quad (2.21)$$

where ΔE_{rad} is radiative energy loss in the medium for gluons g , light quarks q (u, d, s), charm quark c and bottom quark b . The top quark is not mentioned because its decay long before ($\tau_{t,decay} \sim 0.1 \text{ fm}/c^2$ [23]) the formation of the QGP. But recent experimental results from the STAR, ALICE and the CMS collaborations indicate³, that the charm quarks have a similar magnitude of the energy losses as the light quarks.

2.7 D^0 meson

D^0 meson is a bounded state of u and \bar{c} quark (for \bar{D}^0 quark composition is $c\bar{u}$), with invariant mass $m_{D^0} = (1864.84 \pm 0.007) \text{ GeV}/c^2$ [23]. First discovered at SLAC in 1976, D^0 is the lightest meson containing *charm* quark. For this feature, D^0 is often used as one of the first probes of the medium.

Charm quarks are mainly created at initial hard scattering with the minimum value of $Q^2 = 2m_{charm}c^2$, with the corresponding space-time scale $\tau_c \sim 0.1 \text{ fm}$. Production of D^0 in heavy-ion collisions can be studied via

³This results are described in the Chapter 3.

semi-leptonic decay or by hadronic decay. Study of D^0 meson production via semi-leptonic decay is only indirect since this channel cannot give access to parent hadron kinematics and is more influenced by decay of hadrons with bottom quark. But the semi-leptonic channel is easily triggered and have higher branching ration. Hadronic decay gives the complete access to parent hadron kinematics, but they have smaller branching ratio and larger combinatorial background. Schematic view of both decay channels is shown in Fig. 2.12.

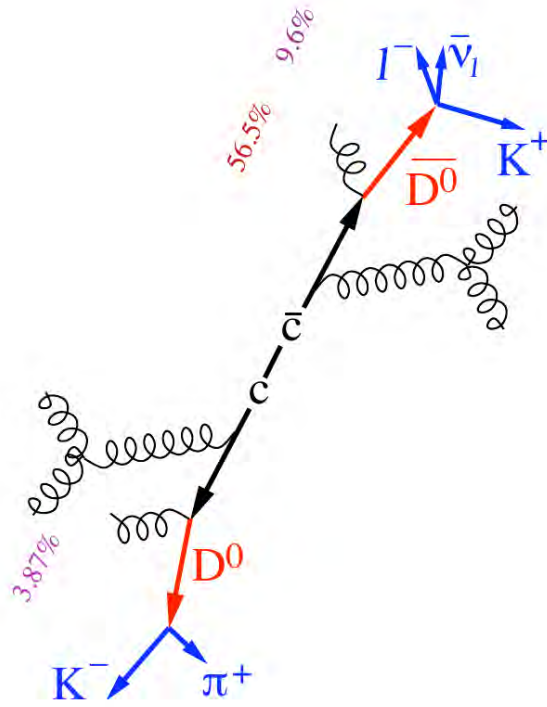


Fig. 2.12: Fragmentation of a c quark to D^0 meson and two main D^0 meson decay channels. [10]

In this analysis the D^0 mesons are reconstructed via the hadronic decay channel $D^0 \rightarrow K^- \pi^+$. The branching ratios are shown in Fig. 2.12. The π mesons are the lightest mesons with the rest mass $m_{\pi^0} = 134.9766 \pm 0.0006$ MeV/ c^2 and $m_{\pi^\pm} = 139.57018 \pm 0.00035$ MeV/ c^2 . Quark composition of π^+ / π^- is $u\bar{d} / \bar{u}d$ respectively. The K mesons are the mesons with the rest mass $m_{K^0} = 493.677 \pm 0.013$ MeV/ c^2 and $m_{K^\pm} = 497.614 \pm 0.024$ MeV/ c^2 . Quark composition of K^+ / K^- is $u\bar{s} / \bar{u}s$ respectively [23].

Chapter 3

Overview of experimental results

In this chapter a brief overview of experimental results from measurement of D mesons in various collision systems will be discussed. Results are from the STAR experiment at RHIC and from the ALICE and CMS experiment at LHC. Moreover published results about modification of production of J/ψ from the Cu+Au collisions at PHENIX detector at RHIC will be discussed.

3.1 Results from the STAR experiment

Production of D^0 meson at STAR was measured in numerous systems. For this overview the results from p+p collisions at $\sqrt{s} = 200$ GeV [31] [32] and Au+Au collisions at $\sqrt{s_{NN}} = 200$ GeV [33] [34] were chosen.

3.1.1 p+p results

The data sample consisted of minimum-bias p+p collisions at $\sqrt{s} = 200$ GeV from 2009. D^0 and D^{*+} were reconstructed via hadronic decay channels, ($D^0 \rightarrow K^- \pi^+$ and ($D^* \rightarrow D^0 \pi^+$). D^0 was reconstructed in the p_T intervals 0.6 - 2.0 GeV/ c and D^* 2.0 - 6.0 GeV/ c . Resulting invariant yield of D^0 is shown in Fig. 3.1.

Differential cross section for D^0 and D^{*+} were extracted as is shown in Fig. 3.2. To get charm quark production cross-section, D^0 and D^{*+} cross sections were divided by the charm quark fragmentation ratios 0.565 ± 0.032 ($c \rightarrow D^0$) and 0.224 ± 0.028 ($c \rightarrow D^+$). Results were compared to the theoretical models - FONLL (Fixed-Order-Next-to-Next-Leading Logarithm) pQCD and PYTHIA calculations. Measurements are consistent with the upper limits of FONLL pQCD calculations. For comparison, PYTHIA 6.416 with various tunes were used¹. The total charm cross section at

¹Full discussion of tunes and results is given in [31].

$\sqrt{s} = 200 \text{ GeV}$ was calculated as:

$$\sigma_{c\bar{c}} = 797 \pm 210(\text{stat.})^{+208}_{-295}(\text{sys}) \mu\text{b}$$

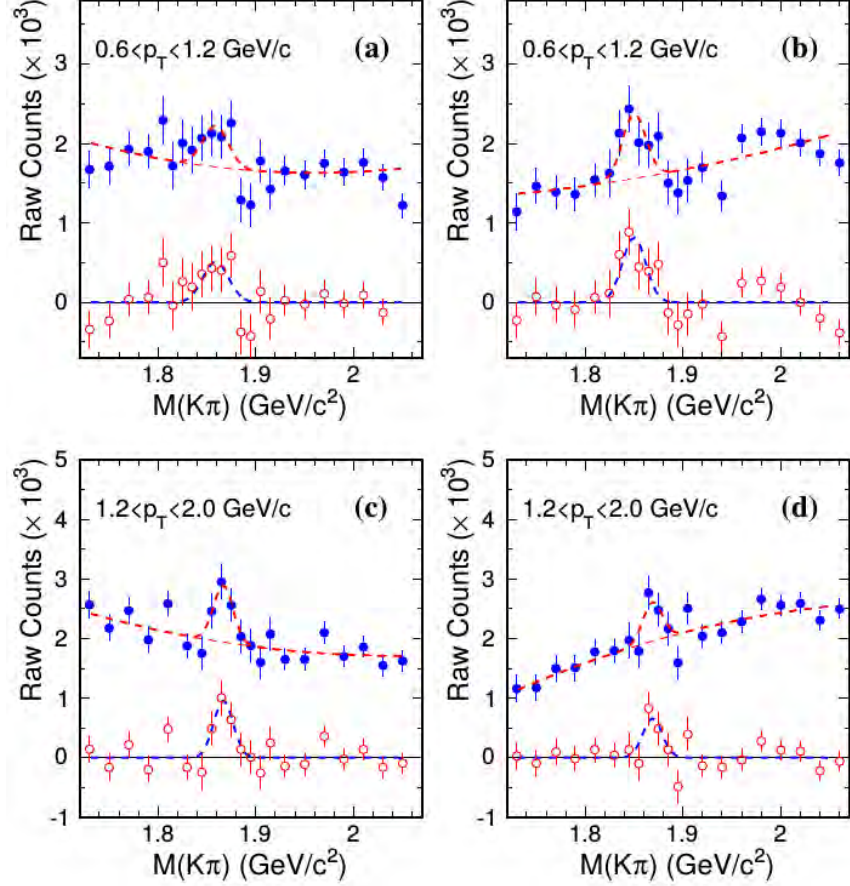


Fig. 3.1: Raw D^0 signals in different p_T bins after like-sign (panels a, c) and track-rotation (panels b, d) subtraction. Taken from Ref. [31].

In Fig. 3.3 can be seen preliminary results from p+p collisions at $\sqrt{s} = 200 \text{ GeV}$ from 2012. These results are compared with published results from 2009 [31] and FONLL.

3.1.2 Au+Au results

The data sample consisted of Au+Au collisions with $\sqrt{s_{NN}} = 200 \text{ GeV}$ from 2010 and 2011, total of $820 \cdot 10^6$ of minimum-bias and $240 \cdot 10^6$ central events were collected. D^0 production was measured via hadronic decay channels $D^0 \rightarrow K^- \pi^+$ and $\bar{D}^0 \rightarrow K^+ \pi^-$. Momentum range was $0.2 \leq p_T \leq 6.0 \text{ GeV}/c$. The D^0 meson invariant mass was reconstructed via same-event method and

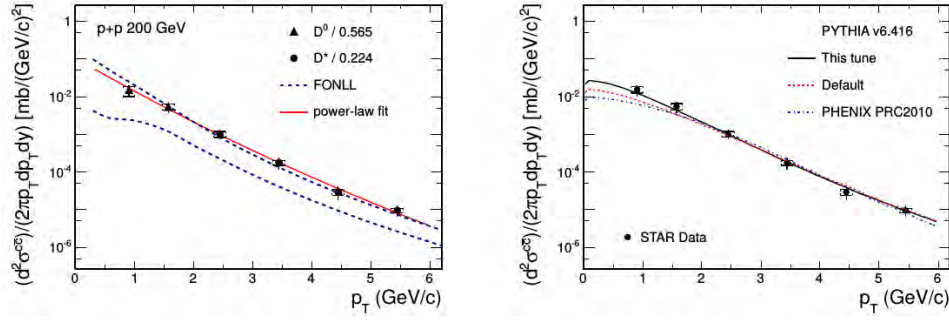


Fig. 3.2: Calculated cross section of $c\bar{c}$ with theoretical prediction - FONLL pQCD (left side) and PYTHIA (right side) Both panels shown same experimental data. Result from the PHENIX experiment are shown as the blue dotted line. Taken from Ref. [31].

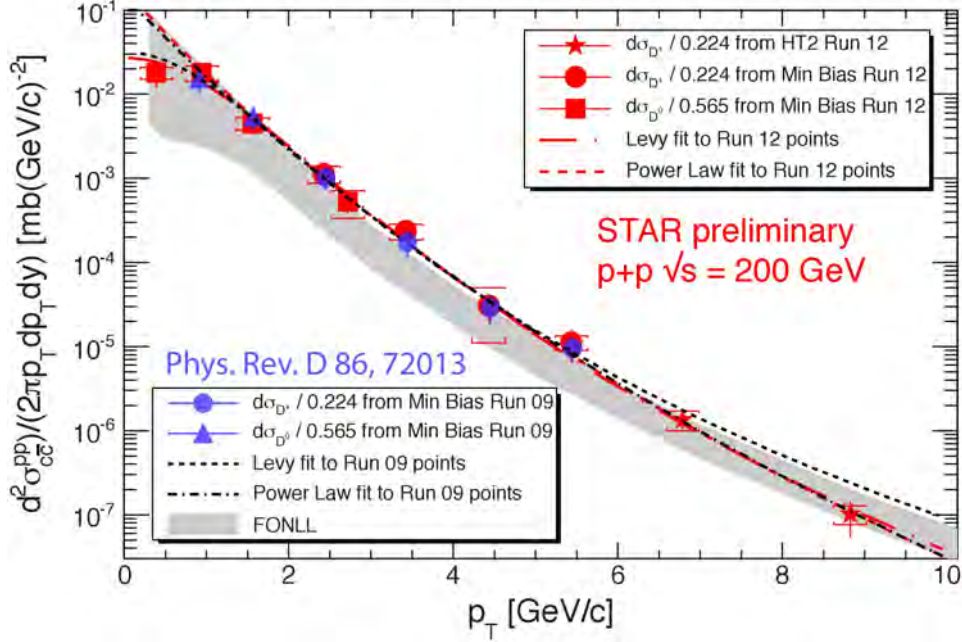


Fig. 3.3: Production cross-section of $c\bar{c}$ in p+p collisions at $\sqrt{s} = 200$ GeV from 2012 data. Blue symbols are data from 2009, red symbols are preliminary results from 2012 data. The vertical bars (brackets) represents statistical (systematic) uncertainties. Taken from Ref. [32].

combinatorial background was reconstructed via mixed-event method². Differential invariant yield of D^0 is shown at 3.4.

Fig. 3.5 shows the measured R_{AA} in D^0 in peripheral (40-80 %), central

²These methods are discussed in the Chapter 4.

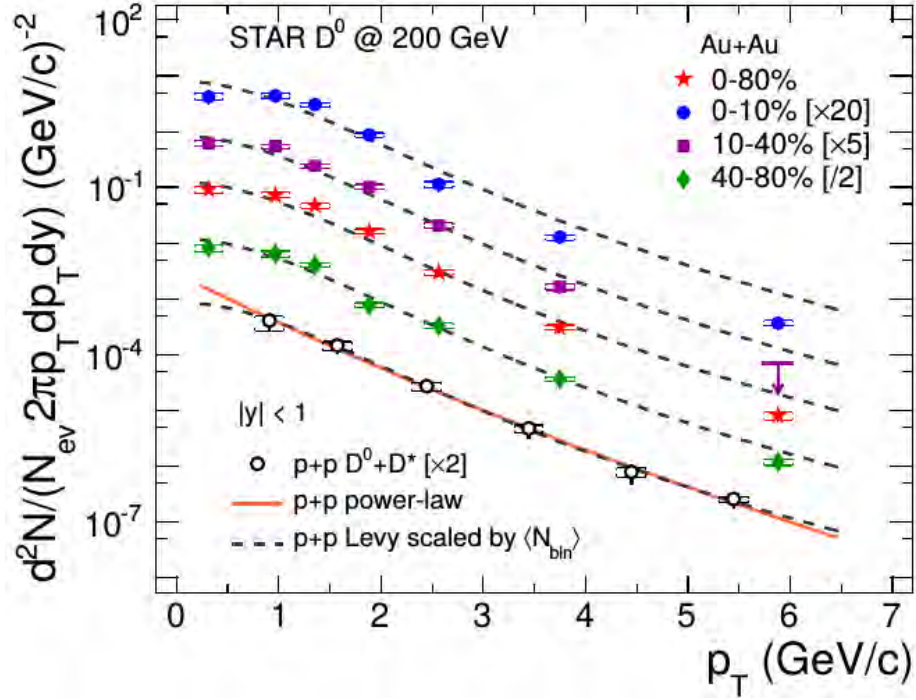


Fig. 3.4: Differential invariant yield of D^0 with centrality dependence. The solid symbols represents result from Au+Au collisions with different centrality classes, the open circles represents p+p results. Taken from Ref. [33].

(10-40%) and most central (0-10 %) Au+Au collisions. Result from most central collisions are compared to the several theoretical models. In case of the data from peripheral collisions (40-80 %) there is no clear evidence for suppression, as all results are close to unity within experimental uncertainties. For central collisions (10-40%) there is some evidence of suppression in region $p_T \geq 3.0 \text{ GeV}$. The most central (0-10 %) collisions shows clear evidence of suppression, R_{AA} is about 0.5 for $p_T \geq 3.0 \text{ GeV}/c$. These results are consistent with measurements of electron from heavy flavor hadron decays and light hadrons. These results are compared to the theoretical models: TAMU [35], SUBATECH [36], Torino [37], DUKE [38] and LANL [39].

In 2014, the HFT was fully installed within STAR, which improves the heavy flavor measuring capacity of the STAR. Result from the data analyzed with the HFT compared with the data from Run 10 and 11 are shown in Fig. 3.6. The HFT results shows similar behavior as the data from the Run 10 and 11. More importantly, both results of the D^0 meson R_{AA} follows same trend as R_{AA} of the pions in the region $p_T > 3 \text{ GeV}/c$.

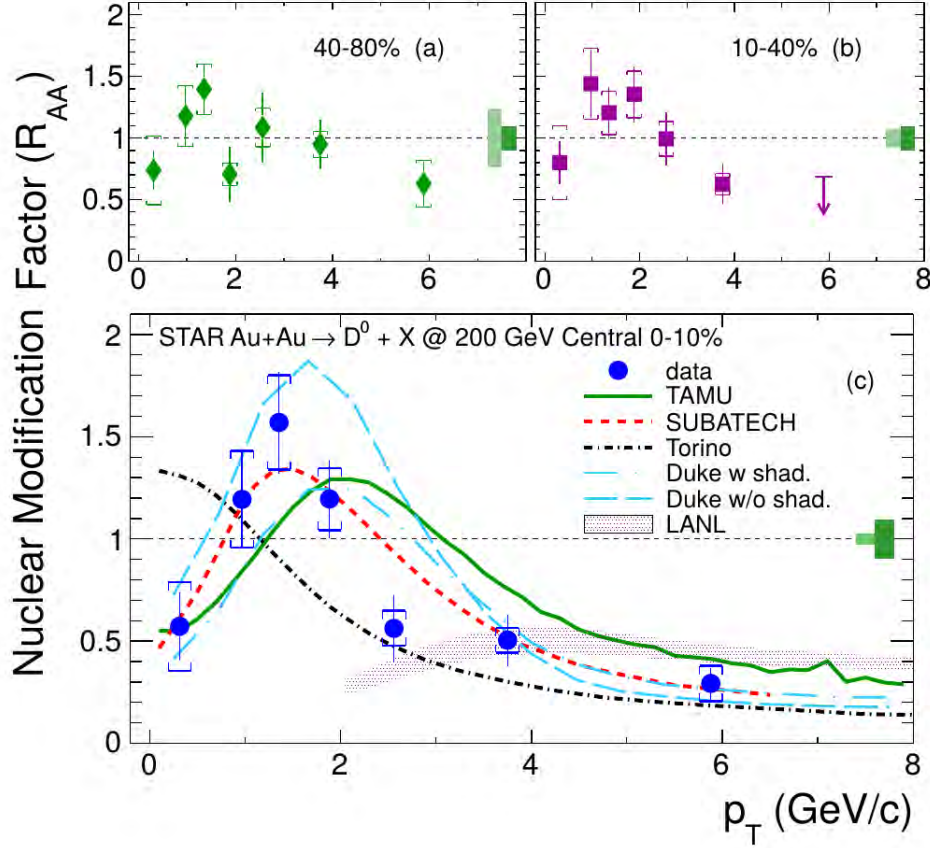


Fig. 3.5: R_{AA} of D^0 as function of p_T from Au+Au collisions for various centrality classes: 40-80% (a), 10-40% (b) and 0-10% most central collisions (c). Most central data are compared with model calculations: TAMU (solid curve), SUBATECH (dashed curve), Torino (dot-dashed curve), Duke (long-dashed and long-dot-dashed curve) and LANL groups (filled band). Taken from Ref. [33].

3.2 Results from the PHENIX experiment

At Run 12 detector PHENIX also taken data from Cu+Au collisions. Mainly modification of J/ψ have been studied - measured from leptonic decay channel. Results are shown at 3.7. Production of J/ψ at Cu+Au collisions is more suppressed than at Cu+Cu collisions but less than at Au+Au collisions.

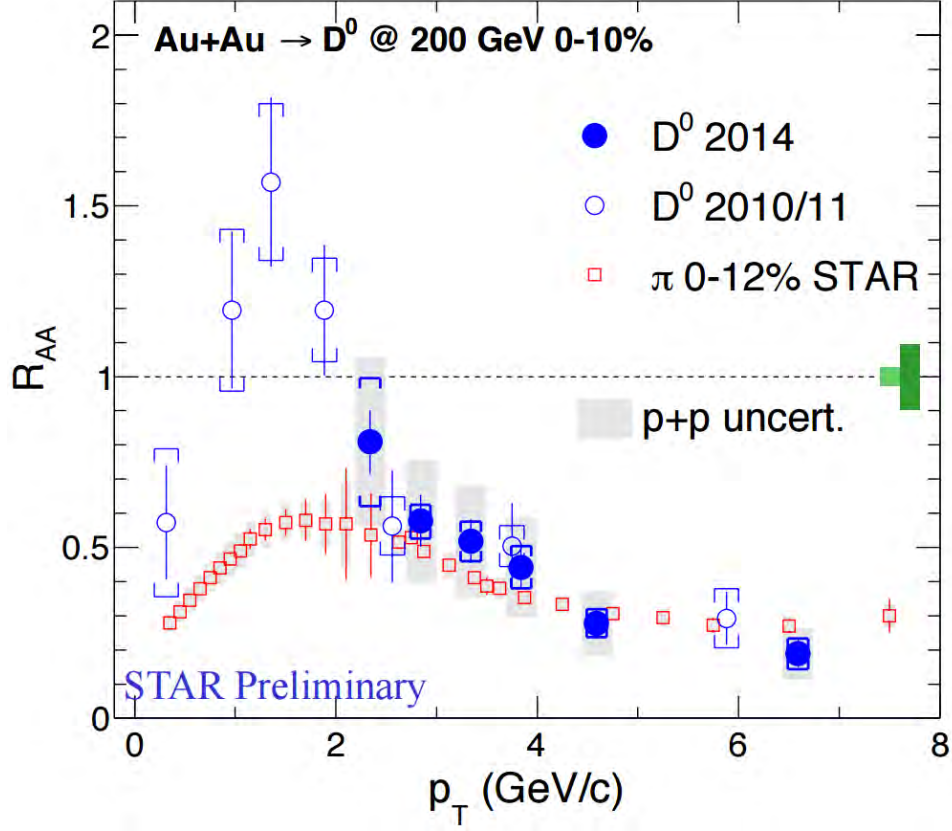


Fig. 3.6: R_{AA} of D^0 as function of p_T from the most central Au+Au collisions in comparison with R_{AA} of pions. The blue points represents data from 2010/2011, blue circles represents data taken with the HFT. Red squares represents pions from 0-12 % central collisions. Taken from Ref. [34].

3.3 Results from the ALICE experiment

The ALICE detector at LHC as dedicated heavy-ion collision experiment have same goal as STAR: study the QGP. At LHC are collided following systems: p+p, p+Pb, Pb+Pb. Maximum energy for p+p collisions is $\sqrt{s} = 13$ TeV, for Pb+Pb is $\sqrt{s_{NN}} = 5.02$ TeV. Measurement of D^0 at p+Pb and Pb+Pb collisions will be discussed. In this section the D meson stands for D^0 , D^+ , and D^{*+} mesons.

3.3.1 p+Pb results

The p+Pb collisions serves mainly as control geometry to study the *cold-nuclear matter* (CNM) effects. The CNM effects are not related to formation of QGP and originates from initial and final state effects. Following effects

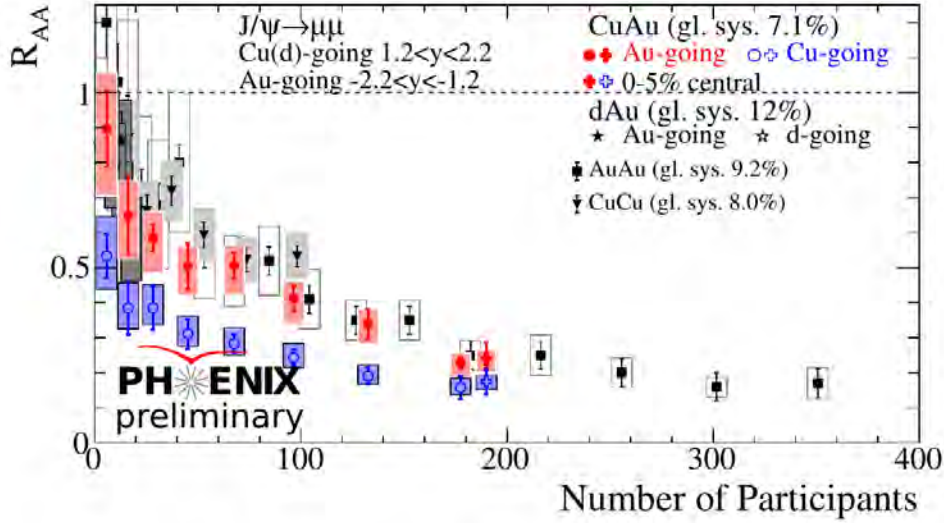


Fig. 3.7: Measurement of J/ψ R_{AA} as function of centrality in Cu+Au collisions with $\sqrt{s_{NN}} = 200$ GeV, with comparison with Au+Au, Cu+Cu and d+Au results. Taken from Ref. [40].

can be included as CNM effects [41]:

1. Initial-state nuclear effects on the parton densities. Often called as a shadowing (positive modification) and anti-shadowing (negative modification)
2. Initial-state energy loss
3. Final-state absorption on nucleons

In the case of no CNM effects, R_{AA} for p+Pb is equal to unity. If CNM effects are presents in the p+Pb collisions, then R_{AA} for p+Pb is is different from unity.

The D^0 were measured at p+Pb collisions and reconstructed via hadronic decay channel. In Fig. 3.8 are shown invariant masses of D mesons. The R_{AA} for p+Pb and differential cross section for D^0 meson are shown at 3.9, combined with data from Pb+Pb collisions. No clear evidence for suppression (or lack of suppression) is shown, as data are equivalent with unity within experimental uncertainties.

3.3.2 Pb+Pb results

In Fig. 3.10 is shown comparison of D mesons and J/ψ , from decay of B mesons (J/ψ data are result of CMS collaboration), R_{AA} as function of

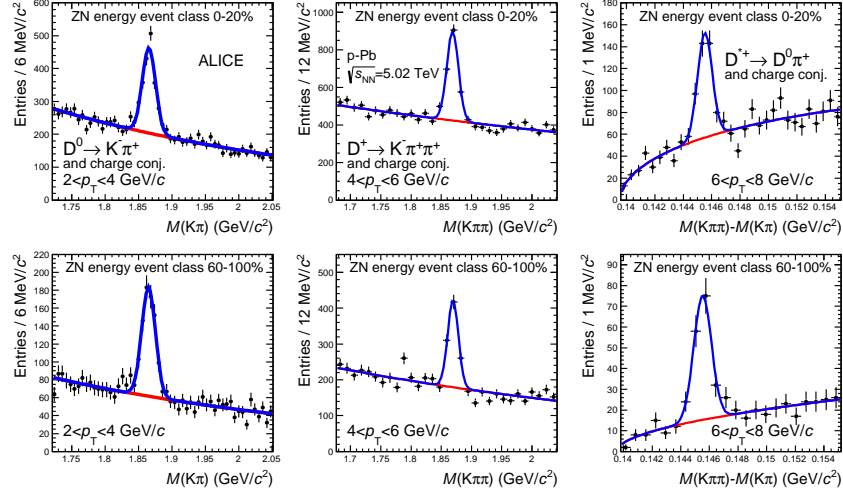


Fig. 3.8: Raw invariant mass of D^0 (left column), D^{*+} (center column), and D_s^{*+} (right column) for two centrality classes from p+Pb collisions. Taken from Ref. [42].

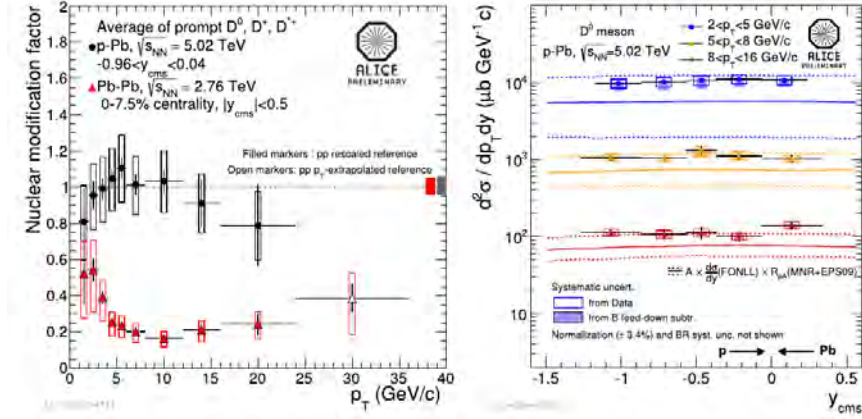


Fig. 3.9: Left panel: comparison of average D^0 , D^+ and D^{*+} nuclear modification factors R_{pA} measured in p+Pb collisions and in the 0–7.5% most central Pb+Pb collisions as a function of p_T . Right panel: differential cross section for D^0 meson as a function of center-of-mass rapidity y_{CMS} . The continuous and dashed lines represent expectations based on pQCD calculations including EPS09 parametrization of nuclear PDF. Taken from Ref. [43].

centrality. These results indicate stronger suppression for D mesons (charm quark respectively) than for production of bottom quark in central Pb+Pb collisions. Kinematic region was chosen in order to have similar kinematic

range for D mesons as for J/ψ .

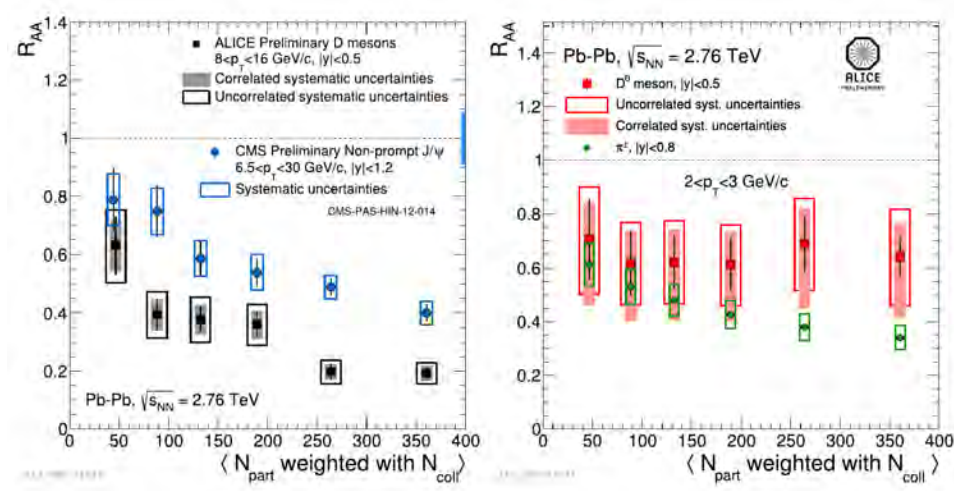


Fig. 3.10: Comparison of R_{AA} as function of centrality for D mesons and J/ψ for Pb+Pb collisions. Left panel: Kinematic range $8 < p_T < 16$ GeV for D mesons and $6 < p_T < 30$ GeV/c for J/ψ from B meson decays. Right panel: R_{AA} of D mesons and charged pions in $2 < p_T < 3$ GeV/c for Pb+Pb collisions. Taken from Ref. [43].

The Fig. 3.11 shows R_{AA} of the D mesons for two centrality classes, 0-10 % and 30-50 %, as a function of the p_T . In the most central collisions the R_{AA} is lower than 1 for the full p_T range and the highest suppression is achieved in the range $8 < p_T < 12$ GeV/c, where the mean value of R_{AA} is $R_{AA} \sim 0.15$. For semi-central collisions, 30-50 %, R_{AA} of charmed mesons is consistent with unity within experimental uncertainties. For increasing p_T the R_{AA} decrease below to $R_{AA} \sim 0.35$ in the range $6 < p_T < 8$ GeV/c.

In Fig. 3.12 is shown R_{AA} of the D mesons and light hadrons for two centrality classes, 0-10 % and 30-50 %, as the function of the p_T .

3.4 Results from the CMS experiment

The CMS detector at the LHC is a multi-purpose detector mainly focused on measuring detailed properties of the Higgs boson in proton-proton collisions and searching for new particles and physics beyond the Standard model.

Results from the CMS measurement of the D^0 meson are shown in Fig. 3.13. These results follow a similar pattern as results from the ALICE experiment. For the lower p_T D^0 mesons are suppressed less than light hadrons, but for $p_T > 10 \text{ GeV}/c$ suppression of light hadrons and D^0 mesons is the same within experimental uncertainties. Data are compared to the two theoretical models [45] and [46].

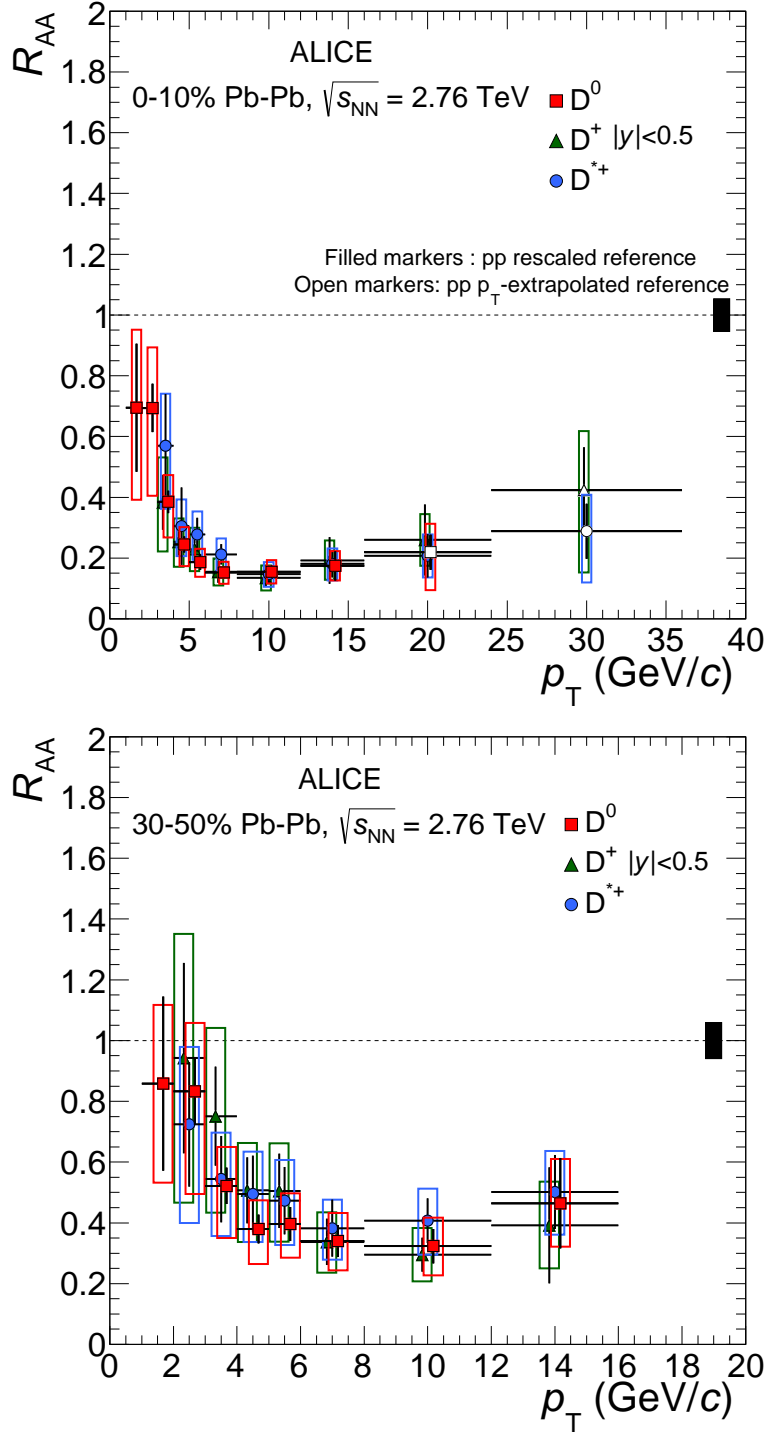


Fig. 3.11: R_{AA} of prompt D^0 , D^+ , and D^{*+} mesons for the 0-10 % (left) and 30-50 % (right) centrality classes. Statistical (bars), systematic (empty boxes), and normalization (shaded box) uncertainties are shown. Horizontal bars represent bin widths. D^0 symbols are placed at the centre of the bin. D^+ , and D^{*+} are shifted for visibility. Taken from Ref. [44].

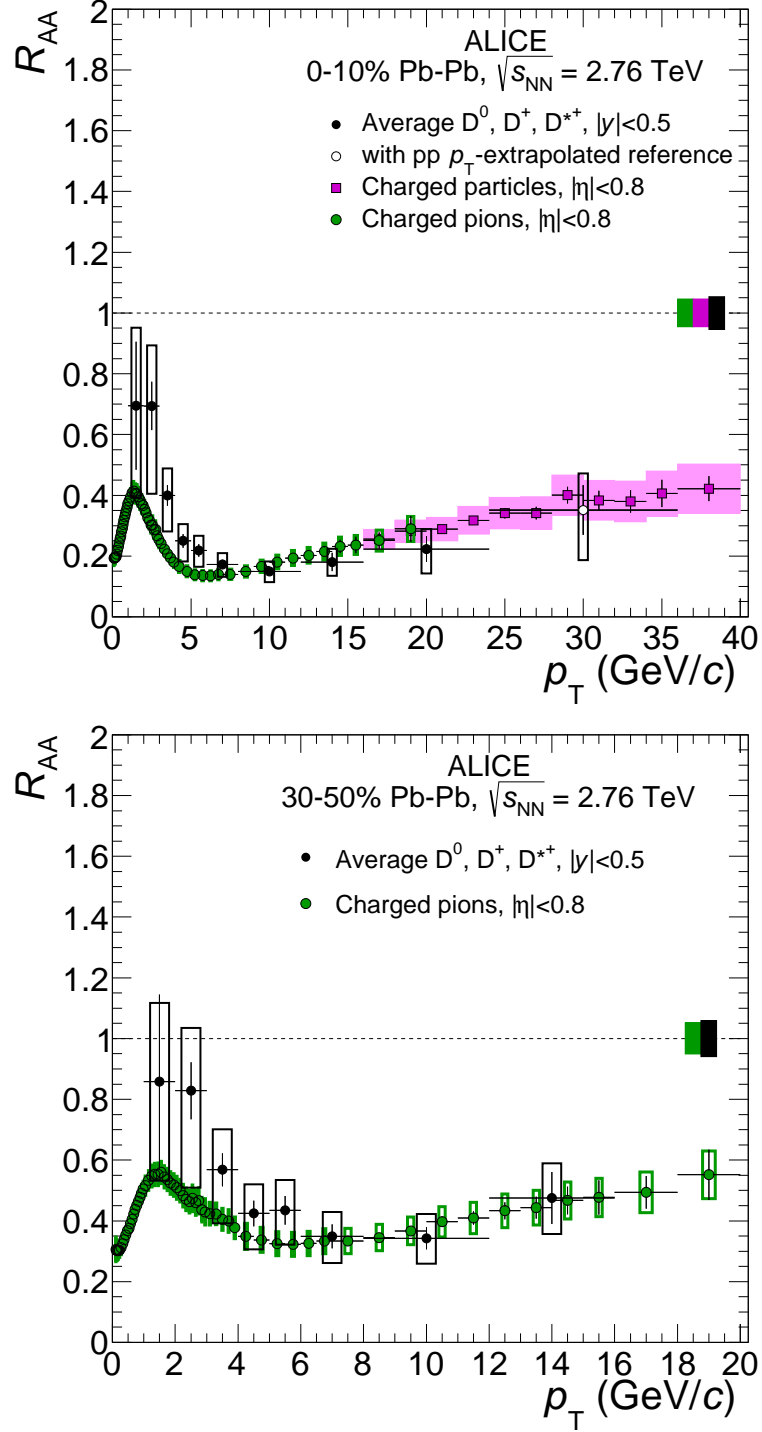


Fig. 3.12: Prompt D-meson R_{AA} (average of D^0 , D^+ and D^{*+}) as a function of p_T compared to the nuclear modification factors of pions and charged particles in the 0-10 % (upper panel) and 30-50 % (lower panel) centrality classes. Statistical (bars), systematic (empty boxes), and normalization (shaded box at $R_{AA} = 1$) uncertainties are shown. Horizontal bars represent bin widths. Symbols are placed at the center of the bin. Taken from Ref. [44].

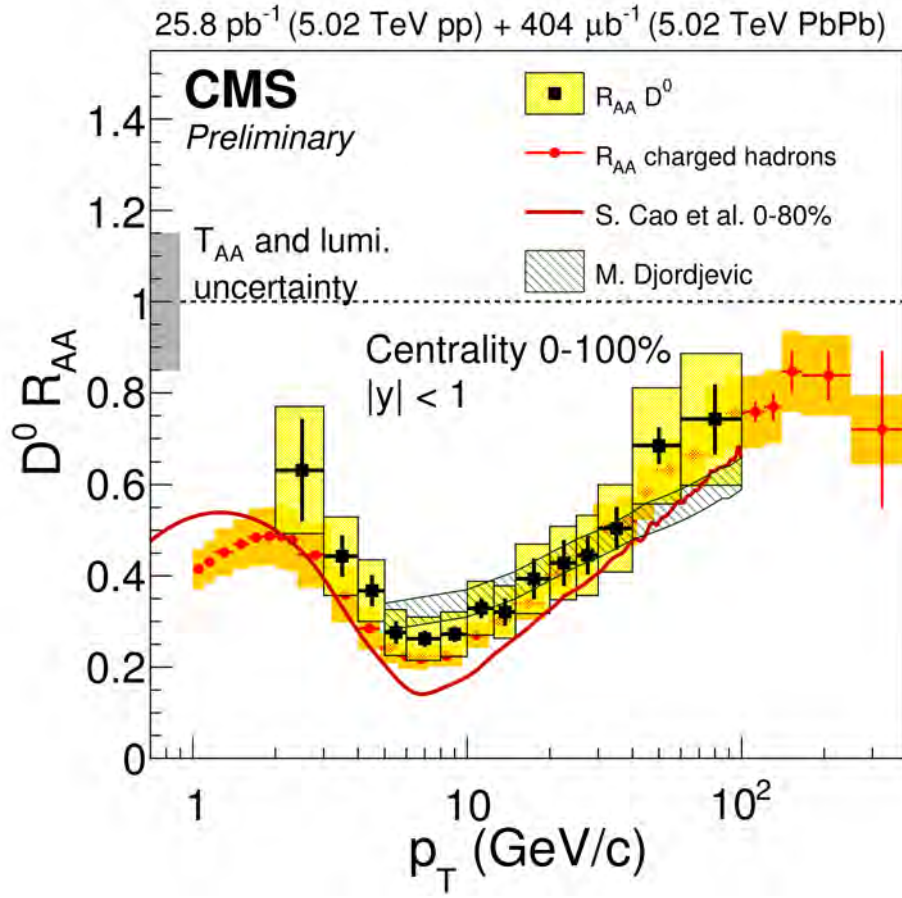


Fig. 3.13: $D^0 R_{AA}$ as a function of p_T from CMS. Black points represents R_{AA} of D^0 mesons, red points represents R_{AA} of light charged hadrons. Data are compared with the two theoretical models [46] and [45]. Taken from Ref. [47].

Chapter 4

Analysis of Cu+Au experimental data

This chapter describes reconstruction of D^0 meson invariant mass in the hadronic decay channel $D^0 \rightarrow K^- \pi^+$ with the branching ratio $\Gamma = 3.89\%$ [23]. D^0 and \bar{D}^0 are analyzed together for achieving a higher statistics. At first, chosen data set will be described and then applied kinematic cuts. Also methods used for identification of background and potential candidates for D^0 meson will be discussed as well. Last part of this chapter show the obtained raw yield of D^0 meson in Cu+Au collisions.

4.1 Event and track selection

Data used for this analysis were taken at RHIC during Cu+Au collisions run at 2012. Centre-of-mass energy per nucleon pair for Cu+Au collisions was $\sqrt{s_{NN}} = 200$ GeV and total integrated luminosity of recorded Cu+Au data is $\mathcal{L}_{\text{total}} = 27 \text{ nb}^{-1}$.

Minimum bias (MB) trigger data are used with $N_{\text{events}} = 70 \times 10^6$ which are only about 1/3 of recorded Cu+Au data. The minimum bias (MB) trigger used for this analysis, is defined as a coincidence between two VPD (East and West VPD) and two ZDC (East and West ZDC) sub-detectors, and an online collision vertex cut.

Data set criteria for event selection are listed below:

1. Name of production: P15ie (june 2015)
2. Used trigger: vpd-zdce-tac-protected
3. $|V_{zTPC}| < 30 \text{ cm}$
4. $|V_{zVZD} - V_{zTPC}| < 3 \text{ cm}$

5. Multiplicity > 8

Number of events after cuts: 59M events

Track selection criteria:

1. $|\eta| < 1$
2. $0 < TrackFlag < 1000$
3. Number of Fit Points ≥ 20
4. $\frac{Number\ of\ TPC\ fit\ points}{Number\ of\ possible\ TPC\ fit\ points} \leq 0.52$
5. gDCA $< 2.0\ cm$
6. $p_{T,min} > 0.2\ GeV$

where cut for pseudorapidity η is due to geometry of TPC and TOF sub-detectors. *TrackFlag* is a parameter which is used to remove potential track splitting from recorded data. *Number of fit points* denotes the number of hit points of given track in the TPC which are used for reconstruction of this track. Ratio of *Number of fit points* and *Number of possible TPC fit points* is used to prevent that one track is reconstructed as two tracks. Global Distance of Closest Approach (gDCA) represents a distance when a track is closest to the primary vertex. Minimal value of p_T is set for track being able to reach TPC and TOF.

4.2 Quality assurance

One of the first steps of new analysis is to check basic quality of selected data. This includes check of multiplicity run-by-run, reference multiplicity, vertices and more. Based on the results of quality assurance bad runs are identified and they are not included in the analysis itself. Figures Fig. 4.1 and Fig. 4.2 shows distribution of Vz_{TPC} vertex or DCA, respectively. In the case of Vz_{TPC} a little shift to the positive values can be seen. This shift is due to slight changes of parameters during data taking.

In Fig. 4.3 can be seen reference multiplicity of Cu+Au collisions. These results are consistent with theoretical predictions. Results from the Glauber model and corresponding division into the centrality classes¹ are shown at Tab. 4.1.

Fig. 4.4 shows dependence of the TOF multiplicity on reference multiplicity after applying following cuts:

¹These calculations are results of the STAR collaboration

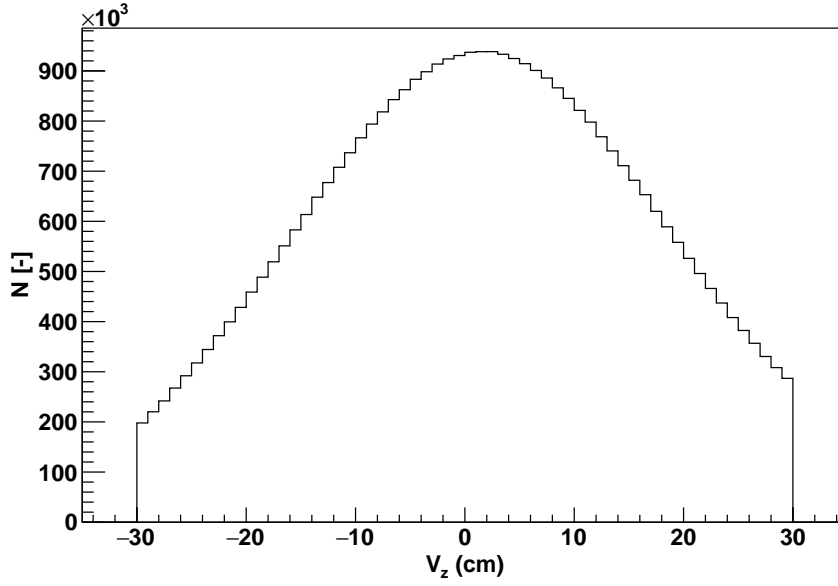


Fig. 4.1: Distribution of V_z TPC. The Y-axis represents number of events.

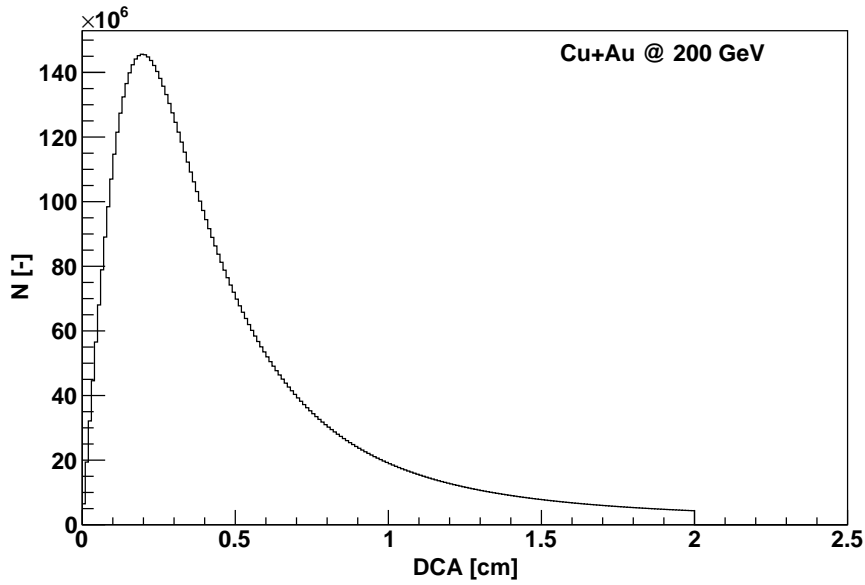


Fig. 4.2: Distribution of DCA for all particles. The Y-axis represents number of events.

1. Cut 1: TOF multiplicity $< 95 + 5.3 \times$ Reference multiplicity
2. Cut 2: TOF multiplicity $> 65 + 2.8 \times$ Reference multiplicity

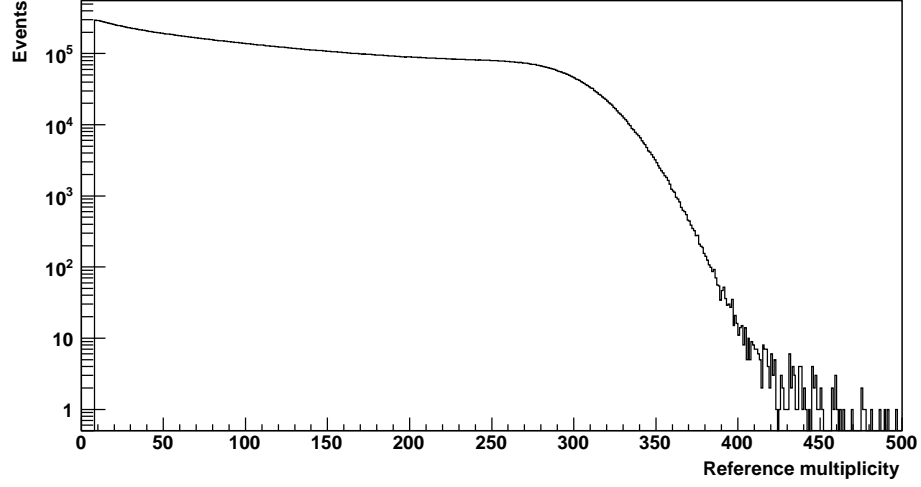


Fig. 4.3: Reference multiplicity of Cu+Au collisions. The Y-axis is drawn in logarithm scale.

Centrality class	Ref. multiplicity
0-5 %	273
5-10 %	235
10-20 %	170
20-30 %	118
30-40 %	78
40-50 %	49
50-60 %	29
60-70 %	16
70-80 %	8

Tab. 4.1: Definiton of centrality classes in dependence on reference multiplicity. Results are from the Glauber model for Cu+Au collisions. Values are the mean value in the centrality class.

4.3 Identification of pions and kaons

For particle identification in this analysis the TOF and TPC are used. Due to performance of TOF, it is used for identification at lower p_T (up to 2 GeV/ c).

For particle identification by TOF, global tracks are projected to TOF and geometrically corresponding TOF channel is linked to it. Result of TOF is velocity of the particle β .

Particle identification in the TPC is done via particle energy loss per unit length dE/dx . Method of so-called *truncated mean* is used. This method

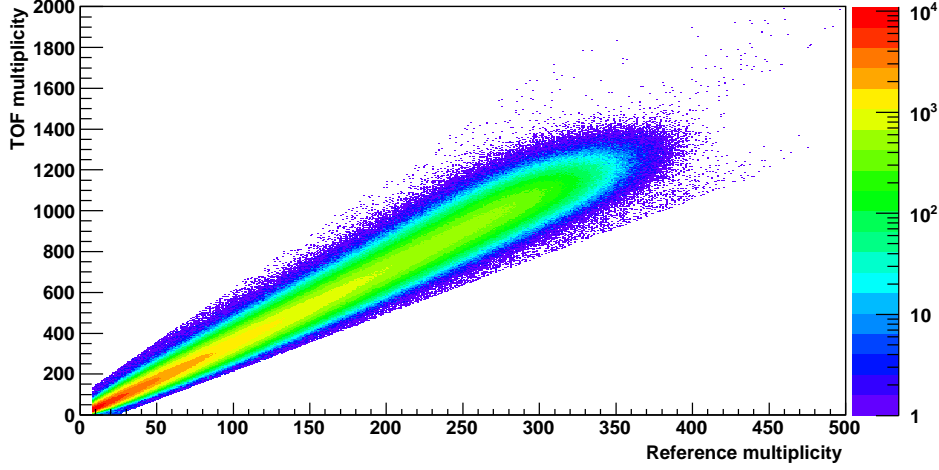


Fig. 4.4: TOF multiplicity as function of reference multiplicity.

discarded hits with the top 30% of high dE/dx values. Average values from the rest of the tracks are then used for derivation of mean dE/dx of the track. Resolution of TPC for minimum ionizing particle is about 6-8 % for the track with maximum of 45 sampled dE/dx points.

For identification normalized functions $n\sigma_X^{1/\beta}$ $n\sigma_X^{dE/dx}$ are used and they are defined as:

$$n\sigma_X^{1/\beta} = \frac{\frac{1}{\beta^{meas}} - \frac{1}{\beta_X^{th}}}{R^{1/\beta}} \quad (4.1)$$

$$n\sigma_X^{dE/dx} = \frac{1}{R^{dE/dx}} \ln \frac{\langle dE/dx \rangle^{meas}}{dE/dx_X^{th}} \quad (4.2)$$

where X denotes type of particle, $\langle dE/dx \rangle$ is mean ionization losses in the TPC, $R^{1/\beta}$ and $R^{dE/dx}$ are corresponding resolutions. Index *meas* indicates measured values, index *th* denotes theoretical values of variables. In this analysis X always will be pion π or kaon K. Identification of both types of particles is more thoroughly described below.

4.3.1 PID of K mesons

Applied cuts for identification of kaons:

1. $p_T > 0.2 \text{ GeV}/c$
2. $|n\sigma_K^{1/\beta}| < \text{variable, see Fig. 4.6}$
3. $|n\sigma_K^{dE/dx}| < 2$

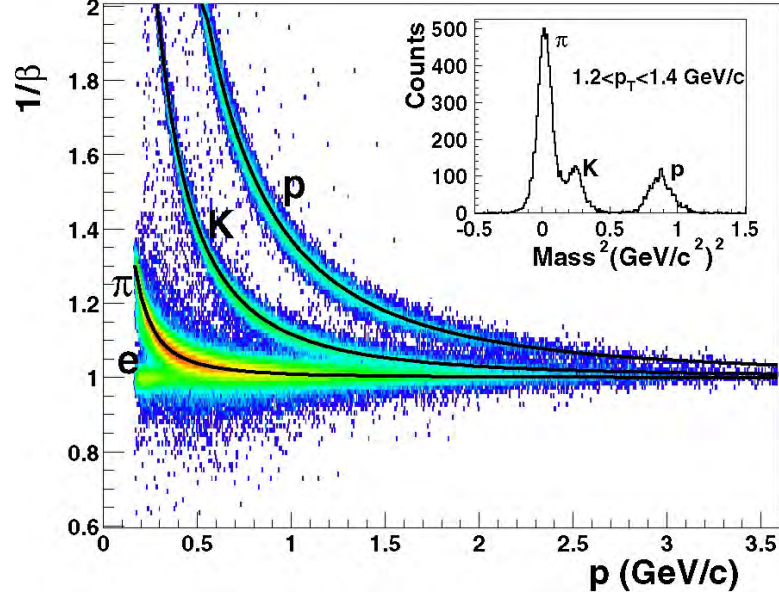


Fig. 4.5: Particle identification via TOF. Data from Au+Au collisions. Taken from Ref. [48]

4. $p_T < 1.6$ GeV/c: TOF used
5. $p_T > 1.6$ GeV/c: Hybrid PID used

Process of identification of kaons is shown at two figures: Fig. 4.6 shows obtained signal from TOF before applying cuts with lines depicting cuts and Fig. 4.7 shows signal from TPC with depicted cuts. For the lower p_T up to 1.6 GeV/c signal from the TOF was used for the PID. For $p_T > 1.6$ GeV/c the Hybrid PID was used. Hybrid PID using primarily signal from the TPC for PID and, if available, signal from the TOF. If signal from the TOF is not available, then only a TPC information is used. With this method better purity of signal is achieved than with the strict division into the TPC and TOF PID regions.

4.3.2 PID of π mesons

Applied cuts for pions PID are listed below:

1. $p_T > 0.2$ GeV/c
2. $|n\sigma_\pi^{dE/dx}| < 2$
3. For all p_T : TPC used

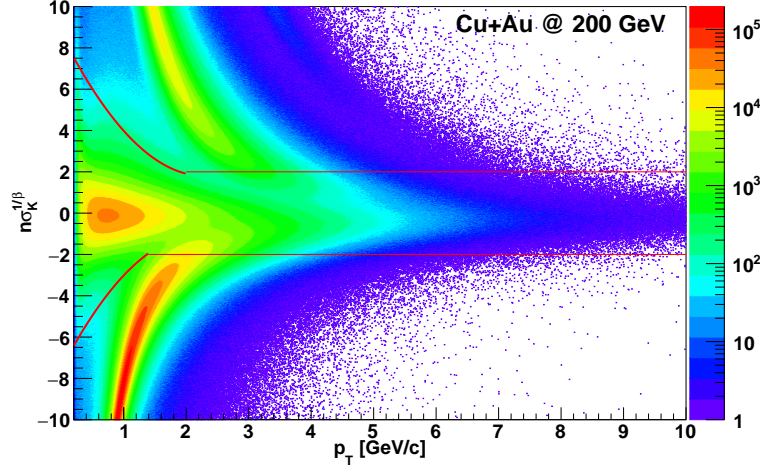


Fig. 4.6: Particle identification of kaons via TOF before applying cuts. The red lines shows the variable cut for the $|n\sigma_K^{1/\beta}|$

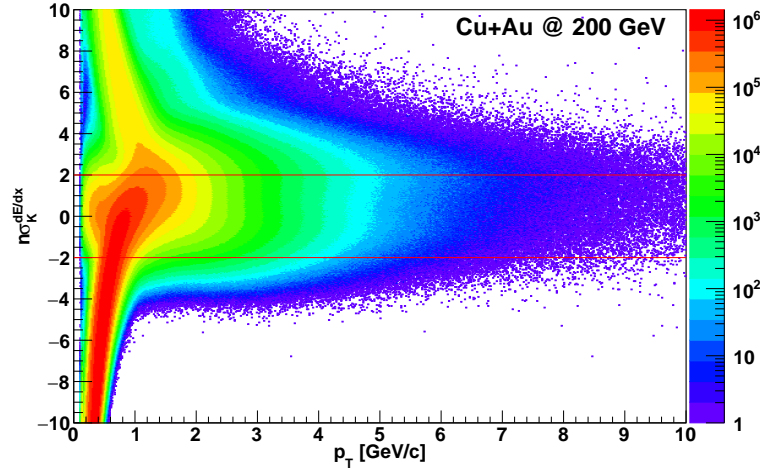


Fig. 4.7: Particle identification of kaons via TPC. The red lines indicated the cut $|n\sigma_K^{dE/dx}| < 2$.

The p_T distribution of π mesons is shown in Fig. 4.8. This distribution has a clearly exponential decrease with total majority of pions falls into the p_T up to 1.5 GeV/c where lies main resolution interval of the TPC. Due to TOF efficiency for pions and due to low statistics, using TOF for pions PID was ruled-out. More about TPC and TOF efficiency for pions is discussed in the Chapter 5. In Fig. 4.9 is shown PID of pions in TPC.

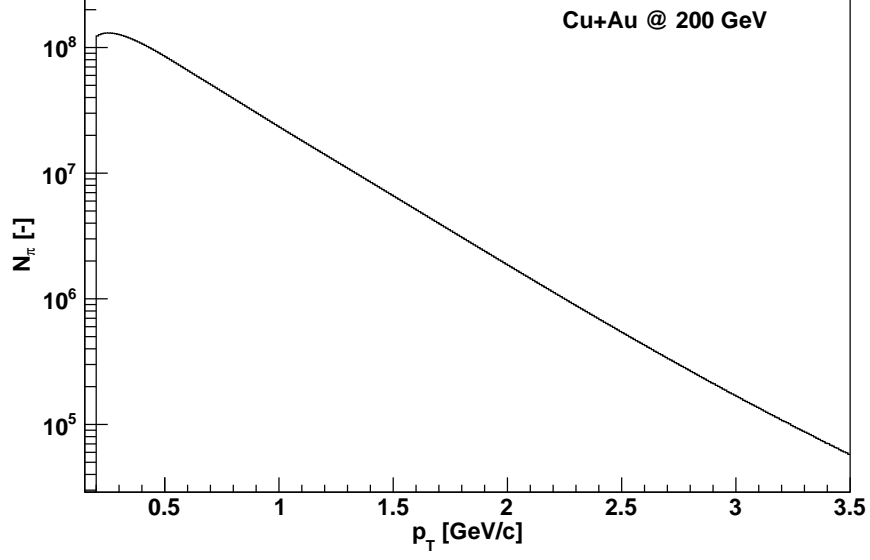


Fig. 4.8: The p_T distribution of pions. The Y-axis represent the number of pions and is drawn in logarithm scale.

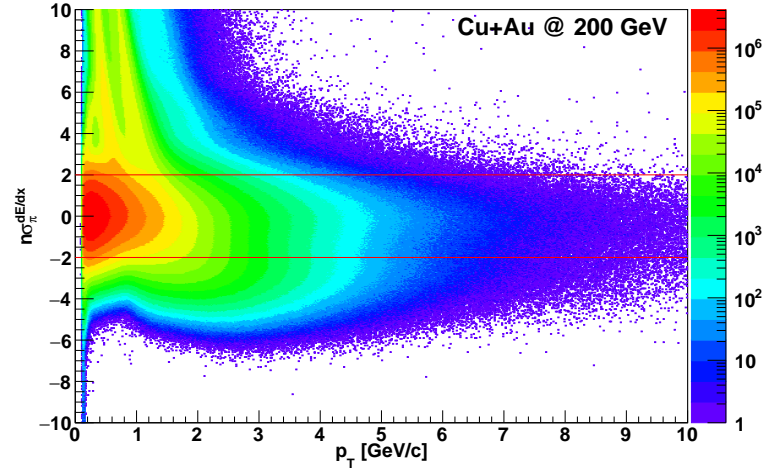


Fig. 4.9: Particle identification of π mesons via dE/dx as function of p_T . Red lines indicated area of the cuts for the $|n\sigma_\pi^{dE/dx}| < 2$.

4.4 Methods of background reconstruction

Before the signal of the D^0 candidate can be analyzed, combinatorial background have to be identified and subtracted from data. For the subtraction

of combinatorial background three methods are used in this analysis:

1. Like-sign method (LS)
2. Mixed-event method (ME)
3. Rotated momentum method (ROT)

Main method used for background subtraction in this analysis is the Mixed-event algorithm while Like-sign and Rotated momentum algorithms are used as a control methods for cross-check of the results.

4.4.1 Like-sign method

The like-sign method paired uncorrelated $K\pi$ pairs of the same charge from the same event. The LS $K\pi$ pairs invariant mass distribution is calculated as [49]:

$$N_{\text{Like-sign}}(m) = 2 \times \sqrt{N_{K_1^+ \pi_1^+}(m) \times N_{K_1^- \pi_1^-}(m)} \quad (4.3)$$

where $N_{\text{Like-sign}}$ is the geometric mean of the number of the like-sign pairs $N_{K_1^+ \pi_1^+}$ and $N_{K_2^- \pi_2^-}$ with the mass m .

The number of D^0 candidates with mass m is then calculated as:

$$N_{D^0}(m) = N_{K_1^+ \pi_1^-}(m) + N_{K_1^- \pi_1^+}(m) - N_{\text{Like-sign}}(m) \quad (4.4)$$

Advantage of the like-sign method is that signal and background are taken from the same event and therefore there is no difference between those two distributions due to, for example, collective effects as a flow. Disadvantage of this method lies in the need of a large data set because statistics in this method is driven by the number of produced kaons and pions in the event [10].

4.4.2 Mixed-event method

One possible approach how to enhance the like-sign method is to increase number of possible like-sign pairs combinations without need of bigger data-set. Mixed-event method combines a unlike-sign $K\pi$ pairs from different events and possible combinations are: $K_i^+ \pi_j^-$, $K_i^- \pi_j^+$, $K_j^+ \pi_i^-$, $K_j^- \pi_i^+$, where subscript i or j denotes the mixed-event with the condition $i \neq j$.

To keep similar characteristic of mixed-events, the data sample was divided into 10 bins in charged particles multiplicity and 10 bins in collisions vertex along the direction of the beam. Only pairs from events with same multiplicity and vertex position were mixed.

4.4.3 Rotated momentum method

Rotated momentum method paired each pion candidate with the kaon candidate with reversed 3-momentum. Track rotation technique is based on the assumption that by rotating one of the daughter track for 180 degree the kinematics of decay is destroyed and thus the distribution of a pair invariant mass with one track rotated is able to reproduce the random combinatorial background [10].

4.5 Raw D^0 yield

Next step, after identification of pions, kaons and combinatorial background, is extraction of raw signal of the D^0 candidates. This extraction is done for all three methods of background estimation.

Fig. 4.10 shows raw yield of D^0 candidates obtained by mixed-event method, Fig. 4.11 shows raw yield obtained by like sign-method and Fig. 4.12 shows raw yield of D^0 mesons obtained by rotated momentum method.

After subtraction of combinatorial background, signal was fitted by Gaussian and residual background by linear function. Overview of raw yield by various method is shown in 4.2. Mean of Gaussian within errors from all method is consistent with the PDG value $1.86483 \pm 0.00014 \text{ GeV}/c^2$ [23]. Signal from D^0 mesons candidates is shown in all figures.

Method	Raw yield	Mean [GeV/c^2]
Mixed-event	172000 ± 36000	1.863 ± 0.004
Like-sign	124000 ± 47000	1.863 ± 0.009
Rotated momentum	188000 ± 47000	1.864 ± 0.004

Tab. 4.2: Overview of D^0 meson raw yield by mixed-event method, like-sign method and rotated momentum method. Mean is a mean of the Gaussian fit which corresponding with the invariant mass.

After obtaining raw yield in the full range of p_T , the p_T interval was divided into the several subintervals, which were analyzed separately. Due to weak signal and high background only for one p_T bin, $0.8 < p_T < 2.0 \text{ GeV}/c$, signal can be extracted. Resulting signal, is shown in Fig. 4.13. Raw yield, calculated by the bin counting method, of the D^0 meson is: 132000 ± 28000 . Mean of Gaussian fit is: $1.863 \pm 0.003 \text{ GeV}/c^2$.

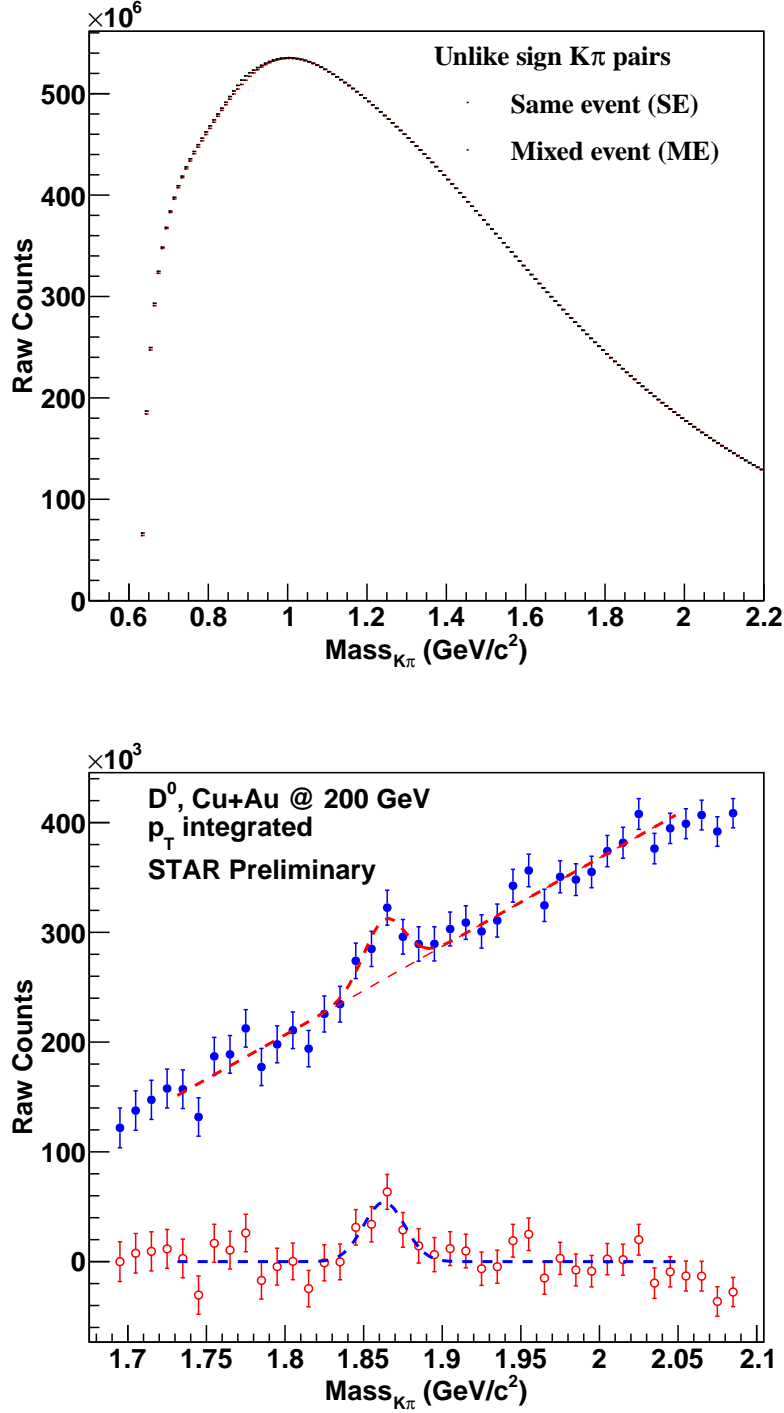


Fig. 4.10: Raw Yield of D^0 meson candidates - Mixed-event method. Upper panel: Invariant mass distribution of $K\pi$ pairs. Same event distribution is displayed by black dots, the mixed event distribution by red dots. Lower panel: Invariant mass in region of D^0 mesons. Background is fitted by linear function, signal is fitted by Gaussian. The blue points represents signal with residual background, red open points represent signal after the subtraction of the residual background.

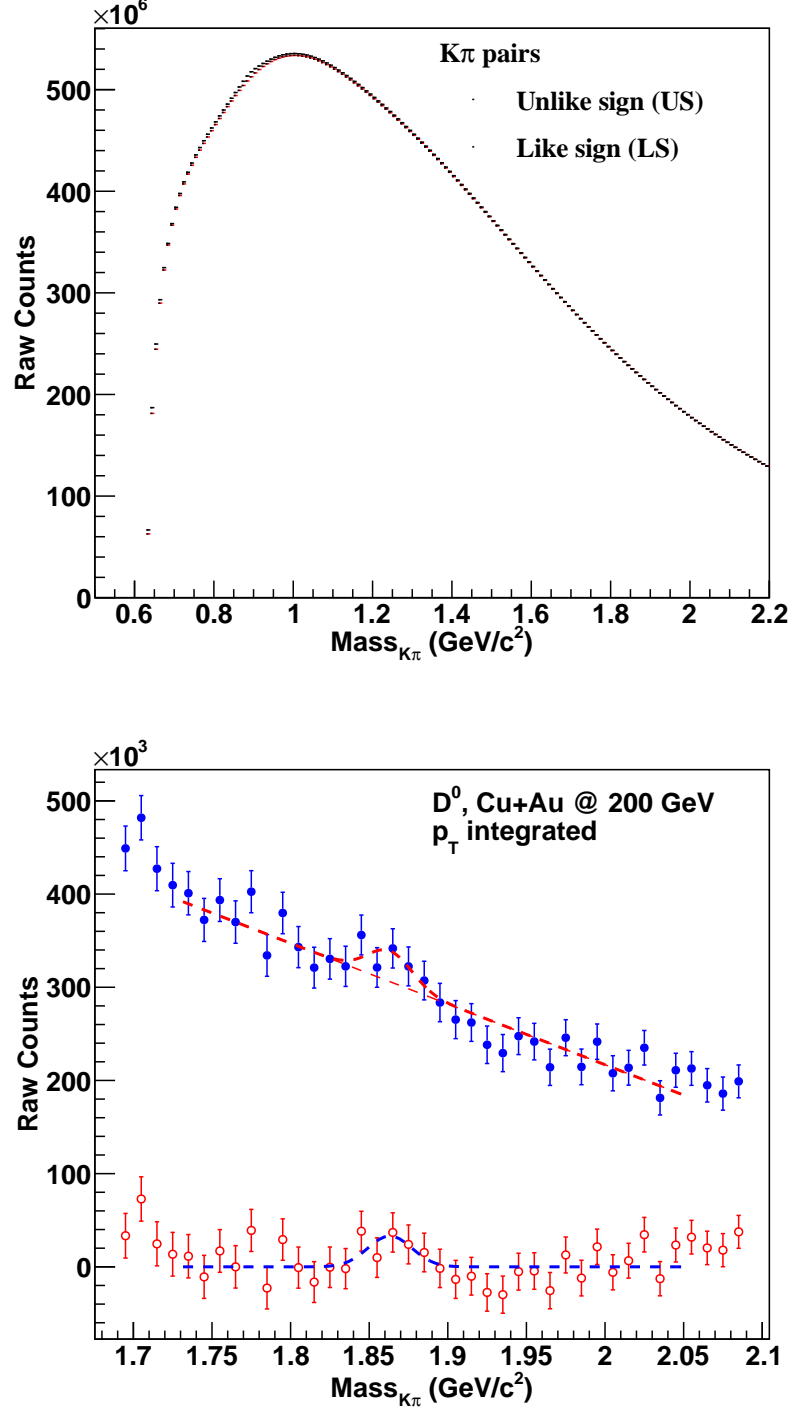


Fig. 4.11: Raw Yield of D^0 meson - LS method. Upper panel: Invariant mass distribution of $K\pi$ pairs. Unlike sign distribution is displayed by black dots, the like-sign distribution by red dots. Lower panel: Invariant mass in region of D^0 mesons. Background is fitted by linear function, signal is fitted by Gaussian. The blue points represents signal with residual background, red open points represent signal after the subtraction of the residual background.

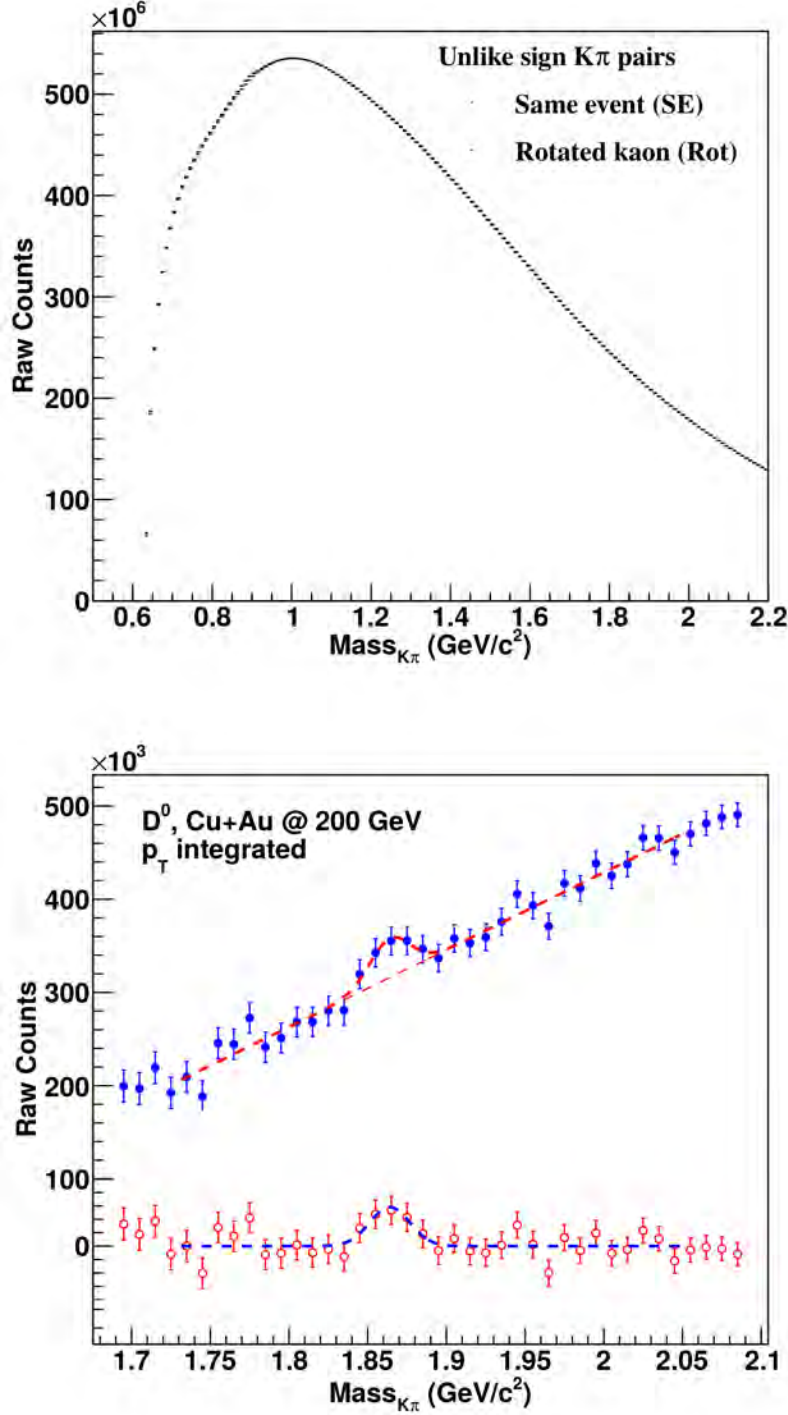


Fig. 4.12: Raw Yield of D^0 meson - ROT method. Upper panel: Invariant mass distribution of $K\pi$ pairs. Same event distribution is displayed by black dost, rotated momentum distribution by red dots. Lower panel: Invariant mass in region of D^0 mesons. Background is fitted by linear function, signal is fitted by Gaussian. The blue points represents signal with residual background, red open points represents signal after subtraction of residual background.

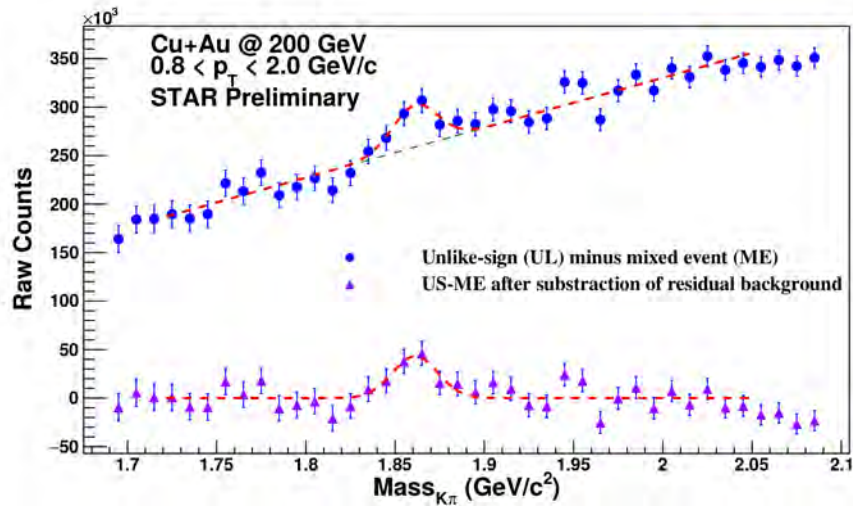


Fig. 4.13: Invariant mass distribution of $K\pi$ pairs in the p_T bin $0.8 < p_T < 2.0 \text{ GeV}/c^2$. The blue points represent signal obtained by subtraction of mixed-event (ME) background from unlike-sign (US) signal. The blue dotted line represents fit of residual background. The violet triangles represent obtained signal after the subtraction of the residual background. Raw yield, calculated by the bin counting method, of the D^0 meson is: 132000 ± 28000 . The mean of Gaussian fit is: $1.863 \pm 0.003 \text{ GeV}/c^2$.

Chapter 5

Detector Efficiencies

In order to obtain invariant yield spectrum of the D^0 meson, the raw spectrum need to be corrected for the detector effects and efficiencies. This chapter will describe process how each one of detector efficiencies for kaons and pions was obtained. At first the TOF efficiency (ϵ_{π}^{TOF} and ϵ_K^{TOF}) will be described. Second part of this chapter will describe tracking efficiency of the TPC, the ϵ_{π}^{TPC} and the ϵ_K^{TPC} . Last part of this chapter will shown total reconstruction efficiency of the D^0 meson for the 0-80 % centrality Cu+Au collisions at $\sqrt{s_{NN}} = 200$ GeV.

5.1 TOF efficiency

TOF efficiency for pions and kaons was enumerated according to following equation:

$$\epsilon_X^{TOF} = \frac{N_X^{TOF}}{N_X^{TPC}} \quad (5.1)$$

where X denotes pions or kaons respectively. Initial p_T distributions of pions in the TPC and TOF is show in Fig. 5.1, Fig. 5.2. The p_T distribution of kaons in the TPC and TOF is shown in Fig. 5.3 and in Fig. 5.4, respectively.

Final result of the ϵ_K^{TOF} for kaons is shown in Fig. 5.5. The ϵ_K^{TOF} is behave mostly as can be expected, with quick rise of efficiency with the rising p_T of the kaons and then the ϵ_K^{TOF} is mostly constant for the large p_T region. Small bump that can be observed in the small p_T region is due to the signal contamination by the pions. Fluctuations in the high p_T region are due to low statistics of kaons in this area.

The final settings of the PID cuts for the pions does not include TOF, but for understanding why using the TOF was ruled off, there is a need to look at the values of the ϵ_{π}^{TOF} and subsequently ϵ_{π}^{TPC} .

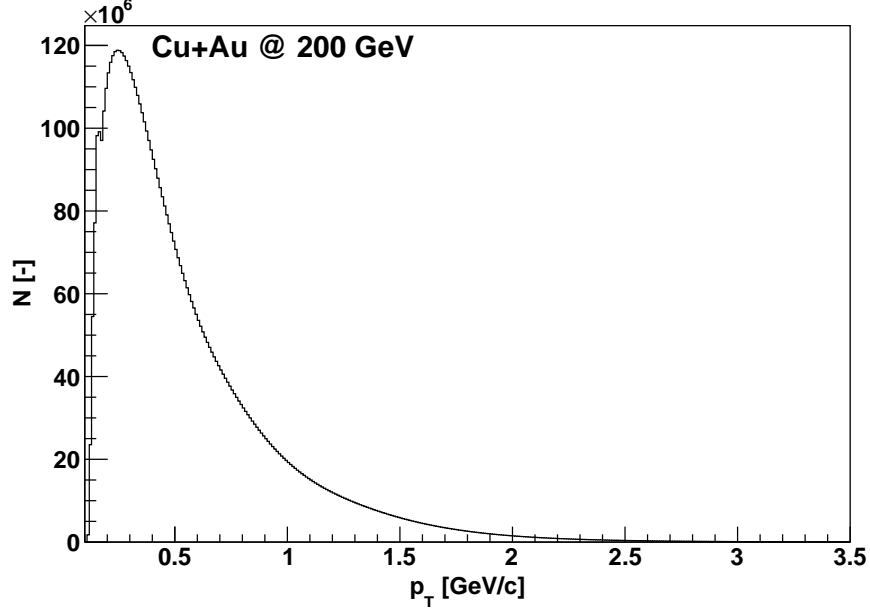


Fig. 5.1: Measured raw p_T distribution of charged pions in the TPC. The Y-axis represent number of charged pions.

Resulting efficiency for pions, ϵ_{π}^{TOF} , is shown in Fig. 5.6. The ϵ_{π}^{TOF} follows similar trend as the ϵ_K^{TOF} . From $p_T = 2.0 \text{ GeV}/c^2$ the efficiency is almost constant at the value $\epsilon_{\pi}^{TOF} = 64 \%$. As in the case of the kaons the high p_T region suffers from the low statistics.

5.2 Tracking efficiency

In order to obtain the tracking efficiency of the TPC, simulated data are embedded into the experimental data. Then this embedded sample is reconstructed via the same reconstruction process that is used for producing the real data. This process is done by the special group within the STAR collaboration.

At first particle production is simulated by the PYTHIA, in the next step events are processed with a detailed GEANT simulation of the STAR detector response. In this manner processed particles have same structure as the real measured data so they can be combined and then be reconstructed by the STAR reconstruction chain. The TPC tracking efficiency is then defined as a ration between the number of reconstructed tracks N^{RC} and the number of embedded tracks N^{EMB} . This embedding process had to

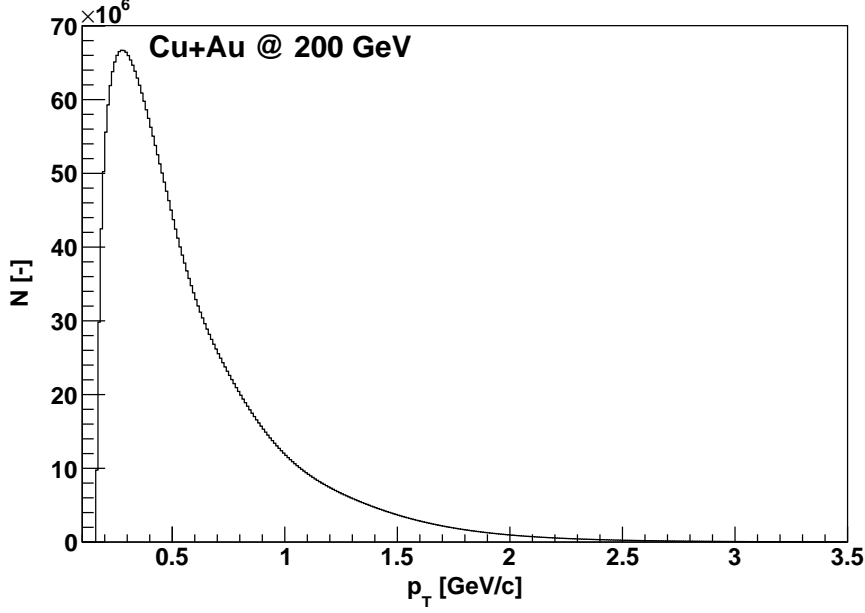


Fig. 5.2: Measured raw p_T distribution of charged pions in the TOF. The Y-axis represent number of charged pions.

be done for all particle species, π^+ , π^- , K^+ , K^- , separately. So for any particle $X \in \{\pi^+, \pi^-, K^+, K^-\}$ the following equation is obtained:

$$\epsilon_X^{\text{TPC}} = \frac{N_X^{\text{RC}}}{N_X^{\text{EMB}}} \quad (5.2)$$

Settings for the embedding of all particles, π^+ , π^- , K^+ , K^- , is shown at the Tab. 5.1.

Embedding variables	Parameters
Data set	Cu+Au, 200 GeV, Run 12
Production	P15ie
Trigger Setup	cuAu_production_2012
Trigger ID	410008
p_T	$0 < p_T < 5 \text{ GeV}/c$ - flat distribution
$ \eta $	< 1.2 - flat distribution
ϕ	$0 < \phi < 2\pi$
No. of events	500 000
$ V_z $	$< 30 \text{ cm}$
$ V_r $	$< 2 \text{ cm}$

Tab. 5.1: Parameters of the embedding process.

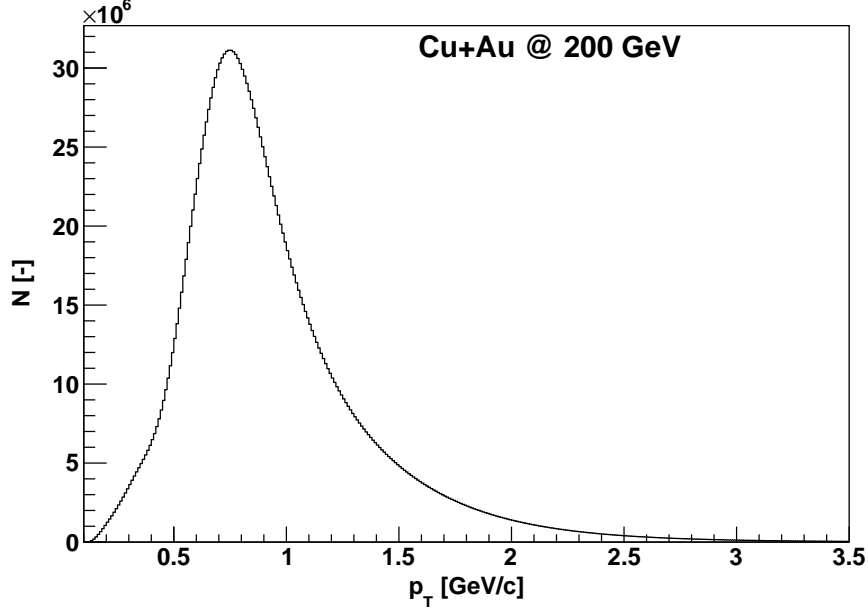


Fig. 5.3: Measured raw p_T distribution of charged kaons in the TPC. The Y-axis represent number of charged kaons.

Tracking efficiency for the K^+ and K^- is shown in Fig. 5.7 and in Fig. 5.8, respectively. Both efficiencies are almost same with saturation around the $\epsilon_K^{\text{TPC}} \approx 80\%$. No discrepancy, with the exception of the statistical fluctuations, between K^+ and K^- can be seen which is completely expected. Efficiencies are fitted by the 5th order polynomial function which is later used for the enumerating of the total reconstruction efficiency of the D^0 meson.

Tracking efficiency for the pions, shown in Fig. 5.9 and in Fig. 5.10, is quite high, about $\epsilon_\pi^{\text{TPC}} \approx 80\%$ across a wide range of the pion p_T . Even for the smallest possible p_T of the pions, 200 MeV/c, $\epsilon_\pi^{\text{TPC}}$ is about 70 %. Due to this effect only the TPC is used for the PID of the pions even at the cost of slightly lower signal purity.

5.3 Total reconstruction efficiency of the D^0 meson

After obtaining all efficiencies ϵ_X^{TOF} and ϵ_X^{TPC} , total reconstruction efficiency of the D^0 meson is evaluated. For pions there is only a $\epsilon_\pi^{\text{TPC}}$ but for kaons both of efficiencies, ϵ_K^{TOF} and ϵ_K^{TPC} , have to be taken into account. The final total reconstruction efficiency of the D^0 meson in the range $0 < p_T < 3.5$ GeV/c is shown in Fig. 5.11.

For the lowest p_T from 0 to 0.5 GeV/c the total reconstruction efficiency

5.3. TOTAL RECONSTRUCTION EFFICIENCY OF THE D^0 MESON87

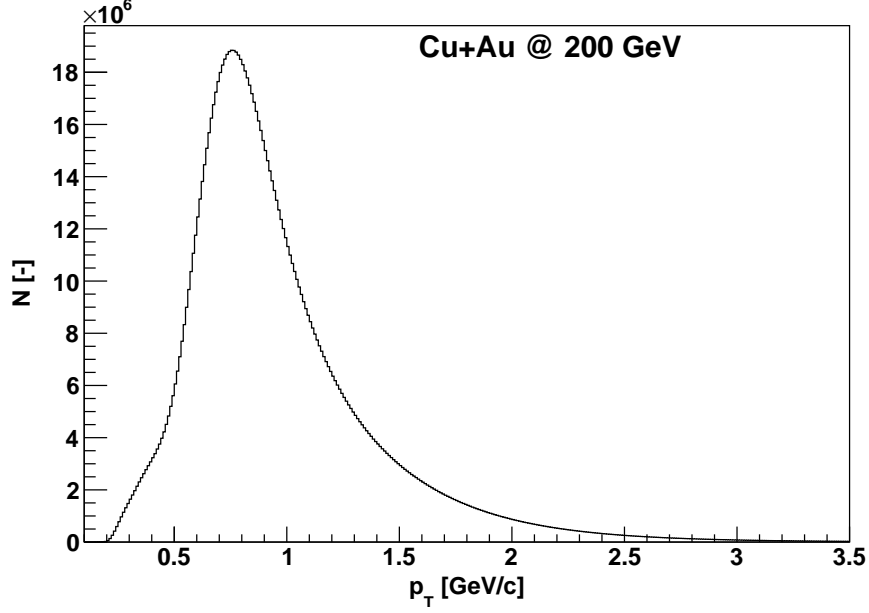


Fig. 5.4: Measured raw p_T distribution of charged kaons in the TOF. The Y-axis represent number of charged kaons.

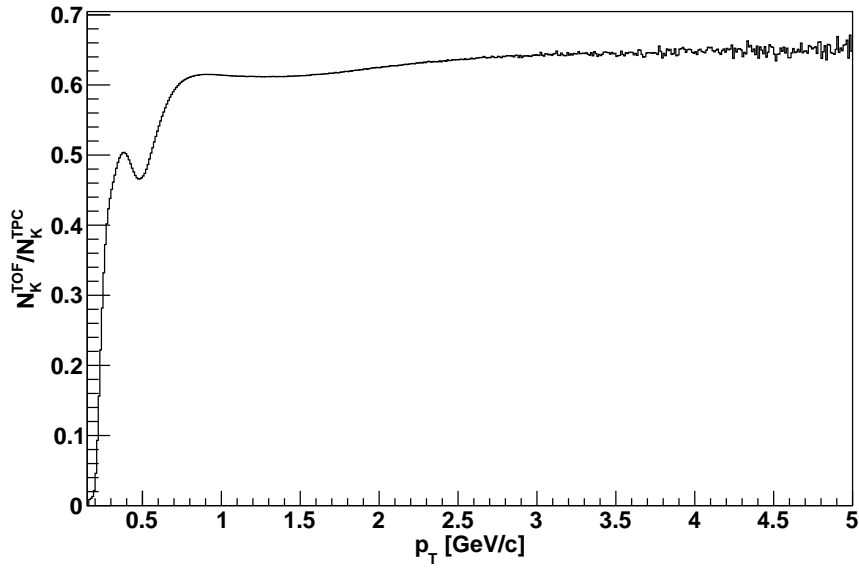


Fig. 5.5: The ϵ_K^{TOF} as a function of the p_T .

of D^0 have the value 18.7 ± 0.1 % but for next p_T bin small decrease of

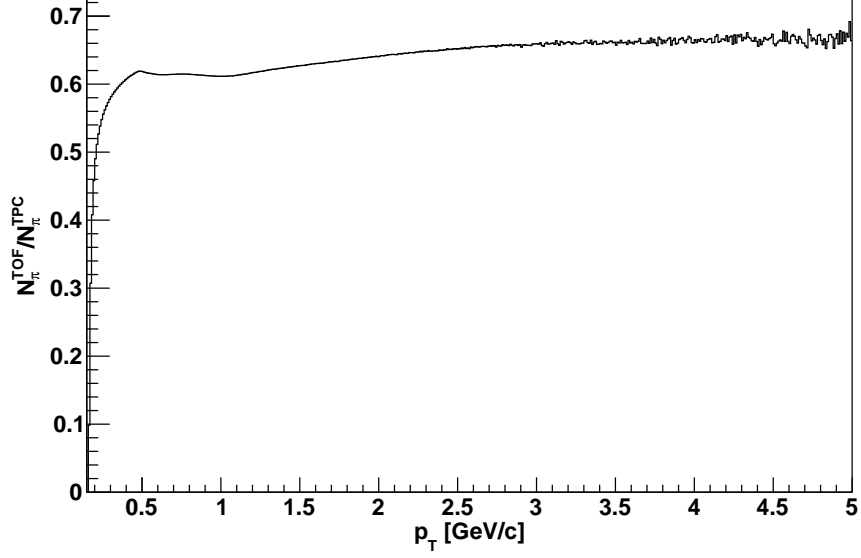


Fig. 5.6: The ϵ_{π}^{TOF} as a function of the p_T .

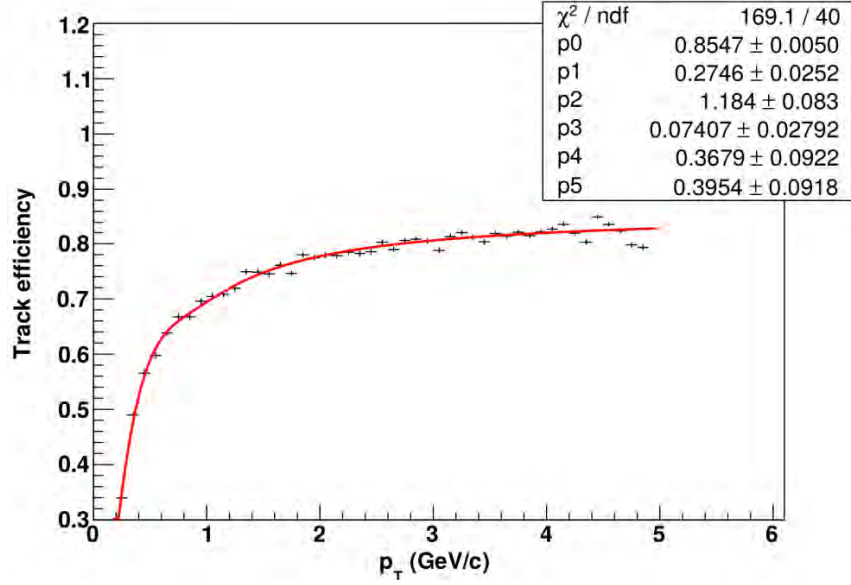


Fig. 5.7: Obtained $\epsilon_{K^+}^{\text{TPC}}$ as a function of the p_T . The $\epsilon_{K^+}^{\text{TPC}}$ is fitted by the 5th order polynomial function.

reconstruction efficiency to the value of $18.4 \pm 0.1 \%$ can be seen. This is mainly due to bump structure in the ϵ_K^{TOF} which is show in the Fig. 5.5

5.3. TOTAL RECONSTRUCTION EFFICIENCY OF THE D^0 MESON89

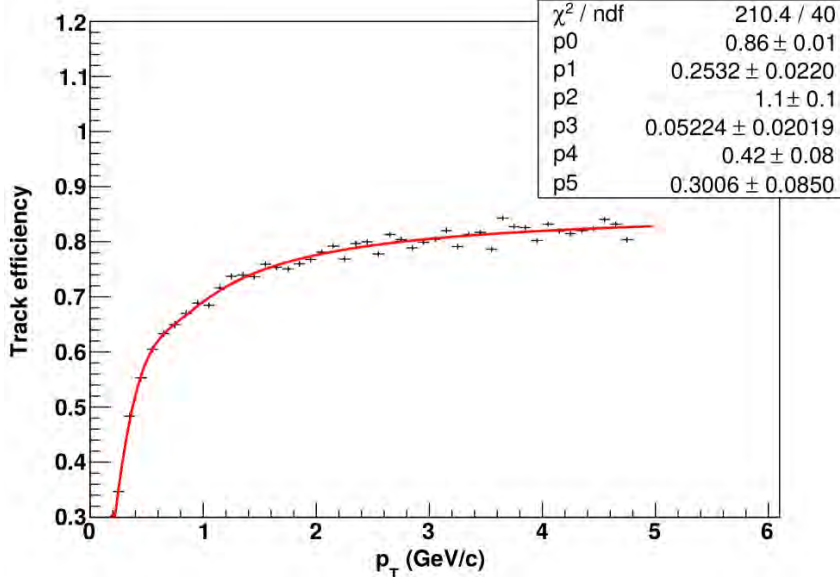


Fig. 5.8: Obtained $\epsilon_{K^-}^{\text{TPC}}$ as a function of the p_T . The $\epsilon_{K^-}^{\text{TPC}}$ is fitted by the 5th order polynomial function.

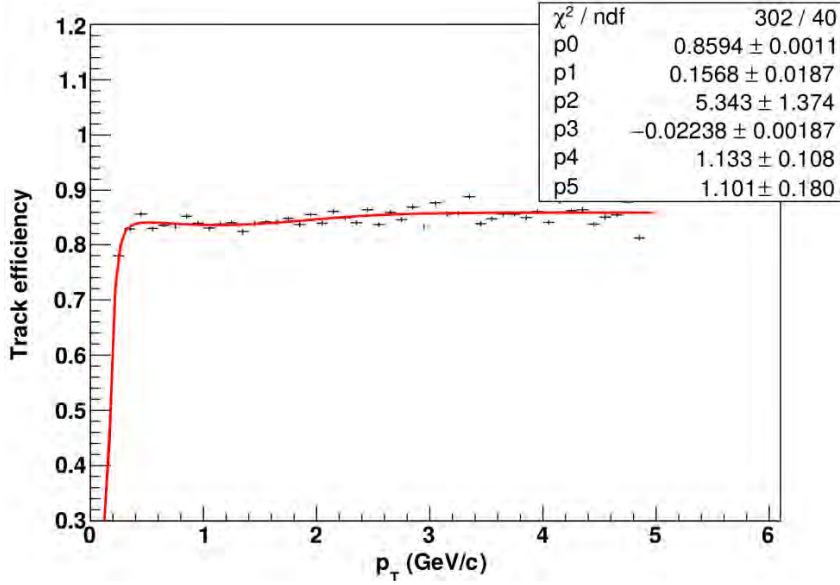


Fig. 5.9: Obtained $\epsilon_{\pi^+}^{\text{TPC}}$ as a function of the p_T . The $\epsilon_{\pi^+}^{\text{TPC}}$ is fitted by the 5th order polynomial function.

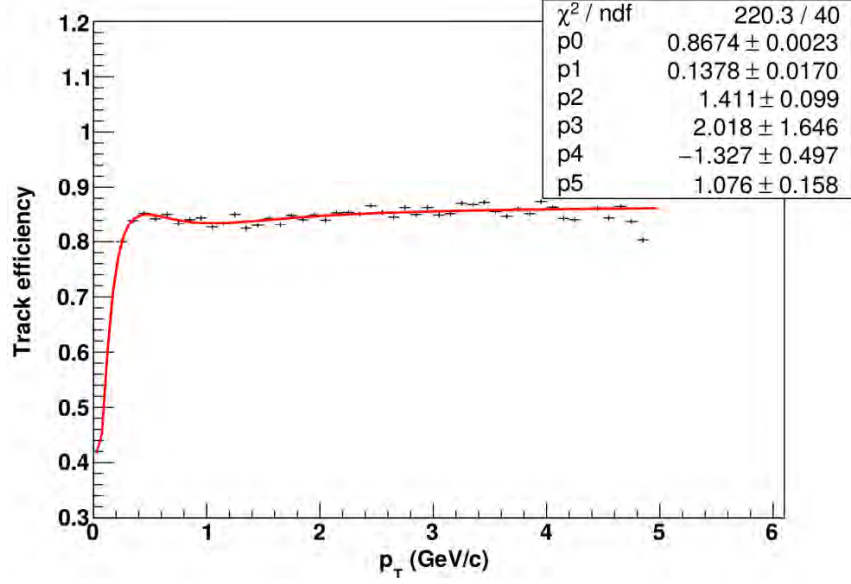


Fig. 5.10: Obtained $\epsilon_{\pi^+}^{\text{TPC}}$ as a function of the p_T . The $\epsilon_{\pi^+}^{\text{TPC}}$ is fitted by the 5th order polynomial function.

and from the non-perfect fit of the tracking efficiencies. From the $p_T > 1.0$ GeV/ c constant slight rise of the reconstruction efficiency can be seen, which is expected because the ϵ_K^{TPC} is still rising in this region.

For the region $0.8 < p_T < 2.0$ GeV/ c , where the D^0 meson signal was reconstructed, the total reconstruction efficiency of the D^0 meson have value:

$$\epsilon_{D^0}^{\text{TOT}} = (18.7 \pm 0.1) \%$$

5.3. TOTAL RECONSTRUCTION EFFICIENCY OF THE D^0 MESON91

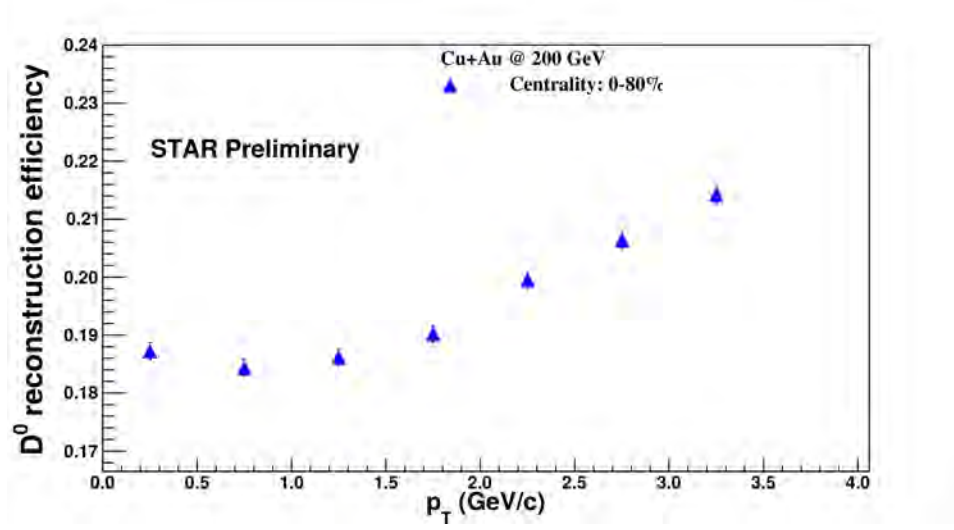


Fig. 5.11: The total reconstruction efficiency of D^0 meson for the $0.2 < p_T < 3.5$ GeV/ c in Cu+Au collisions at $\sqrt{s_{NN}} = 200$ GeV.

Chapter 6

Systematics uncertainties

Systematic uncertainties arise from the fact, that there is only a limited knowledge about nature of all physical processes which happens during measurement, response of the detector to the detected particles and from the imperfect simulations used in various stages of this analysis. Thus due to all of mentioned limits all analysis are biased in some manner. In order to minimize the impact of this bias, systematic uncertainties need to be evaluated and accounted as an another source of uncertainties to the final results. This chapter will provide description of the sources of the systematic uncertainties and how uncertainties were evaluated.

In all cases, value of each type of systematic uncertainties was calculated as a relative fraction of the difference in the raw yield between data set with the standard conditions¹ and data set with variated conditions. All evaluated systematic uncertainties can be divided into 5 classes:

- Tracking
- Background estimation
- Signal extraction
- Branching ratio
- Efficiency

Systematic uncertainties originated from tracking are the largest contributors to the total systematic uncertainty. Origin of tracking uncertainties is in the used cuts on the tracks selections. To assure that obtained results are stable under various tracking conditions, variations of the required *Number of the Fit Points*, ratio of *Number of fit points* and *Number of possible TPC fit points* and gDCA were done. The *Number of the Fit Points*

¹As they were defined at the Chapter 4.

was varied from 20 to 25, ratio of *Number of fit points* and *Number of possible TPC fit points* was varied from 0.52 to the values 0.50 and 0.55, observed D^0 mass peak is shown in Fig 6.1. Default value of the gDCA is 2 cm and that values was varied to the values of 1 and 3 cm, results are shown in Fig. 6.2 for DCA = 1 cm and in Fig. 6.3 for DCA = 3 cm, respectively.

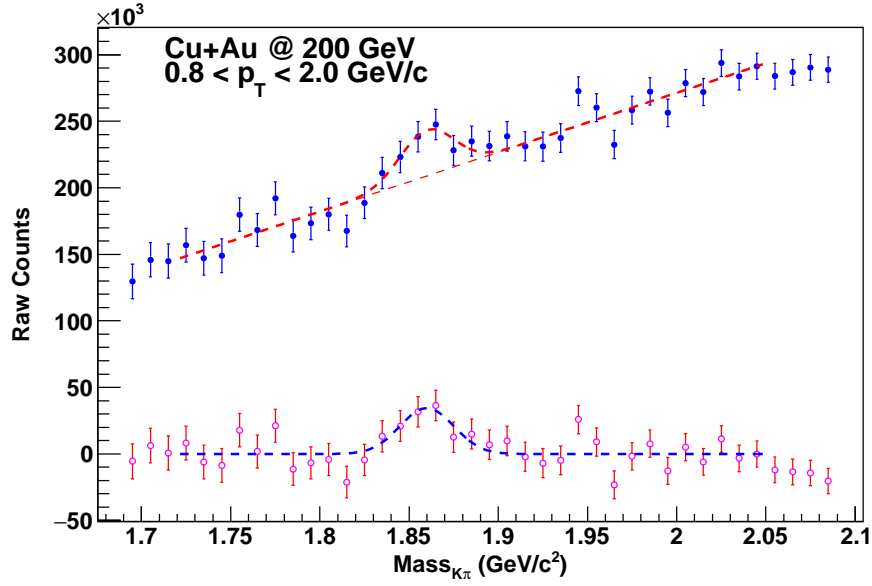


Fig. 6.1: Raw yield of D^0 meson for the p_T bin: $0.8 < p_T < 2.0 \text{ GeV}/c$ with condition $\text{FitPoints} \geq 25$. The blue points represents signal obtained by subtraction of mixed-event (ME) background from unlike-sign (US) signal. The blue dotted line represents fit of residual background. The purple points represents obtained signal after subtraction of the residual background.

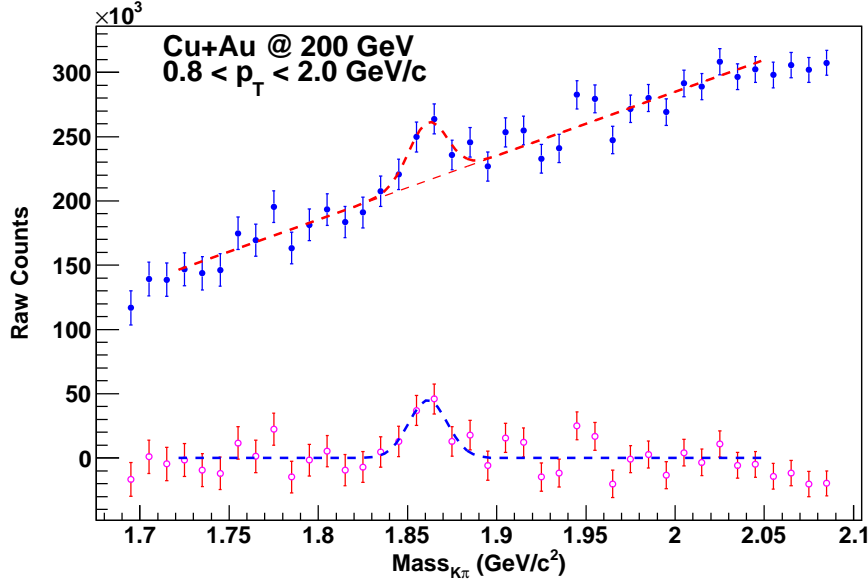


Fig. 6.2: Raw yield of D^0 meson for the p_T bin: $0.8 < p_T < 2.0 \text{ GeV}/c$ for $\text{DCA} = 1 \text{ cm}$. The blue points represents signal obtained by subtraction of ME background from unlike-sign US signal. The blue dotted line represents fit of residual background. The purple points represents obtained signal after subtraction of the residual background.

Main method for the background estimation used in this analysis is the ME method but for control the LS and ROT methods were used. Both control methods give a results with the clearly visible D^0 meson mass peak, so results of this analysis may be considered as a stable with using different background estimation methods.

Signal extraction uncertainty is difference between values of the raw yield obtained by the bin counting in the range of the D^0 mass peak and a value from the Gaussian fit.

Branching ratio uncertainty is taken from the Particle Data Group [23]. This value is a result from the various experiments and model predictions.

Efficiency uncertainty is taken from the fitting functions of the tracking efficiencies (Fig. 5.7, 5.8, 5.9, 5.10). As the fit of the each particle tracking efficiency have its own errors and then those uncertainties are propagated into the total D^0 meson reconstruction efficiency which is crucial for all final results.

When all single sources of the systematic uncertainties were evaluated, final systematic uncertainty was calculated according to the following equation:

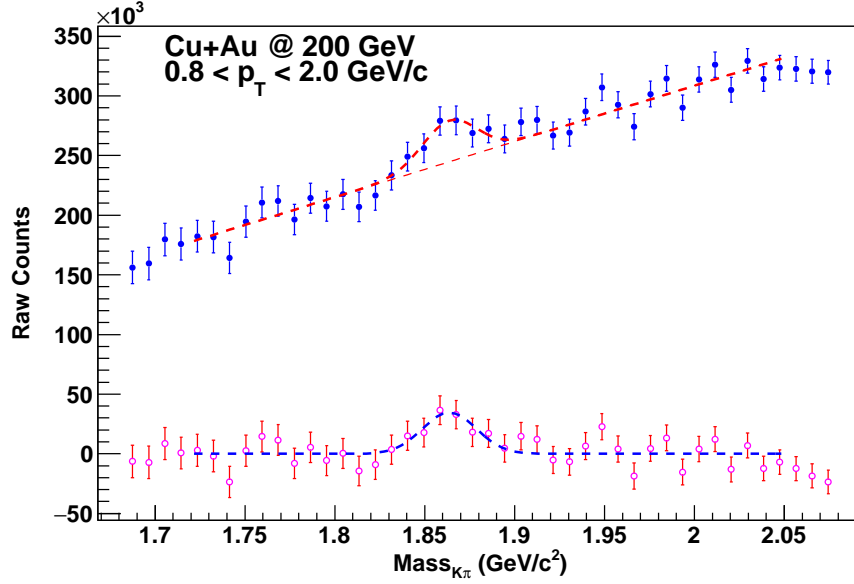


Fig. 6.3: Raw yield of D^0 meson for the p_T bin: $0.8 < p_T < 2.0$ GeV/ c for $DCA = 3$ cm. The blue points represents signal obtained by subtraction of ME background from US signal. The blue dotted line represents fit of residual background. The purple points represents obtained signal after subtraction of the residual background.

$$\sigma_{Sys} = \sqrt{\sigma_{Tracking}^2 + \sigma_{Bckg}^2 + \sigma_{Fit}^2 + \sigma_{BR}^2 + \sigma_{Eff}^2}, \quad (6.1)$$

where σ_{Sys} is total systematic uncertainty, $\sigma_{Tracking}$ is uncertainty from the tracking, σ_{Bckg} is from methods of evaluating the background, σ_{Fit} is from differences between fit and bin counting, σ_{BR} is a uncertainty of the branching ratio and σ_{Eff} is from efficiency calculations. Values of all uncertainties and final systematic uncertainty are in the Tab. 6.1. The total systematic uncertainty is $\sigma_{Sys} = 16.9$ %.

6.1 Double counting

Another source of systematic uncertainties, which is not mentioned so far, is effect of the double counting. The D^0 is reconstructed via the decay channel: $D^0 \rightarrow K^- \pi^+$. In the case if K^- is misidentified as a π^- and π^+ is misidentified as a K^+ , then this pair may contribute to the \bar{D}^0 signal.

Correction on double counting is not included in this analysis due to time constrains. But can be expected, that the significance of the double counting in Cu+Au collisions would be similar to Au+Au collisions. In Fig.

Uncertainty	Value [%]
Tracking	12.6
Background estimation	9.5
Signal extraction	4.9
Branching ratio	1.3
Efficiency	0.9
Total systematic uncertainty	16.9

Tab. 6.1: Sources of the systematic uncertainties with their values and the value of the total systematic uncertainty.

6.4 the results of the double counting analysis in Au+Au collisions is shown. Function represented by the open circles, shows identification of pions and kaons via TPC, second represents identification of pions from TPC and kaons from TPC+TOF. Effect from first variation is dominant for the low p_T region up to 0.5 GeV/c. From there significance linearly decrease to the value about 10 % for $p_T = 3.0$ GeV/c. In this region effect from the second variation took same value and is constant at the about 10 % onward. From this can be seen, that in the case of this analysis, the effect of the double counting is about ~ 1 %.

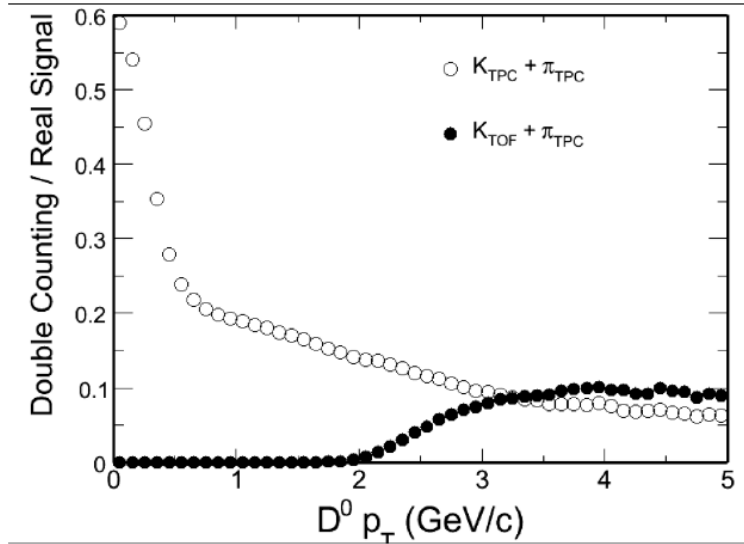


Fig. 6.4: Double counting of D^0 in Au+Au collisions. Open points represents double counting fractions with both pion and kaon identified from TPC. Full circles represents effect with pions identified from TPC and kaons from TPC and TOF. Taken from Ref. [50].

Chapter 7

Results and discussion

This chapter describes results from the analysis of D^0 meson production in Cu+Au collisions at $\sqrt{s_{NN}} = 200$ GeV. The p+p (with $\sqrt{s_{NN}} = 200$ GeV) reference was taken from [31] and the Au+Au (with $\sqrt{s_{NN}} = 200$ GeV) reference was taken from [33].

Resulting invariant yield of the D^0 meson in the p_T range $0.8 < p_T < 2.0$ GeV/ c^2 , was calculated according to the equation 2.10, where, for this case, X is D^0 . After application of corrections, invariant yield is:

$$1/p_T \times d^2N/dydp_{T_{D^0}}^{Cu+Au} = (1.13 \pm 0.29 (stat) \pm 0.19 (sys)) \times 10^{-2} (\text{GeV}/c)^{-2} \quad (7.1)$$

This is to be compared to the invariant yield measured in p+p in the same $\sqrt{s_{NN}}$ and p_T range:

$$1/p_T \times d^2N/dydp_{T_{D^0}}^{p+p} = (1.10 \pm 0.05 (stat) \pm 0.15 (sys)) \times 10^{-4} (\text{GeV}/c)^{-2} \quad (7.2)$$

The large statistical uncertainties in the $d^2N/dydp_{T_{D^0}}^{Cu+Au}$ are primarily due to small available statistics but relative values of the systematic uncertainty 16.9 % for $d^2N/dydp_{T_{D^0}}^{Cu+Au}$ and 13.6 % for $d^2N/dydp_{T_{D^0}}^{p+p}$ are comparable. As the invariant yield is the main component used for enumerating of the nuclear modification factor it can be clearly seen that the small size of the analyzed data-set is a main limiting factor for better precision. The average number of binary collisions N_{coll} in Cu+Au collisions is $N_{coll} = 130$.

Main result of the analysis presented in this Diploma thesis is the nuclear modification factor for the D^0 meson in the Cu+Au collisions in the p_T range $0.8 < p_T < 2.0$ GeV/ c^2 shown in Fig. 7.1. In that figure the obtained result is depicted as the red star and is compared with the published data from the Au+Au collisions [33].

The Au+Au data with the centrality 0-80 % (blue circles) shows certain suppression for the low p_T region up to 0.5 GeV/ c . In the p_T region from

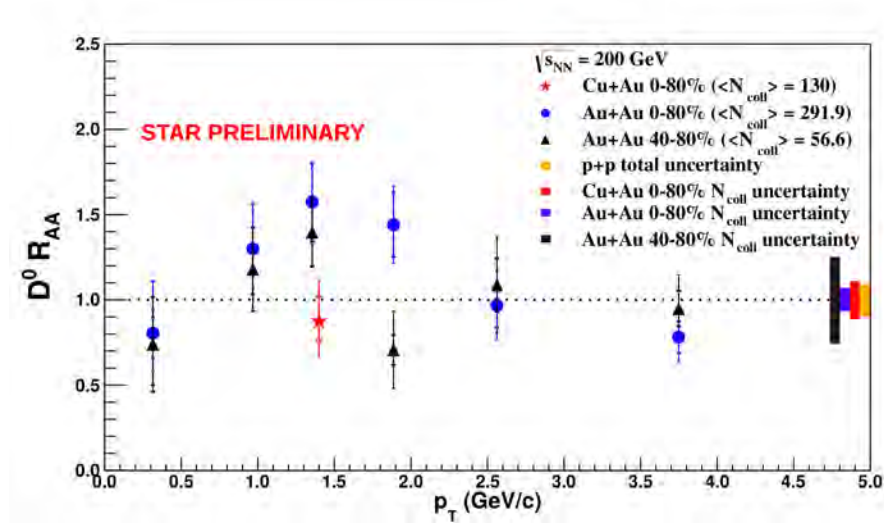


Fig. 7.1: Nuclear modification factor as a function of the p_T for the D^0 meson. The red star represents result of this analysis with the corresponding statistical and systematic uncertainties. The blue circles represent data from the the Au+Au collisions with the 0-80 % centrality with statistical and systematic uncertainties. The black triangles represent data from the Au+Au collisions with the 40-80 % centrality with statistical and systematic uncertainties. Color boxes represent value of the N_{coll} uncertainty for the corresponding data-set. The Au+Au data were taken from the [33].

0.5 to the 2.0 GeV/c enhancement of the D^0 production up to the value $R_{AA}^{D^0} = 1.6$ can be seen. For higher p_T the $R_{AA}^{D^0}$ fall again to the unity and from $p_T = 3.5$ GeV/c suppression about 0.7 can be seen. Uncertainty in the N_{coll} is ± 7 %.

The Au+Au data with the centrality 40-80 % (black triangles) shows similar behavior as the 0-80 % Au+Au data. From the initial suppression there is a rise above unity with the fall under unity from the p_T higher than 4 GeV/c. Uncertainty in the N_{coll} is ± 24 %.

Obtained result from the Cu+Au data shows slight suppression in the p_T range from 0.8 to 2.0 GeV/c which is more consistent with the data from the ALICE experiment shown in Fig. 3.10, Fig. 3.11 and Fig. 3.12, but two points have to be recalled. First, the data from the ALICE experiment are from the Pb+Pb collisions with much higher energy ($\sqrt{s_{NN}} = 2.76/5.02$ TeV at LHC versus $\sqrt{s_{NN}} = 200$ GeV at RHIC) witch correspond to the much higher energy density. The second point is, that the results from the Cu+Au has large uncertainties which cannot exclude that the D^0 production in Cu+Au is compatible with independent superposition of N_{coll} and even with the Au+Au data, which indicates enhancement of the D^0 meson

production.

Conclusion and outlook

This thesis deals with the analysis of D^0 meson production via the hadronic decay channel ($D^0 \rightarrow K^- \pi^+$) in the minimum bias 0-80 % centrality Cu+Au collisions at $\sqrt{s_{NN}} = 200$ GeV at the STAR experiment.

Medium induced modification in the D^0 production in the heavy-ion collisions compared with p+p collisions provide information about the formation and properties of quark-gluon plasma. The asymmetric Cu+Au collisions allows to study D^0 production in different geometry than symmetric Au+Au collisions. Comparing Cu+Au with the Au+Au results (with corresponding centrality) thus constrain influence of the collision geometry on particle production. This is especially interesting for centrality selections with the same number of participants.

Main goals of this Diploma thesis was check the quality of Cu+Au data, obtain D^0 raw yield, calculate invariant yield and nuclear modification factor of D^0 in Cu+Au collisions. All the goals of this Thesis have been successfully fulfilled.

This thesis consists of seven chapters. First three chapters are introductory chapters, describing the STAR experiment at the RHIC, main detectors system of STAR used for this analysis, theory and experimental results overview. Next three chapters describes analysis of D^0 in Cu+Au collisions.

Last chapter, Chapter 7, shows and discuss results of this Thesis. Those results are invariant yield and nuclear modification factor of D^0 in the p_T range 0.8 - 2.0 GeV/c. Nuclear modification factor of D^0 in this p_T is consistent with the unity within sizable statistical and systematic uncertainties. This result slightly favors minor suppression of D^0 , which is consistent with the latest results from the STAR, ALICE and CMS experiments.

Results of D^0 production in 0-80 % centrality Cu+Au collisions presented in this Thesis are not final. In the future additional studies of systematic uncertainties will be done. But more importantly, this analysis was done only on 30 % of the recorded data. When this analysis will be done on the full statistics a notable reduction of statistical uncertainties is expected. Larger statistics will allow to extract signal of D^0 from more than one p_T bin, thus resulting nuclear modification factor should provide more information about behavior of D^0 in Cu+Au collisions.

Bibliography

- [1] GELL-MANN, M. A schematic model of baryons and mesons. Physics Letters [online]. 1964, 8(3), 214-215 [cit. 2017-04-08]. DOI: 10.1016/S0031-9163(64)92001-3. ISSN 00319163. Available from: <http://linkinghub.elsevier.com/retrieve/pii/S0031916364920013>
- [2] ZWEIG G. An SU(3) model for strong interaction symmetry and its breaking. Version 1. 1964. CERN-TH-401
- [3] COLLINS J. C. and PERRY M. J. Superdense Matter: Neutrons or Asymptotically Free Quarks? Physical Review Letters [online]. 1975, 34(21), 1353-1356 [cit. 2017-04-07]. DOI: 10.1103/PhysRevLett.34.1353. ISSN 0031-9007. Available from: <https://link.aps.org/doi/10.1103/PhysRevLett.34.1353>
- [4] Particle Data Group. History of the Universe Poster. [online]. [cit. 2017-04-20] Available from: <http://www.particleadventure.org/history-universe.html>
- [5] OZAKI, S. and ROSER T. Relativistic Heavy Ion Collider, its construction and upgrade. Progress of Theoretical and Experimental Physics [online]. 2015, 2015(3), 3A102-0 [cit. 2016-10-03]. DOI: 10.1093/ptep/ptu093. ISSN 2050-3911. <http://ptep.oxfordjournals.org/cgi/doi/10.1093/ptep/ptu093>
- [6] STAR Images [online]. STAR Collaboration. [cit. 2016-04-03]. <https://drupal.star.bnl.gov/STAR/public/img>
- [7] RUN OVERVIEW OF THE RELATIVISTIC HEAVY ION COLLIDER [online]. [cit. 2017-05-04]. <http://www.rhichome.bnl.gov/RHIC/Runs/index.htm>
- [8] MEEHAN K. C. for the STAR Collaboration. The fixed-target experiment at STAR. Journal of Physics: Conference Series [online]. 2016, 742, 012022- [cit. 2017-04-07]. DOI: 10.1088/1742-6596/742/1/012022. ISSN 1742-6588. Available from: <http://stacks.iop.org/1742-6596/742/i=1/a=012022?key=crossref.6f82a17e3b91e79fdde13c42e9d31993>

- [9] ANDERSON M., BERKOVITZ J., BETTS W., et al. The STAR time projection chamber: a unique tool for studying high multiplicity events at RHIC. Nuclear Instruments and Methods in Physics Research Section A: Accelerators, Spectrometers, Detectors and Associated Equipment [online]. 2003, 499(2-3), 659-678 [cit. 2016-12-05]. DOI: 10.1016/S0168-9002(02)01964-2. ISSN 01689002. <http://linkinghub.elsevier.com/retrieve/pii/S0168900202019642>
- [10] TLUSTÝ D. A Study of Open Charm Production in p+p Collisions at STAR, Ph.D. thesis, Prague 2014
- [11] STAR Collaboration Beam Use Request. [cit. 2016-11-20] [online] <https://drupal.star.bnl.gov/STAR/starnotes/public/sn0657>
- [12] Nuclear Science Advisory Committee, The 2015 Long Range plan for Nuclear Science. [online]. [cit. 2017-03-21]. Available from: <https://science.energy.gov/np/nsac/>
- [13] STAR Collaboration, Physics Opportunities with STAR in 2020+. Internal document [online]. [cit. 2017-04-25]
- [14] sPHENIX Collaboration, An Upgrade Proposal from the PHENIX Collaboration, arXiv:1501.06197v1. [online]. [cit.2016-04-04].
- [15] sPHENIX Collaboration, sPHENIX: The next generation heavy ion detector at RHIC, arXiv: 1611.03003v1. [online]. [cit.2017-04-04]
- [16] ASCHENAUER E.C. et al., eRHIC Design Study: An Electron-Ion Collider at BNL , arXiv:1409.1633 (2014). [cit.2017-04-04]
- [17] GYULASSY M. The QGP Discovered at RHIC. Proceeding of NATO Advanced Study Institute: Structure and Dynamics of Elementary Matter [online]. [cit. 2016-03-10]. <https://inspirehep.net/record/646251>
- [18] YAGI K. et al., Quark-gluon plasma, Cambridge University Press, (2005)
- [19] SARKAR S., SATZ H. and SINHA B. The physics of the Quark-Gluon plasma: introductory lectures. New York: Springer, c2010, ix, 369 p. Lecture notes in physics, 785. ISBN 3540769676
- [20] MILLER, M. L., REYGERS K., SANDERS S. J. and STEINBERG P. Glauber Modeling in High-Energy Nuclear Collisions. Annual Review of Nuclear and Particle Science [online]. 2007, 57(1), 205-243 [cit. 2017-04-09]. DOI: 10.1146/annurev.nucl.57.090506.123020. ISSN 0163-8998. Available from: <http://www.annualreviews.org/doi/10.1146/>
- [21] ZHU Y. Study on Hypertriton Production and Lifetime measurement at RHIC STAR, Ph.D. thesis, Beijing 2013

- [22] RAK J. and TANNENBAUM M. J. High-pT physics in the heavy ion era. x, 387 p. ISBN 0521190290.
- [23] K.A. Olive et al. (Particle Data Group), Chin. Phys. C, 38, 090001 (2014) and 2015 update.
- [24] Why is the Higgs discovery so significant? STFC [online]. [cit. 2016-12-07]. <https://www.stfc.ac.uk/2861.aspx>
- [25] LHCb COLLABORATION. Observation of the resonant character of the $Z(4430)^-$ state. [online]. 2014 [cit. 2016-03-23]. <http://arxiv.org/abs/1404.1903>
- [26] LHCb Collaboration. Observation of J/ψ Resonances Consistent with Pentaquark States in $\Lambda_b^0 \rightarrow J/\psi K^- p$ Decays. Physical Review Letters [online]. 2015, 115(7), [cit. 2016-12-21]. DOI: 10.1103/PhysRevLett.115.072001. ISSN 0031-9007. <http://link.aps.org/doi/10.1103/PhysRevLett.115.072001>
- [27] CHÝLA, J. Quarks, Partons and Quantum Chromodynamics. Skriptum MFF UK 2009. Available from: <http://www-hep2.fzu.cz/chyla>
- [28] VAJZER M. Study of hard processes in the ALICE experiment, Ph.D thesis, Prague 2015
- [29] PHENIX Collaboration. Measurements of directed, elliptic, and triangular flow in Cu+Au collisions at $\sqrt{s_{NN}} = 200$ GeV. [cit. 2016-12-05] <http://arxiv.org/abs/1509.07784v1>
- [30] CBM collaboration. Challenges in QCD matter physics - The scientific programme of the Compressed Baryonic Matter experiment at FAIR. The European Physical Journal A [online]. 2017, 53(3), - [cit. 2017-05-01]. DOI: 10.1140/epja/i2017-12248-y. ISSN 1434-6001. Available from: <http://link.springer.com/10.1140/epja/i2017-12248-y>
- [31] STAR Collaboration. Measurements of D^0 and D^{*+} production in p+p collisions at $\sqrt{s} = 200$ GeV. Physical Review D [online]. 2012, 86(7), - [cit. 2016-06-03]. DOI: 10.1103/PhysRevD.86.072013. ISSN 1550-7998. <http://link.aps.org/doi/10.1103/PhysRevD.86.072013>
- [32] ZHENYU Y. for the STAR Collaboration, Open Charm Hadron Production in p+p, Au+Au and U+U Collisions at STAR. Nuclear Physics A 00 (2014) 1–4
- [33] STAR Collaboration. Observation of D^0 Meson Nuclear Modifications in Au + Au Collisions at $\sqrt{s_{NN}} = 200$ GeV. Physical Review Letters [online]. 2014, 113(14), - [cit. 2016-06-03]. DOI: 10.1103/PhysRevLett.113.142301. ISSN 0031-9007. Available from: <http://link.aps.org/doi/10.1103/PhysRevLett.113.142301>

- [34] XIE G. for the STAR Collaboration. Modification Factor of D^0 Meson in Au+Au Collisions at Nuclear Physics A [online]. 2016, 956, 473-476 [cit. 2017-01-08]. DOI: 10.1016/j.nuclphysa.2016.01.046. ISSN 03759474. Available from: <http://linkinghub.elsevier.com/retrieve/pii/S0375947416000609>
- [35] HE M., RAINER J. F., and RAPP R. Heavy-quark diffusion and hadronization in quark-gluon plasma. Physical Review C [online]. 2012, 86(1), - [cit. 2017-05-01]. DOI: 10.1103/PhysRevC.86.014903. ISSN 0556-2813.
- [36] GOSSIAUX, P. B., AICHELIN J., GOUSSET T. and GUIHO V. Competition of heavy quark radiative and collisional energy loss in deconfined matter. Journal of Physics G: Nuclear and Particle Physics [online]. 2010, 37(9), 094019- [cit. 2017-05-01]. DOI: 10.1088/0954-3899/37/9/094019. ISSN 0954-3899. Available from: <http://stacks.iop.org/0954-3899/37/i=9/a=094019?key=crossref.3c880d1f65db5e83ab0a55ba6490bbdb>
- [37] ALBERICO, W. M., A. BERAUDO, DE PACE A., MOLINARI A., MONTENO M., NARDI M. and PRINO F. Heavy-flavour spectra in high-energy nucleus-nucleus collisions. The European Physical Journal C [online]. 2011, 71(6), - [cit. 2017-05-01]. DOI: 10.1140/epjc/s10052-011-1666-6. ISSN 1434-6044. Available from: <http://link.springer.com/10.1140/epjc/s10052-011-1666-6>
- [38] CAO, S., QIN G. and BASS S. A. Heavy-quark dynamics and hadronization in ultrarelativistic heavy-ion collisions: Collisional versus radiative energy loss. Physical Review C [online]. 2013, 88(4), - [cit. 2017-05-01]. DOI: 10.1103/PhysRevC.88.044907. ISSN 0556-2813. Available from: <https://link.aps.org/doi/10.1103/PhysRevC.88.044907>
- [39] SHARMA, R., VITEV I., and ZHANG B. Light-cone wave function approach to open heavy flavor dynamics in QCD matter. Physical Review C [online]. 2009, 80(5), - [cit. 2017-05-01]. DOI: 10.1103/PhysRevC.80.054902. ISSN 0556-2813. Available from: <https://link.aps.org/doi/10.1103/PhysRevC.80.054902>
- [40] PHENIX collaboration. Forward/backward J/ψ production in Cu+Au collisions at PHENIX. Journal of Physics: Conference Series [online]. [cit. 2016-06-03]. ISSN 1742-6588.
- [41] LINDEN LEVY L. A. What do we really know about cold nuclear matter effects? The European Physical Journal C [online]. 2009, 62(1), 99-102 [cit. 2017-04-08]. DOI: 10.1140/epjc/s10052-009-0947-9. ISSN 1434-6044. Available from: <http://www.springerlink.com/index/10.1140/epjc/s10052-009-0947-9>

- [42] ALICE Collaboration. Measurement of D-meson production versus multiplicity in p-Pb collisions at 5.02 TeV. [cit. 2016-04-20] arXiv:1602.07240
- [43] ALICE Collaboration. Measurement of D-meson production in pp, p-Pb and Pb-Pb collisions with ALICE at the LHC, (2014) Nuclear Physics A, 932 , pp. 51-56.
- [44] ALICE Collaboration. Transverse momentum dependence of D-meson production in Pb-Pb collisions at $\sqrt{s_{NN}} = 2.76$ TeV. Journal of High Energy Physics [online]. 2016, 2016(3), - [cit. 2017-04-10]. DOI: 10.1007/JHEP03(2016)081. ISSN 1029-8479. Available from: [http://link.springer.com/10.1007/JHEP03\(2016\)081](http://link.springer.com/10.1007/JHEP03(2016)081)
- [45] DJORDJEVIC, M., DJORDJEVIC M. Predictions of heavy-flavor suppression at 5.1 TeV Pb+Pb collisions at the CERN Large Hadron Collider. Physical Review C [online]. 2015, 92(2), - [cit. 2017-03-04]. DOI: 10.1103/PhysRevC.92.024918. ISSN 0556-2813. Available from: <https://link.aps.org/doi/10.1103/PhysRevC.92.024918>
- [46] CAO, S., LUO T., QIN G., and WANG X. Linearized Boltzmann transport model for jet propagation in the quark-gluon plasma: Heavy quark evolution. Physical Review C [online]. 2016, 94(1), - [cit. 2017-03-04]. DOI: 10.1103/PhysRevC.94.014909. ISSN 2469-9985. Available from: <https://link.aps.org/doi/10.1103/PhysRevC.94.014909>
- [47] CMS Collaboration. D0D0 meson nuclear modification factor in PbPb collisions at $\sqrt{s_{NN}} = 5.02$ TeV, CMS-PAS-HIN-16-001 [online], [cit. 2017-04-10]. Available from: <https://cds.cern.ch/record/2157844/files/HIN-16-001-pas.pdf>
- [48] STAR Collaboration, Pion, kaon, proton and anti-proton transverse momentum distributions from p+p and d+Au collisions at 200 GeV, Phys. Lett. B 616, 2005
- [49] STAR Collaboration. K(892)* resonance production in Au+Au and p + p collisions at $\sqrt{s_{NN}} = 200$ GeV. Physical Review C [online]. 2005, 71(6), [cit. 2017-04-13]. DOI: 10.1103/PhysRevC.71.064902. ISSN 0556-2813. <https://link.aps.org/doi/10.1103/PhysRevC.71.064902>
- [50] ZHANG Y. for the STAR collaboration. Measurements of D^0 production in Au+Au collisions at $\sqrt{s_{NN}} = 200$ GeV. Analysis note. Internal document of the STAR collaboration.

Appendices

Public posters

1. Presented poster at the Quark Matter 2017, Chicago USA.